Dissertation

submitted to the
Combined Faculty of Mathematics, Engineering and Natural Sciences
of Heidelberg University, Germany
for the degree of
Doctor of Natural Sciences

Put forward by
Marius Günter Sparn
born in Heidelberg, Germany

Oral examination on the 5th of June 2025

Particle Pair Production in Analog Spacetime Realized in a Bose-Einstein Condensate

Referees: Prof. Dr. Markus K. Oberthaler
Prof. Dr. Lauriane Chomaz

Teilchenpaarproduktion in Analoger Raumzeit Realisiert in einem Bose-Einstein-Kondensat – Zusammenfassung Die kosmologische Teilchenproduktion ist eine der wichtigsten Erkenntnisse der Quantenfeldtheorie (QFT) in gekrümmten Raumzeiten. Bei diesem Prozess erzeugt die Expansion des Raums Paare von Teilchen, sogar aus einem anfänglichen Vakuum. Dies entspricht einem eindimensionalen quantenmechanischen Streuproblem, bei dem die Zeitabhängigkeit des Skalenfaktors in das Streupotential einfließt. Die Reflexion an diesem Potential führt zur Produktion von Teilchen. Hier wird dieser Prozess im analogen System eines zweidimensionalen Bose-Einstein-Kondensats aus Kalium-39 untersucht. Seine fundamentalen Anregungen werden als skalares Feld behandelt und die Schallgeschwindigkeit gibt die relevante Skala vor. Die Expansion wird durch eine dynamische Abnahme der Schallgeschwindigkeit über eine magnetische Feshbach-Resonanz simuliert. Wir beobachten kohärente Oszillationen der Dichtefluktuationsspektren, die durch Interferenz der erzeugten Teilchenpaare hervorgerufen werden. Um die Streuungsanalogie zu untersuchen, implementieren wir eine lineare Expansion des Raums, die einem Boxpotential entspricht, und finden keine Teilchenproduktion für Impulsmoden, die mit Resonanzen der Box in Verbindung gebracht werden können. Für periodische Raumzeiten finden wir eine große Teilchenproduktion für Impulse, die den Bandlücken des unendlich ausgedehnten periodischen Potentials entsprechen. In einem Fall finden wir Quetschungen unterhalb das Niveaus von Vakuumfluktuationen, was ein Zeuge für Verschränkung zwischen den besetzten Impulsmoden ist.

Particle Pair Production in Analog Spacetime Realized in a Bose-Einstein Condensate – Summary Cosmological particle production is one of the key findings of quantum field theory (QFT) in curved spacetimes. In this process, the expansion of space produces pairs of particles, even from an initial vacuum. This is equivalent to a one-dimensional quantum mechanical scattering problem, in which the time-dependence of the scale factor is incorporated in a scattering potential. Reflection on the potential gives rise to particle production. Here, this process is investigated in the analog system of a two-dimensional Bose-Einstein condensate of potassium-39. Its fundamental excitations are treated as a scalar field and the speed of sound sets the relevant scale. Expansion is simulated with a dynamical decrease of the speed of sound via a magnetic Feshbach resonance. We observe coherent oscillations of the density fluctuation power spectra which are a result of interference of the produced particle pairs. To probe the scattering analogy, we implement linear expansion of space, which is equivalent to a box potential, and find no particle production for modes that can be associated with resonances of the box. For periodic spacetimes, we find large particle production for momenta that correspond to the band gaps of the infinitely extended periodic potential. In one case, we find squeezing below the level of vacuum fluctuations, which is a witness for entanglement between the populated momentum modes.

Contents

1 Introduction

Plenty of experimental evidence points to the expansion of the universe. The first experimental discovery goes back to 1922, when Carl Wilhelm Wirtz discovered that the spectral lines from galaxies are redshifted to the same lines measured on earth and the amount of redshift is correlated to their apparent brightness. He explained the first with a Doppler shift of the spectral lines, which means the galaxies are moving away from earth. The second, he associated with the distances to the galaxies. Although others had previously found red-shifted galaxies, he concluded that the correlation to the brightness could "be described as a drifting apart of the system of spiral nebulae relative to our point of view" (translated from the German reference [1]). Two years later he connected it to a possible expansion of the whole universe [2]. Towards the end of the 1920s Georges Lemaître and Edwin Hubble similarly concluded that the whole universe is expanding and the velocity is a result of the rate of change of the scale factor of the universe. Both extracted this rate of change that became known as the Hubble constant [3, 4][1].

A decade after the discovery of the expansion of the universe, Erwin Schrödinger realized that such an expansion would lead to particle creation, what he believed to be "alarming" [6]. In an expanding system, its fundamental eigenmodes (he called "proper vibrations") change in time. The notion of a particle and the vacuum itself is ambiguous as the energy eigenstates of the static universe are not eigenstates of its expanding counterpart. Instead, the positive and negative frequency solutions that describe the time evolution of a spatial mode in the static universe are coupled in the process of expansion. At a later time where expansion has either seized or becomes adiabatically slow, one finds that particle number is not conserved during the expansion, but pairs of particles that fulfill momentum conservation have been created. In principle, particles of all fundamental fields can be created in this process.

[1] Many others contributed to this highly active field at the time, which is why some attributions are still disputed today [5].

At todays expansion rates, there exist adiabatically well-defined eigenenergies and their creation rates are negligible [7]. Schrödinger hoped for some other explanation for the red-shift to luminosity correlation (while admitting that "the hypothesis of expansion is probably easier to fit in with observations"). Today, this process at the boundary of quantum and general relativity is regarded as one of the fundamental achievements of quantum field theory in curved spacetimes.

In addition to the expansion we measure today, it is widely accepted that there was a period of rapid expansion in the early universe. This inflationary period solves a variety of theoretical problems. For example, we find an almost perfectly homogeneous cosmic microwave background (CMB) across the size of the observable universe of roughly 46.5 billion years at an estimated age of the universe of 13.8 billion years [8]. Although the discrepancy of these two numbers is an effect of the expansion since the inflationary period, it does not explain why the CMB is almost perfectly correlated over this distance. In the same way, the distribution of matter on large scales is almost perfectly homogeneous and looks the same in all directions (isotropic). The correlation between the causally disconnected regions across the universe can be explained by equilibration at a much smaller scale and a subsequent inflation [9]. The inflationary period also left its imprint on todays universe and the CMB. Quantum fluctuations in the early universe have been increased by the pair-creation mechanism during inflation. The inflated quantum fluctuations were eventually converted into matter fields through a process called reheating, with many open questions still remaining and being actively researched [10, 11]. The resulting small overdensities collapsed under the gravitational instability in an otherwise homogeneous universe. Resulting sound waves traveled through the primordial plasma of interacting nucleons, electrons and light (baryon acoustic oscillations [12]). Once subsequent epochs of further expansion diluted and cooled this system enough to the point where atoms could form, the universe became transparent to light. It decoupled from the matter, and the final pattern of the sound waves was imprinted into the light field. This can be measured today in the form of the strongly red-shifted microwave background. These sound waves also left their imprint on the distribution of galaxies. Because galaxies are more likely to form in the high density regions, they did so in the high density regions produced by the quantum fluctuations. While those are distributed randomly, a slight overdensity formed at the pressure peaks of the sound waves that are at a specific distance to the original high density region. This can be seen in correlation functions of the galaxy distribution in the universe [13].

In Einsteins theory of gravity the geometry of spacetime itself bends under the influence of its energy content. While it is hard to find self-consistent solutions in general, some certain energy distributions allow for a spacetime description via a metric. For example, the homogeneous and isotropic universe can be described by the Friedmann-Lemaître-Robertson-Walker (FLRW) metric. In contrast, a single central mass can be described by the Schwarzschild metric. It captures the local spacetime around a non-rotating uncharged black hole that is characterized by a black hole horizon beyond which no geodesics lead to the outside region. Remarkably, at the extreme curvatures at the event horizon a similar particle creation process can occur. While one particle is trapped inside the horizon, the other escapes in the form of

Hawking radiation [14]. So far, the observation of this process has proved elusive. Not only is the apparent temperature of the radiation inversely proportional to the size of the black hole, it is also a weak effect, in general. For a black hole of the mass of the Sun (which is too small to form by star collapse [15]), this temperature is on the order of a microkelvin. This is much smaller than the temperature of the CMB at 2.7 K [16] that is omnipresent in the universe.

In analog gravity, the idea is to recreate this process in some effective quantum field theory, where quasi-particles can be created by the same processes. This was first proposed by William Unruh in 1981 who realized that the hydrodynamic equations for sound waves in a fluid could be formulated as a metric for quantized sound waves (phonons) [17]. The phonons would be the quasi-particles of the effective quantum field, while the metric is governed by the speed of sound in the fluid and a background flow of the fluid. The sound speed sets the fundamental causal speed analog to the speed of light in the universe. If the fluid itself is flowing, the speed of the sound waves will be governed by the speed of sound and the background flow. For a background flow at the speed of sound or higher, the sound can not travel upstream at all. By constructing a transition point from sub- to supersonic flow speeds, a localized horizon for sound can be created.

Although some theoretical progress was made in the meantime[18, 19], it took over twenty years until the first realization of such an experiment in a water tank [20] and a similar experiment with light in an optical fiber [21] had been achieved. In these experiments a stimulated Hawking process has been reported, where an ingoing wave is amplified. The first implementation of a sound horizon in a Bose-Einstein condensate was achieved in 2010 [22]. Many other systems have been proposed both in the classical regime as well as with tangible hopes to measure the underlying quantum effects [23, 24, 25, 26]. Some have been experimentally realized [27, 28, 29]. Refinements to the BEC experiment, in particular conducting it at extremely low temperatures of the BEC, enabled the measurement of the thermal spectrum expected from Hawking radiation in 2019 [30]. The steps mentioned here are by no means a comprehensive picture. An overview of the historical developments in the field and the analog Hawking effect can be found in [31].

Similarly, the FLRW metric can be implemented in analog systems [32, 33, 34, 35, 36, 37, 38, 39]. This metric allows for the expansion of space, as well as a spatial curvature. It describes a universe that has equal densities everywhere (homogeneous) and looks the same in all directions (isotropic). This is a good approximation of our universe at large scale and can be used to model the processes during inflation. Earlier implementations of expansion in an FLRW-metric include experimental systems based on trapped ions [40], light [41] and BECs [42, 43, 44, 45, 46, 47]. Although in some experiments the system was physically expanded [44, 46], most have implemented the expansion by decreasing the sound speed. This effectively increases the travel time between two points and, as we will see, is equivalent to an expansion. An overview of the field of analog gravity can be found in [48].

In the analog system described in this thesis, we simulate expanding spacetime of an FLRW-metric in a two-dimensional Bose-Einstein condensate of potassium. The low energetic fundamental excitations of this system take the form of phonons.

These are quantized sound waves that are moving at the speed of sound. It depends on the local atom density, as well as the interatomic interaction constant, that is dynamically tunable in the experiment. In previous publications ([49, 47]) we showed that this system is indeed capable of simulating particle creation via a dynamic adjustment of the speed of sound. Additionally, we showed that curvature can be implemented via specific density profiles. We found a striking feature in the particle spectra that are produced in the expansion. However, a clear physical picture of this phenonemon was missing. In light of newly developed theory in which the particle production can be described as reflection on a quantum mechanical potential [50], we can now interpret this feature as a resonance of this scattering potential. Additionally, we construct periodic spacetimes that are equivalent to periodic scattering potentials and find growth for momenta that correspond to the band gaps of the periodic potential. We investigate the final states in terms of a readout akin to state tomography via homodyning with the background condensate at multiple times after the expansion has seized. We find coherent oscillations of the extracted density fluctuation power spectra. These are a result of squeezing of the momentum modes because the particles are being created in pairs. In one case, we find squeezing below the level of vacuum fluctuations, which is a witness for entanglement between the pairwise populated momentum modes. This strongly suggests that the measured density fluctuations are indeed a result of the pair-creation mechanism.

Structure of the Thesis

The thesis is structured as follows. In chapter 2 we investigate the particle pair creation mechanism for a scalar field in curved spacetime. We will see that the absence of energy eigenmodes translates into a time dependence of the particle creation (and annihilation) operators, that in turn leads to a particle creation from a quantum vacuum as defined before the expansion. We present the scattering framework in which time takes the coordinates of space and the time dependence of the scale factor turns into a scattering potential of a Schrödinger equation. Reflections at the potential give rise to particle creation. We discuss the final state as an example for a squeezed state that can show a variance below the level of vacuum fluctuations in the squeezed variable.

In chapter 3 we introduce the necessary BEC theory for the dilute weakly interacting Bose gas. We will find that the interaction gives rise to new quasi-particles, that for low energies have the character of sound waves (phonons) and at higher energies retain the character of free massive particles. We introduce the necessary approximations and the concept of quasi two-dimensionality.

In chapter 4 the analogy is presented for the specific case in question. The quantum fluctuations on the mean field background are decomposed in two real fields. We will find that those are proportional to conjugate fields only in the low momentum limit, in which the excitations are phononic and have the phase velocity of the speed of sound (acoustic regime). For higher momenta, the dispersion must be respected. This can be incorporated in a momentum dependent spacetime metric (rainbow metric). Additionally, the dispersion leads to a prefactor in the extraction of the

spectra, which is important for a quantitative comparison to theoretical predictions and the level of vacuum fluctuations.

Chapter 5 includes all the important information of the experimental platform including the properties of the bosonic isotope ^{39}K and the BEC production. More emphasis is given to the trapping potentials in the BEC stage and the tunability of the interaction. The imaging system and an experimental extraction of its sensitivity at different length scales is covered in detail. This is later used to correct the measured spectra for the experimental sensitivity and is also important for a quantitative interpretation of the results.

Chapter 6 shows experimental results for multiple cosmological scenarios. For a simple linear expansion, we find particle production for all but a few momentum modes. These are identified as the resonances of the equivalent scattering potential. Two periodic cosmologies show very different quasiparticle spectra depending on the form of the periodic potential. This is interpreted as the opening of band gaps. In one case, we find squeezing below the level of vacuum fluctuations.

Finally, the last chapter includes a brief summary of our findings. Additionally, we give an outlook on possible future directions of research on the interface of quantum field theory and curved spacetime in analog systems.

2
Cosmological Particle Production

According to the cosmological standard model, temperature fluctuations in the cosmic microwave background (CMB) provide the initial conditions for large-scale cosmic structure formation [12, 51]. These fluctuations themselves are a result of the cosmological particle production mechanism that creates particle pairs from the quantum fluctuations of empty space. As we will see, this mechanism shows up when a quantum field is subject to an expansion of space [52], which is what happened in the inflationary period of the early universe.

Conceptually, this mechanism results from combining the core principles of quantum field theory (QFT) and general relativity (GR). In that sense, gravity is treated as a classical field, whereas matter fields are quantized. In our model system, a scalar quantum field will be subjected to a classical metric. At first, the model will be invariant under space and time translations as well as Lorentz boosts, providing energy and momentum conservation. Furthermore, the model is homogeneous and isotropic, leaving us with the Friedmann–Lemaître–Robertson–Walker (FLRW) metric.

In QFT a particle can be thought of as an excitation of an associated quantum field. Production and annihilation of particles are often tied to the interaction with other quantum fields, e.g. charged particles creating a (virtual) photon.

As we will see in this chapter, particles can also be created by breaking some of these aforementioned symmetries, in this case time-translation symmetry and, therefore, energy conservation. This happens when the structure of space itself changes over time. If space expands, the eigenmodes of the quantum fields change over time. We will see that we are allowed to think of these modes as quantum harmonic oscillators and the expansion changes the frequencies of these oscillators. As a consequence, the ground state that is the vacuum state before the expansion can differ from the one after expansion, already suggesting that the final field configuration might not be a vacuum state with respect to a particle notion employed at some earlier time.

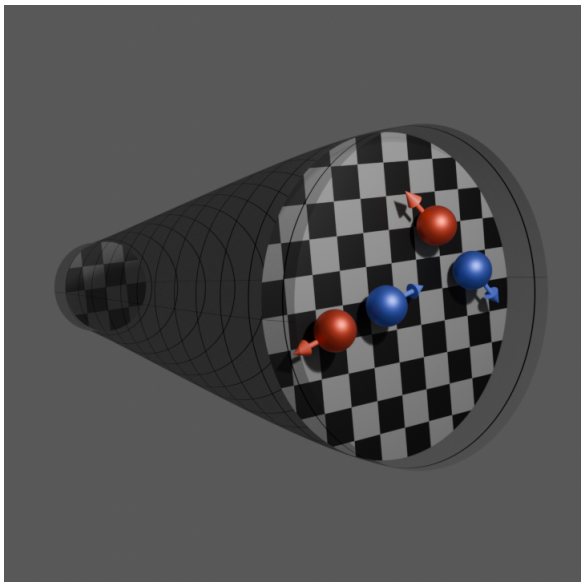

Figure 2.1: Particle production in expanding spacetimes. The vacuum state of a static spacetime is transformed via an epoch of expansion into a state including particle pairs in a spacetime that is again static. Particle pairs have a net momentum of zero. Note that there is no fundamental distinction between the particles and antiparticles of a real scalar field.

Time evolution within the expansion further complicates the matter because energy is not conserved and therefore no well-defined eigenenergies exist. We reformulate particle production in terms of quantum mechanical scattering on a potential which is given by the time dependence of the scale factor. In this framework, particle production is related to the reflection at the potential. Coherent oscillations arising from quantum correlations between produced particles are equivalent to the interference of incoming and reflected amplitudes. This is also discussed in terms of squeezing of the involved momentum modes.

While this effect was first discussed with the fundamental fields in mind, it does also happen in effective field theories whose excitations are quasi-particles. The experiments shown in this thesis are an example of this.

In this first chapter we look at the particle production process in more detail, following [53] chapter 4 as well as [50, 49].

2.1 Scalar Quantum Field in Flat Space

Starting from a classical scalar field $\phi(\mathbf{x}, t)$, its corresponding action has to be invariant under translations and Lorentz boosts (so called Poincaré invariance) to fulfill the aforementioned symmetries. A typical choice is the following [53]:

$$\begin{aligned}\Gamma[\phi] &= \frac{1}{2}\int \mathrm{d}t\, \mathrm{d}^D\mathbf{x}\left[\dot{\phi}^2 - (\nabla\phi)^2 - m^2\phi^2\right] \\ &= \frac{1}{2}\int \mathrm{d}t\, \mathrm{d}^D\mathbf{x}\sqrt{g}\left[-g^{\mu\nu}(\partial_\mu\phi)(\partial_\nu\phi) - m^2\phi^2\right],\end{aligned} \tag{2.1}$$

where dots define the derivative with respect to time t, m is the mass, D is the number of spatial dimensions and $c = 1$. The lower line shows a form with a Minkowski metric $g^{\mu\nu} = diag(-1, \mathbf{1}^D)$ and $\sqrt{g} \coloneqq \sqrt{-\det(g_{\mu\nu})} = 1$. A more general approach, including the spatially curved metrics possible within FLRW universes, can be found in [49, 50]. From the action one finds the equation of motion for $\phi(\mathbf{x}, t)$, the Klein-Gordon equation:

$$\ddot{\phi}(\mathbf{x}, t) - \Delta\phi(\mathbf{x}, t) + m^2\phi(\mathbf{x}, t) = 0 \tag{2.2}$$

Changing to momentum space via a Fourier transform reveals that this is equivalent to the equations of motion of harmonic oscillators

$$\ddot{\phi}_\mathbf{k}(t) + (\mathbf{k}^2 + m^2)\phi_\mathbf{k}(t) = 0, \tag{2.3}$$

one for each momentum $\mathbf{k}$, with frequencies $\omega_k \coloneqq \sqrt{\mathbf{k}^2 + m^2}$.

These can now be quantized like the harmonic oscillator. We find the canonical momentum $\pi_\mathbf{k}(t) = \dot{\phi}_\mathbf{k}$ and promote both to operators on which we impose standard commutation relations:

$$\left[\hat{\phi}_\mathbf{k}(t), \hat{\pi}_{\mathbf{k}'}(t)\right] = i\delta(\mathbf{k} + \mathbf{k}') \tag{2.4}$$

where $\delta(\mathbf{k} + \mathbf{k}')$ is the Dirac-delta function and the reduced Planck constant is set to $\hbar = 1$. Additionally one can define creation and annihilation operators in the Heisenberg picture

$$\hat{a}_\mathbf{k}(t) \coloneqq \sqrt{\frac{\omega_k}{2}}\left(\hat{\phi}_\mathbf{k} + \frac{i\hat{\pi}_\mathbf{k}}{\omega_k}\right), \hat{a}^\dagger_\mathbf{k}(t) = \sqrt{\frac{\omega_k}{2}}\left(\hat{\phi}_{-\mathbf{k}} - \frac{i\hat{\pi}_{-\mathbf{k}}}{\omega_k}\right), \tag{2.5}$$

that fulfill

$$\frac{\mathrm{d}}{\mathrm{d}t}\hat{a}^\dagger_\mathbf{k}(t) = i\omega_k\hat{a}^\dagger_\mathbf{k}(t), \qquad \frac{\mathrm{d}}{\mathrm{d}t}\hat{a}_\mathbf{k}(t) = -i\omega_k\hat{a}_\mathbf{k}(t), \tag{2.6}$$

and the usual Bosonic commutation relations and construct the momentum modes from those:

$$\hat{\phi}_\mathbf{k}(t) = \frac{1}{\sqrt{2\omega_k}}\left(e^{-i\omega_k t}\hat{a}_\mathbf{k} + e^{i\omega_k t}\hat{a}^\dagger_{-\mathbf{k}}\right), \tag{2.7}$$

where we introduced the time-independent construction and annihilation operators $\hat{a}^\dagger_\mathbf{k}$ and $\hat{a}_\mathbf{k}$ and an exponential ansatz for Equation (2.6). The full field operator is obtained via integration over all momentum modes and transformation to real space:

$$\hat{\phi}(\mathbf{x}, t) = \int \frac{\mathrm{d}^D\mathbf{k}}{(2\pi)^{D/2}}\frac{1}{\sqrt{2\omega_k}}\left(e^{-i\omega_k t + i\mathbf{k}\mathbf{x}}\hat{a}_\mathbf{k} + e^{i\omega_k t - i\mathbf{k}\mathbf{x}}\hat{a}^\dagger_\mathbf{k}\right) \tag{2.8}$$

Reordering was used to change $-\mathbf{k}$ to $\mathbf{k}$ in the second term. This will be useful later, but is only valid whenever we consider the integral over the $\hat{\phi}_{\mathbf{k}}(t)$. For completeness, we can also build the Hamiltonian from $\hat{\phi}_{\mathbf{k}}(t)$ and $\hat{\pi}_{\mathbf{k}}(t)$

$$\hat{H} = \frac{1}{2}\int \mathrm{d}^D\mathbf{k}\left[\hat{\pi}_{\mathbf{k}}\hat{\pi}_{-\mathbf{k}} + \omega_k^2\hat{\phi}_{\mathbf{k}}\hat{\phi}_{-\mathbf{k}}\right] = \int \mathrm{d}^D\mathbf{k}\omega_k\left[\hat{a}^\dagger_{\mathbf{k}}\hat{a}_{\mathbf{k}} + \frac{1}{2}\delta(0)\right], \tag{2.9}$$

and can construct the usual number operator $\hat{n}_{\mathbf{k}} = \hat{a}^\dagger_{\mathbf{k}}\hat{a}_{\mathbf{k}}$. Eigenvalues $n_{\mathbf{k}} = 0, 1, 2...$ of this number operator are particle occupation numbers of the mode $\mathbf{k}$. When a measurement is performed in this $\hat{n}_{\mathbf{k}}$ basis, the outcome is one of these eigenvalues. This allows the unambiguous definition of a particle as a non-zero outcome of such a measurement.

The vacuum state

In contrast, the vacuum state $|0\rangle$ is the lowest energy state and has to fulfill $\hat{a}_{\mathbf{k}}|0\rangle = 0$ for all modes $\mathbf{k}$. For the harmonic oscillators this means that each and every one of them is in the ground state. The ground state also has to fulfill the commutation relations (2.4) and can, therefore, not simply be the classical $|\psi_{\mathbf{k},0}\rangle = 0$ solution. Instead, the solutions to the quantum mechanical harmonic oscillator are the Hermite functions $|\psi_{k,n_k}\rangle$, which can be seen in Figure 2.2 a). The ground state with $n_k = 0$ has a gaussian form

$$|\psi_{k,0}\rangle = \sqrt{\frac{\omega_k}{\pi}}\exp\left(-\frac{\omega_k|\phi_{\mathbf{k}}|^2}{2}\right). \tag{2.10}$$

It has a field expectation value of zero but a nonzero variance. It is this width of the ground state that gives rise to the so-called vacuum fluctuations. The vacuum state $|0\rangle$ of the field $\hat{\phi}$ can be constructed via the (infinite) product state of the ground states of all momentum modes. Occupied states can then be constructed by applying the creation operators to the vacuum, as often as needed:

$$|n_1, n_2, ...\rangle = \left[\prod_k \frac{\left(\hat{a}^\dagger_{\mathbf{k}}\right)^{n_{\mathbf{k}}}}{\sqrt{n_{\mathbf{k}}!}}\right]|0\rangle \tag{2.11}$$

The energy of the number states is $E_n = \hbar\omega_k(n_k + 1/2)$ (here $\hbar \neq 1$, compare Eq. 2.9), which means that even an empty single mode contributes $\hbar\omega_k/2$, the so-called zero-point energy. Without further constraints or assumptions such as UV cutoffs, the energy of the quantum vacuum diverges as one sums over all the (infinitely) many momentum modes contributing to the full vacuum state $|\Omega\rangle$. Additionally, the number of modes below a cutoff increases with the volume of space considered. This vacuum energy of empty space might drive the accelerated expansion of space. However, estimations of this typically lead to values of orders of magnitude larger than the bounds to the cosmological constant derived from observational data [54].

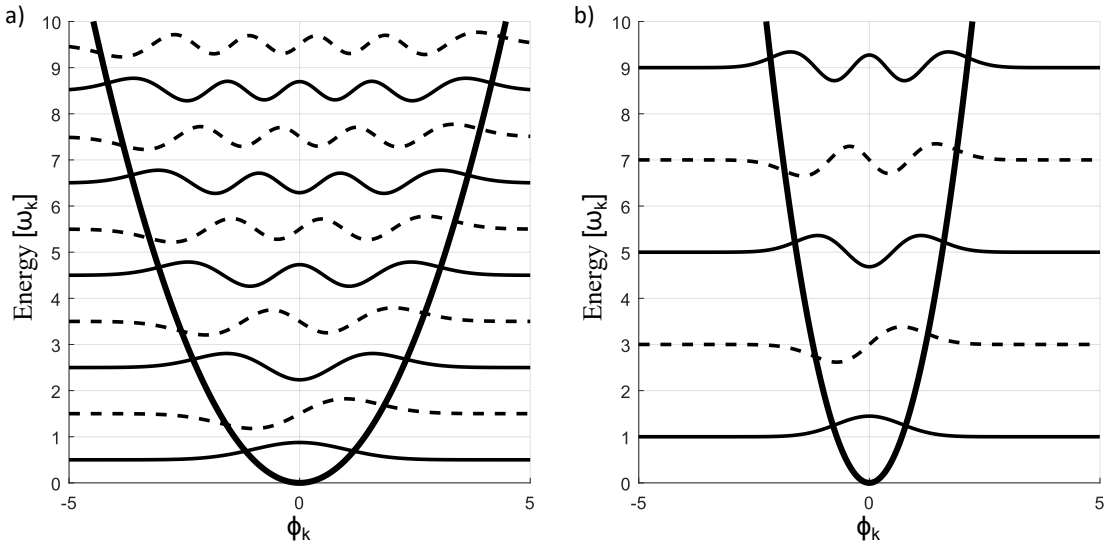

Figure 2.2: a) The quantum harmonic oscillator and its solutions. The thick line shows the harmonic potential of the form $\frac{1}{2}\omega_k^2\phi_{\mathbf{k}}^2$. Solid lines show the symmetric wavefunctions ψ_{k,n_k} of the solutions that correspond to even $n_{\mathbf{k}}$, dashed lines show the asymmetric solutions corresponding to odd $n_{\mathbf{k}}$. The zero point for each solution is shifted to its eigenenergy $\omega_k(n_k + 1/2)$. b) The harmonic oscillator and its solutions for $\tilde{\omega}_k = 2\omega_k$. Although the solutions show the same structure, they have higher energies and a reduced width.

2.2 Particle Production

While it is an open question whether the quantum vacuum state is responsible for the expansion of space, we do know how the vacuum itself transforms under such an expansion. The derivation in Equation (2.1) was only valid within static spacetimes. We can do the same for an expanding spacetime by making the metric tensor in Equation (2.1) time dependent

$$\mathrm{d}s^2 = g_{\mu\nu}\mathrm{d}x^\mu \mathrm{d}x^\nu = -\mathrm{d}t^2 + a^2(t)\mathrm{d}\mathbf{x}^2, \tag{2.12}$$

introducing a time dependent scale factor a(t), that describes expansion (or contraction) of space and was set to one so far. This is an example of a spatially flat FLRW-metric. From now on, we restrict the analysis to two spatial dimensions and massless modes, which is representative of our situation in the experiment. Variation of the action again leads to the Klein-Gordon equation

$$a^2(t)\ddot{\phi}(\mathbf{x},t) - \Delta\phi(\mathbf{x},t) + 2a(t)\dot{a}(t)\dot{\phi}(\mathbf{x},t) = 0 \tag{2.13}$$

and we find that the expansion results in an extra damping term proportional to $\dot{\phi}(\mathbf{x},t)$. The static solution in Equation (2.8) does not solve this (because the equations for the time depended creation and annihilation operators change). Instead we choose a more general ansatz

$$\hat{\phi}(\mathbf{x},t) = \int \frac{\mathrm{d}^2\mathbf{k}}{2\pi}\left(v_k^*(t)\hat{a}_{\mathbf{k}}e^{i\mathbf{kx}} + v_k(t)\hat{a}_{\mathbf{k}}^\dagger e^{-i\mathbf{kx}}\right) \tag{2.14}$$

with the time dependent mode functions $v_k(t)$, that can be interpreted as a representation of time depended frequencies $\omega_k(t)$, a result of the broken time-translation invariance. Because isotropy is still preserved all $|\mathbf{k}| = k$ share the same mode function. This ansatz and Equation (2.13) lead us to the mode equation

$$\ddot{v}_k(t) + 2\frac{\dot{a}(t)}{a(t)}\dot{v}_k(t) + \frac{k^2}{a^2(t)}v_k(t) = 0. \tag{2.15}$$

This is a damped harmonic oscillator equation similar to the undamped one from before (Eq. 2.3). Accordingly, the extra damping term in form of a first derivative with respect to time is sometimes called Hubble friction in the cosmological context. Finding solutions for $v_k(t)$ solves the time dependence for the field. If we know the mode functions at some initial time, we can solve for all later times by integrating the mode equation.

Bogoliubov transformations

In general, solutions are required to fulfill the bosonic commutation relations (Eq. 2.4). Here, the canonical momentum $\hat{\pi} = \sqrt{g}\frac{\mathrm{d}}{\mathrm{d}t}\hat{\phi}$ differs by a factor $a^2(t)$ from the one in Equation (2.1). This leads to the normalization condition

$$a^2(t)[v_k\dot{v}_k^* - \dot{v}_k v_k^*] = i, \tag{2.16}$$

where the term in brackets is the Wronskian $\mathrm{Wr}[v_k, v_k^*] \equiv [v_k\dot{v}_k^* - \dot{v}_k v_k^*]$. Because the Wronskian is nonzero, $v_k(t)$ and $v_k^*(t)$ span a space of solutions

$$u_k(t) = \alpha_k v_k(t) + \beta_k v_k^*(t), \tag{2.17}$$

with complex coefficients α_k and β_k that also solve the mode equation, as well as the normalization condition if

$$|\alpha_k|^2 - |\beta_k|^2 = 1. \tag{2.18}$$

They come with their own set of creation and annihilation operators $\hat{b}_{\mathbf{k}}^\dagger$ and $\hat{b}_{\mathbf{k}}$, that fulfill

$$\hat{a}_{\mathbf{k}} = \alpha_k^*\hat{b}_{\mathbf{k}} + \beta_k\hat{b}_{-\mathbf{k}}^\dagger, \quad \text{and} \quad \hat{a}_{\mathbf{k}}^\dagger = \alpha_k^*\hat{b}_{\mathbf{k}}^\dagger + \beta_k\hat{b}_{-\mathbf{k}}, \tag{2.19}$$

such that the field operator in Equation (2.14) stays the same if we construct it out of u_k and $\hat{b}_{\mathbf{k}}$ instead of v_k and $\hat{a}_{\mathbf{k}}$. This is called a Bogoliubov transformation.

Let us start at a time of constant scale factor $a(t) = a^{\mathrm{I}}$. By comparison with Equation (2.8) we find that the static situation is solved by rotations in the complex plane

$$v_k^{\mathrm{I}}(t) = v_k(t < t_{\mathrm{i}}) = \frac{e^{-i\omega_k^{\mathrm{I}}t}}{a^{\mathrm{I}}\sqrt{2\omega_k^{\mathrm{I}}}}, \tag{2.20}$$

where we again added a factor a^{I} that was set to one before and introduced the index I denoting the first section of constant scale factor. At time t_i the scale factor starts

to change and does so throughout section II. Here we have to solve the full mode Equation (2.15) either analytically or by means of numerical integration methods. Its solutions will in general go beyond the simple oscillating behavior in region I. At a later time t_f we have again a section of constant scale factor a^{III}. We are inclined to represent the solutions by oscillations in the complex plane

$$u_k^{\mathrm{III}}(t) = \frac{e^{-i\omega_k^{\mathrm{III}} t}}{a^{\mathrm{III}}\sqrt{2\omega_k^{\mathrm{III}}}}, \tag{2.21}$$

which is the basis for the static situation in which eigenenergies, number states and the vacuum are well defined. For massless modes, the frequency change is given by the red-shift $\omega_k^{\mathrm{III}}/\omega_k^{\mathrm{I}} = a^{\mathrm{I}}/a^{\mathrm{III}}$. Due to the background dynamics in region II, the full mode solution $v_k(t)$ is not equivalent to u_k^{III} for $t \geq t_f$. However, it can still be projected onto it by means of the inverse Bogoliubov transformation

$$v_k(t) = \alpha_k^* u_k(t) - \beta_k u_k^*(t), \quad \text{and} \quad \hat{b}_{\mathbf{k}} = \alpha_k^* \hat{a}_{\mathbf{k}} - \beta_k^* \hat{a}_{-\mathbf{k}}^\dagger. \tag{2.22}$$

If we plug the oscillating u_k into the inverse Bogoliubov transformation, we see that a non-zero β_k is an admixture of modes oscillating with opposite phase evolution, which is why they are called negative frequency modes. We can construct the coefficients α_k and β_k via the Wronskian (or equivalently by projecting the mode functions $v_k(t_f)$ and their derivatives onto the new mode functions $u_k^{\mathrm{III}}(t_f)$)

$$\alpha_k = -i\mathrm{Wr}[u_k, v_k^*], \quad \text{and} \quad \beta_k = i\mathrm{Wr}[u_k, v_k]. \tag{2.23}$$

If we now take our original vacuum state and apply it to the new number operator in region III we find

$$\begin{aligned} N_k = \langle 0_{\mathrm{I}}| \hat{b}_{\mathbf{k}}^\dagger \hat{b}_{\mathbf{k}} |0_{\mathrm{I}}\rangle &= \langle 0_{\mathrm{I}}| |\alpha_{\mathbf{k}}|^2 \hat{a}_{\mathbf{k}}^\dagger \hat{a}_{\mathbf{k}} |0_{\mathrm{I}}\rangle + \langle 0_{\mathrm{I}}| |\beta_{\mathbf{k}}|^2 \hat{a}_{-\mathbf{k}} \hat{a}_{-\mathbf{k}}^\dagger |0_{\mathrm{I}}\rangle \\ &\quad - \langle 0_{\mathrm{I}}| \alpha_{\mathbf{k}} \beta_{\mathbf{k}}^* \hat{a}_{\mathbf{k}}^\dagger \hat{a}_{-\mathbf{k}}^\dagger |0_{\mathrm{I}}\rangle - \langle 0_{\mathrm{I}}| \alpha_{\mathbf{k}}^* \beta_{\mathbf{k}} \hat{a}_{\mathbf{k}} \hat{a}_{-\mathbf{k}} |0_{\mathrm{I}}\rangle \\ &= \langle 0_{\mathrm{I}}| |\beta_{\mathbf{k}}|^2 \hat{a}_{-\mathbf{k}}^\dagger \hat{a}_{-\mathbf{k}} |0_{\mathrm{I}}\rangle + |\beta_{\mathbf{k}}|^2 \langle 0_{\mathrm{I}}|0_{\mathrm{I}}\rangle = |\beta_{\mathbf{k}}|^2, \end{aligned} \tag{2.24}$$

which means the vacuum state from region I $\hat{a}_{\mathbf{k}} |0_{\mathrm{I}}\rangle = 0$ is not a vacuum state with respect to $\hat{b}_{\mathbf{k}}$ if $\beta_{\mathbf{k}}$ (the admixture of the negative frequency solution) is nonzero. Instead, the changing scale factor produced particles. This effect can show up even if the scale factor at the start and end are the same and there will be experimental examples of that in chapter 6. Then the $v_k(t < t_i)$ and $u_k(t > t_f)$ differ only by a phase factor. Nevertheless, $v_k(t_f)$ can have admixtures of negative frequency solutions i.e. $\beta_{\mathbf{k}} \neq 0$.

2.3 Excitation Power Spectrum and Coherent Oscillations

Besides the particle content of our outgoing state, we can also look at fluctuations in region III ($t > t_f$). For this we consider the equal time connected correlation function of the canonical momentum field

$$\begin{aligned} G_{\pi\pi}(t, \mathbf{x}, \mathbf{x}') &= \frac{1}{2} \langle 0_\mathrm{I}| \left\{ \hat{\pi}(t, \mathbf{x}), \hat{\pi}(t, \mathbf{x}') \right\} |0_\mathrm{I}\rangle \\ &= \frac{1}{2} \left(\langle 0_\mathrm{I}| \hat{\pi}(t, \mathbf{x}) \hat{\pi}(t, \mathbf{x}') |0_\mathrm{I}\rangle - \langle 0_\mathrm{I}| \hat{\pi}(t, \mathbf{x}) |0_\mathrm{I}\rangle^2 \right), \end{aligned} \tag{2.25}$$

where the second term can be taken to vanish due to symmetry. With Eq. 2.14 and $\hat{\pi} = a_f^2 \dot{\hat{\psi}}$ we get

$$\begin{aligned} G_{\pi\pi}(t, \mathbf{x}, \mathbf{x}') = \frac{1}{2} \langle 0_\mathrm{I}| \int \frac{\mathrm{d}^2\mathbf{k}}{2\pi} \int \frac{\mathrm{d}^2\mathbf{k}'}{2\pi} a_f^4 \left(\dot{v}_k^*(t) \hat{a}_\mathbf{k} e^{i\mathbf{k}\mathbf{x}} + \dot{v}_k(t) \hat{a}_\mathbf{k}^\dagger e^{-i\mathbf{k}\mathbf{x}} \right) \\ \left(\dot{v}_{k'}^*(t) \hat{a}_{\mathbf{k}'} e^{i\mathbf{k}'\mathbf{x}'} + \dot{v}_{k'}(t) \hat{a}_{\mathbf{k}'}^\dagger e^{-i\mathbf{k}'\mathbf{x}'} \right) |0_\mathrm{I}\rangle . \end{aligned} \tag{2.26}$$

All but the mixed terms including $\hat{a}_\mathbf{k}^\dagger \hat{a}_{\mathbf{k}'} \delta(\mathbf{k} - \mathbf{k}')$ and $\hat{a}_\mathbf{k} \hat{a}_{\mathbf{k}'}^\dagger \delta(\mathbf{k} - \mathbf{k}')$ vanish for an incoherent or no initial occupation. Because we apply the vacuum state, only a one from the second term contributes (commutator) and we get

$$\begin{aligned} G_{\pi\pi}(t, \mathbf{x} - \mathbf{x}') &= \frac{1}{2} \int \frac{\mathrm{d}^2\mathbf{k}}{2\pi} a_f^4 |\dot{v}_k(t)|^2 e^{i\mathbf{k}(\mathbf{x}-\mathbf{x}')} \\ &= \frac{1}{2} \int \frac{\mathrm{d}^2\mathbf{k}}{2\pi} \omega_k a_f^2 \left(|\alpha_k|^2 + |\beta_k|^2 + 2\mathrm{Re}\left(\alpha_k \beta_k e^{2i\omega_k t} \right) \right) e^{i\mathbf{k}(\mathbf{x}-\mathbf{x}')} \\ &= \int \frac{\mathrm{d}^2\mathbf{k}}{2\pi} \omega_k a_f^2 S_k(t) e^{i\mathbf{k}(\mathbf{x}-\mathbf{x}')}, \end{aligned} \tag{2.27}$$

where we introduced the excitation power spectrum $S_k(t)$ and we find that the correlations depend only on the distance $(\mathbf{x} - \mathbf{x}')$ but not on absolute position because of homogeneity. Moreover, there is no directionality because of isotropy. We put this into the theory when we introduced the mode functions without dependence on $\mathbf{k}$ but only $k = |\mathbf{k}|$.

The Excitation Power Spectrum

Equation (2.27) introduced a quantity that will continue to be relevant throughout this work, the excitation power spectrum

$$S_k(t) = \frac{1}{2} + |\beta_k|^2 + \mathrm{Re}(\alpha_k\beta_k)\cos(2\omega_k t + \vartheta_k) = \frac{1}{2} + N_k + \Delta N_k(t). \tag{2.28}$$

In the definition, the normalization condition (Eq. 2.18) was used and we introduced the time-dependent coherent oscillations $\Delta N_k(t)$ and their phase $\vartheta_k = \arg(\alpha_k\beta_k)$.
The coherent oscillations show up as a time dependence of the fluctuations and the spectrum after expansion has already stopped. This does not mean that there is a time dependence of the particle content N_k of the final state. The oscillation can rather be identified as the anomalous contribution $\langle 0_\mathrm{I}|\,\hat{b}^\dagger_{\mathbf{k}}\hat{b}^\dagger_{-\mathbf{k}}\,|0_\mathrm{I}\rangle = -\alpha_k\beta_k$. This signal is only visible in the correlations and a remnant of the pair production process resulting in interference between a particle pair. In chapter 6 we show this in experimental data.

2.4 Scattering Analogy

The following analogy to the quantum mechanical scattering problem on a potential barrier was already mentioned in the book by Mukhanov and Winitzki that is often cited throughout this thesis.

"We would like to stress once more that this analogy is entirely formal and is useful only to those who have a solid intuition for the corresponding quantum-mechanical problem." – V. Mukhanov and S. Winitzki [53]

We will see that there is a lot to gain from this intuition. We start by introducing conformal time

$$\mathrm{d}\eta = \frac{\mathrm{d}t}{a(t)}. \tag{2.29}$$

In context of our experiment, the speed of sound is incorporated in the scale factor ($a(t) = 1/c_s(t)$). Conformal time then has the units of space. We use it to reformulate the spacetime interval (Eq. 2.12):

$$\mathrm{d}s^2 = -\mathrm{d}t^2 + a^2(t)\mathrm{d}\mathbf{x}^2 = a^2(\eta)[-\mathrm{d}\eta^2 + \mathrm{d}\mathbf{x}^2] \tag{2.30}$$

Additionally, we rescale the mode functions $\psi_k(\eta) = \sqrt{a(\eta)}v_k(\eta)$.

This leads to the new mode equation

$$\psi_k''(\eta) + \left(k^2 - \frac{1}{2}\frac{a''(\eta)}{a(\eta)} + \frac{1}{4}\left(\frac{a'(\eta)}{a(\eta)}\right)^2\right)\psi_k(\eta) = 0, \tag{2.31}$$

where the primes denote derivatives to conformal time. While this might look more complicated than Equation (2.15), it does not have a Hubble-friction term (with a first derivative of the mode function).

Harmonic Oscillator with Time Dependent Frequency

We can interpret everything in brackets in Equation 2.31 as time dependent frequency

$$\omega_k(\eta) = \sqrt{k^2 - \frac{1}{2}\frac{a''(\eta)}{a(\eta)} + \frac{1}{4}\left(\frac{a'(\eta)}{a(\eta)}\right)^2}, \tag{2.32}$$

and get the usual harmonic oscillator. (Alternatively, everything but k^2 can be interpreted as time-dependent effective mass like, for example, in [53, 50, 51]). We can also explain the particle production process, in terms of harmonic oscillators with time-dependent frequency. Consider a harmonic oscillator that changes its frequency $\omega_k(\eta)$ nonadiabatically (much faster than the timescale set by $1/\omega_k(\eta)$). Then we can neglect the time evolution and simply project the old vacuum state onto the new states. Figure 2.2 shows such a change in eigenfrequency from ω_k to $\tilde{\omega}_k = 2\omega_k$. The final state will be a superposition of the symmetric states (even $n_{\mathbf{k}}$), and correspond to particle production. This superposition is not an eigenstate of the oscillator, but describes a breathing motion with $2\tilde{\omega}_k$. This does not change the field expectations values, but their variances and describes the coherent oscillations. By including the full time dependence of the operators, this analogy can also be extended to describe the full problem (beyond the assumption of non-adiabaticity).

The Schrödinger Equation in Conformal Time

Because we want to tap into existing knowledge about the scattering problem, we instead rewrite Equation (2.31) the following way

$$\left(-\frac{\mathrm{d}^2}{\mathrm{d}\eta^2} + V(\eta)\right)\psi_k(\eta) = k^2\psi_k(\eta), \tag{2.33}$$

which is a non-relativistic stationary Schrödinger-equation in conformal time with the potential given by

$$\begin{aligned} V(\eta) &= \frac{1}{2}\frac{a''(\eta)}{a(\eta)} - \frac{1}{4}\left(\frac{a'(\eta)}{a(\eta)}\right)^2 \\ &= \frac{1}{4}\,\dot{a}^2(t(\eta)) + \frac{1}{2}\,\ddot{a}(t(\eta))\,a(t(\eta)), \end{aligned} \tag{2.34}$$

where the lower line shows a version written in derivatives with respect to the laboratory time coordinate t. This potential is zero for a constant scale factor. What was an epoch of changing scale factor translates into a region of non-zero potential.

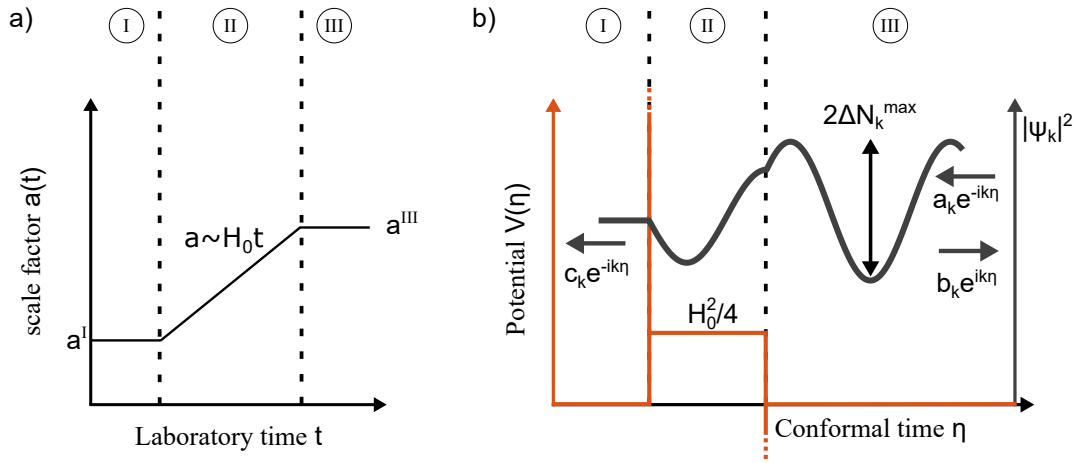

Figure 2.3: Scheme of the scattering analogy. The time dependence of the scale factor $a(t)$ translates into the scattering potential that depends on conformal time η. The linear expansion $a^{\mathrm{II}}(t) \sim t$ in (a) corresponds to a box potential (b). The mode function v_k is replaced by the scattering state ψ_k. To compare to the usual scattering problem, the causal order is reversed. An incoming state of amplitude a_k is scattered on the barrier such that some part b_k is reflected and another c_k transmitted. The transmitted state is the original vacuum state in region I. The reflected state corresponds to produced particles $\sim |b_k^2|$, the interference of incoming and reflected state is responsible for coherent oscillations $\sim |a_k b_k|$. Singular contributions in the form of δ-peaks stem from the sudden switch of the expansion rate at the boundaries between the regions.

We again consider the three epochs from before. Region I with $\eta < \eta_i = \eta(t_i)$ and region III with $\eta > \eta_f = \eta(t_f)$ have constant scale factors a^{I} and a^{III} and are connected by region II of time dependent scale factor. In region I we again find oscillatory mode functions

$$\psi_k^{\mathrm{I}}(\eta) = c_k e^{-i\omega_k(\eta)\eta} = c_k e^{-ik\eta}, \tag{2.35}$$

and in region III we allow for a superposition of those with positive and negative frequencies $\omega_k = \pm k$

$$\psi_k^{\mathrm{III}}(\eta) = a_k e^{-ik\eta} + b_k e^{ik\eta}. \tag{2.36}$$

In region II the full Schrödinger Equation (2.33) has to be solved and wavefunctions and derivatives have to be matched at the boundaries.

We can now interpret particle production as a standard scattering problem. An example we will later discuss in more detail is illustrated in Figure 2.3:

1. We start with an incoming wave from the right, the region of large η or future lab time

$$\psi_k^{\mathrm{inc}}(\eta) = a_k e^{-ik\eta}, \tag{2.37}$$

traveling towards the potential barrier $V(\eta)$.

2. At position η_f it starts interacting with the potential barrier, where some portion is reflected
$$\psi_k^{\mathrm{ref}}(\eta) = b_k e^{ik\eta}. \tag{2.38}$$

3. The rest exits the barrier at η_i
$$\psi_k^{\mathrm{trans}}(\eta) = c_k e^{-ik\eta}. \tag{2.39}$$

Conservation of probability gives constraints on the prefactors a_k, b_k and c_k
$$|a_k|^2 = |b_k|^2 + |c_k|^2. \tag{2.40}$$

This is the normalization condition for the Bogoliubov coefficients α_k and β_k (Eq. 2.18). To get the values of the prefactors we have to match the plane wave ansatz for the static regions and the (numerical) solution of region II at the boundaries of the regions
$$\begin{aligned} \psi_k^{\mathrm{I/II}}(\eta_{i/f}) &= \psi_k^{\mathrm{II/III}}(\eta_{i/f}), \\ \frac{\mathrm{d}}{\mathrm{d}\eta}\psi_k^{\mathrm{I/II}}(\eta_{i/f}) &= \frac{\mathrm{d}}{\mathrm{d}\eta}\psi_k^{\mathrm{II/III}}(\eta_{i/f}). \end{aligned} \tag{2.41}$$

These conditions where previously ensured by the Wronskian (Eq. 2.23)) and one could do the same here. We can identify
$$\alpha_k = \frac{a_k^*}{c_k^*} \quad \text{and} \quad \beta_k = -\frac{b_k}{c_k^*}. \tag{2.42}$$

Particle production is now tied to reflection at the potential. The particle number
$$N_k = |\beta_k|^2 = \frac{|b_k|^2}{|c_k|^2}, \tag{2.43}$$

is non-vanishing if reflection is present. We can also identify the complex reflection and transmission amplitudes
$$r_k = \frac{b_k}{a_k} \quad \text{and} \quad t_k = \frac{c_k}{a_k}. \tag{2.44}$$

The excitation power spectrum (compare Eq. 2.27) is simply given by the wavefunction in region III
$$S_k(\eta) = \frac{|\psi_k^{\mathrm{III}}(\eta)|^2}{2|c_k|^2} = \frac{|\psi_k^{\mathrm{inc}}(\eta) + \psi_k^{\mathrm{ref}}(\eta)|^2}{2|c_k|^2}. \tag{2.45}$$

Coherent oscillations are a result of the interference term of the incoming and reflected wavefunction
$$\Delta N_k(\eta) = \frac{|a_k b_k|}{|c_k|^2}\cos\left(2k\eta + \vartheta_k\right) = \Delta N_k^{\max}\cos\left(2k\eta + \vartheta_k\right), \tag{2.46}$$

Particle Production	Scattering	Harmonic Oscillator
scale factor $a(t)$	scat. potential $V(\eta)$	frequency $\omega(\eta)$
mode functions $v_k(t)$	scat. states $\psi_k(\eta)$	ground state $\psi_{k,0}$
Bogoliubov coefficients α_k, β_k	scat. amplitudes a_k, b_k, c_k	mode overlaps
$\lvert\alpha_k\rvert^2 - \lvert\beta_k\rvert^2 = 1$	$\lvert a_k\rvert^2 = \lvert b_k\rvert^2 + \lvert c_k\rvert^2$	$\sum_n \lvert\psi_{k,n}\rvert^2 = 1$
Coherent oscillations	interference of ψ_k^{inc} and ψ_k^{ref}	breathing motion

Table 2.1: Side by side comparison of important quantities of the cosmological pair creation mechanism and their counterparts in the analogous processes describing quantum mechanical scattering on a potential barrier and a quantum harmonic oscillator with time dependent frequency.

where we introduced the amplitude of the oscillations $\Delta N_k^{\max}$. In contrast to usual scattering events the whole problem is not normalized to some particle stream going towards the barrier in region III, but is normalized with respect to region I instead. This is a result of the relabeling of a constituent of ψ_k^{III} to incoming wave, which reverses the causal order of the problem. Comparison with the mode function in region I (Eq. 2.20) gives $c_k = 1/\sqrt{2\omega_k}$. The reinterpretation of what are incoming and outgoing modes transformed the problem from that of symplectic Bogoliubov transformations to unitary quantum mechanics. Table 2.1 shows the different aspects of pair creation and their scattering counterparts side by side.

Box Potential and Singular Contributions

Figure 2.3 shows a linear expansion of the form $a^{\text{II}}(t) = a_{\min}(1 + H_0 t)$ that corresponds to a box potential of height $H_0^2/4$ in the scattering framework (Eq. 2.34). In region I and III the scale factors are constant and the potential is zero. Whereas the wavefunction in region I has a single positive frequency constituent which results in $\left|\psi^{\text{I}}(\eta)\right|^2 = const.$, the wavefunction in region III has incoming and reflected constituents (positive and negative frequency) and shows an interference pattern $\Delta N_k(\eta)$ and a mean that is enhanced by N_k.

What we ignored so far is that the expansion does not start and end in a smooth way (and is therefore not continuously differentiable). Instead, the first derivative $\dot{a}$ is turned on (off), which we can describe by multiplication with Heaviside functions

$$\dot{a}(t) = \dot{a}^{\text{II}}(t)\Theta(t - t_i)\Theta(t_f - t). \tag{2.47}$$

These turn into positive (negative) δ-peaks in the second derivative

$$\ddot{a}(t) = \dot{a}^{\text{II}}(t)(\delta(t - t_i) - \delta(t_f - t)) + \ddot{a}^{\text{II}}(t)\Theta(t - t_i)\Theta(t_f - t). \tag{2.48}$$

The last term is just the regular contribution of $\ddot{a}(t)$ that is zero in this example.

The rest turns into a singular contribution to the potential (Eq. 2.34)

$$\begin{aligned} V_s &= \frac{1}{2}\dot{a}^{\mathrm{II}}(t)a^{\mathrm{II}}(t)(\delta(t-t_i)-\delta(t_f-t)) \\ &= \frac{\mathcal{H}(\eta)}{2}(\delta(\eta-\eta_i)-\delta(\eta_f-\eta)), \end{aligned} \tag{2.49}$$

with the conformal Hubble rate $\mathcal{H}(\eta) = a'(\eta)/a(\eta)$.

The δ-peaks result in a phase kick of the wavefunction, that is a discontinuity in its first derivative ψ_k' ([55])

$$\frac{\mathrm{d}}{\mathrm{d}\eta}\psi_k^{\mathrm{II}}(\eta_i) - \frac{\mathrm{d}}{\mathrm{d}\eta}\psi_k^{\mathrm{I}}(\eta_i) = \frac{\mathcal{H}(\eta)}{2}\psi_k(\eta_i), \tag{2.50}$$

for the first peak and with opposite sign at η_f. We defined $\psi_k^{\mathrm{I}}(\eta_i) \equiv \lim_{\epsilon\to 0^+} \psi_k(\eta_i-\epsilon)$ and $\psi_k^{\mathrm{II}}(\eta_i) \equiv \lim_{\epsilon\to 0^+} \psi_k(\eta_i+\epsilon)$. In comparison to the matching condition found earlier (Eq. 2.41) we retain the one for ψ_k but have to add the phase shift from the delta peak, which amounts to $\frac{\mathcal{H}(\eta)}{2}\psi_k(\eta_i)$, to match its derivative.

More generally, whenever there is a δ-peak in the potential, it will result in a phase shift of the wavefunctions. More details on this and why the phase kicks can be interpreted as the application of a squeezing or anti-squeezing operator can be found in [50].

2.5 Squeezing and Entanglement

Although we found $N_k = |\beta_k|^2$, the original vacuum state is not an eigenstate of the new number operator. If so, it would be an eigenstate of the Hamiltonian and there would be no observable time dependence. However, we did find a time dependence of the excitation power spectrum in form of coherent oscillations (Sect. 2.3).

Analogous to this we can calculate the quantum fluctuations in the non-commuting observables

$$\begin{aligned} \Delta\pi_k^2 &= \langle 0_{\mathrm{I}}|\,(\hat{\pi}_k)^2\,|0_{\mathrm{I}}\rangle - \langle 0_{\mathrm{I}}|\,\hat{\pi}_k\,|0_{\mathrm{I}}\rangle^2 = \omega_k a_f^2\left(\frac{1}{2}+N_k+\Delta N_k(t)\right) = \omega_k a_f^2 S_k(t), \\ \Delta\phi_k^2 &= \frac{1}{\omega_k a_f^2}\left(\frac{1}{2}+N_k-\Delta N_k(t)\right). \end{aligned} \tag{2.51}$$

With $N_k = |b_k|^2/|c_k|^2$ and $\Delta N_k^{\max} = |a_k b_k|/|c_k|^2$ we find that for the vacuum without particle production (i.e. $b_k = 0$) we get

$$\sqrt{\omega_k a_f^2}\Delta\phi_k = \frac{1}{\sqrt{\omega_k a_f^2}}\Delta\pi_k = \sqrt{\frac{1}{2}}. \tag{2.52}$$

We can interpret the 1/2 in the spectra as the level of vacuum fluctuations that are the result of the Heisenberg uncertainty limit.

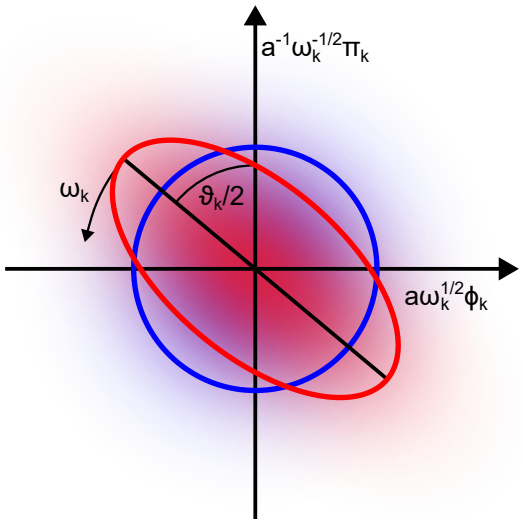

Figure 2.4: Phase space distribution of a squeezed state (red) and original vacuum state (blue) overlapped. The solid lines are lines of equal (quasi-)probability density, illustrating that the squeezing in one observable was compensated by anti-squeezing in the non-commuting canonical observable. The axis of the squeezed state rotates in phase space with ω_k, which gives rise to coherent oscillations. This is equivalent to a phase space description of the breathing motion of the harmonic oscillator discussed before (see Fig. 2.2).

For $b_k \neq 0$, we use the fact that the reflected amplitude is always smaller than the incoming amplitude (conservation of probability). This means $\Delta N_k^{\max} \geq N_k$, and there are times t, where one of these variances drops below the level of vacuum fluctuations. At the same time, the product of the uncertainties $\Delta\phi_k \Delta\pi_k \geq \frac{1}{2}$ is always greater or equal to that of the vacuum.

This effect is called Squeezing and a consequence of the fact that particles are produced in entangled pairs of opposite momenta. The b eigenstates are a superposition of number states [53], e.g.

$$|0_{\mathrm{III}}\rangle = \prod_{\mathbf{k}} \frac{1}{\sqrt{\alpha_{\mathbf{k}}}} \exp\left\{ \frac{\beta_k}{2\alpha_k} \hat{a}_{\mathbf{k}}^\dagger \hat{a}_{-\mathbf{k}}^\dagger \right\} |0_{\mathrm{I}}\rangle \,. \tag{2.53}$$

The exponential is an example of a squeezing operator. It transforms a symmetric Gaussian state (e.g. the vacuum state) into a state with asymmetric widths (i.e. uncertainties). An example can be seen in Figure 2.4 where the phase space distributions of a vacuum and squeezed state are compared. The coherent oscillations then reduce to phase space rotations. This is equivalent to a phase space description of the breathing motion of the harmonic oscillator discussed before.

A squeezing of the quantum fluctuations below the level of the vacuum state can be connected to the non-separability of the pair state [56, 57, 58]. This makes $S_k(t) < 1/2$ for any time t a witness for entanglement. [45, 59]

3
BEC Theory

This chapter contains the necessary theory of Bose-Einstein condensates. We will see that small excitations of a weakly interacting bosonic gas can be described in terms of new quasi-particles that are connected to the free (non-interacting) particles through a Bogoliubov transformation similar to the last chapter. At low kinetic energies, the energy of these quasi-particles is dominated by the interaction. They behave like the sound waves in a fluid and move at the speed of sound. At high kinetic energies, the particles retain their original character of massive particles. The corresponding scales are derived and the experimentally relevant case of the quasi-two-dimensional BEC is discussed.

The key feature of Bose-Einstein condensation is a macroscopic occupation of the ground state ψ_0 of the system, which can only happen for bosonic (quasi-)particles. This is achieved at high phase space densities when the thermal de-Broglie wavelength is roughly on the order of the interparticle spacing [60]. The precise geometry of the single particle wavefunction of the ground state ψ_0 depends on external trap parameters. A nice consequence of this macroscopic occupation is the (quasi-)long range order in the system, stemming from the fact that the ground state particles share a single phase. This phenomenon is often interpreted as the breaking of the U(1) gauge symmetry, which is the freedom of choice of a global phase.

This does not mean, however, that all particles need to be in the ground state, as this phase coherence can still be retained for a small non-condensed (e.g. thermal) fraction. The full field operator can be written in the form:

$$\hat{\Phi} = \psi_0 \hat{a}_0 + \sum_{i>0} \psi_i \hat{a}_i \tag{3.1}$$

where the $\hat{a}_i$ are the creation operators of the single particle states ψ_i.

Because the atoms in our system are weakly interacting, we introduce a interaction potential that depends on the relative position between the particles $V(\mathbf{r}' - \mathbf{r})$

and get the Hamiltonian [61]

$$\begin{aligned}\hat{H} = &\int \left(\frac{\hbar^2}{2m}\nabla\hat{\Phi}^\dagger(\mathbf{r})\nabla\hat{\Phi}(\mathbf{r})\right)\mathrm{d}\mathbf{r} + \int \hat{\Phi}^\dagger(\mathbf{r})V_{\mathrm{ext}}(\mathbf{r})\hat{\Phi}(\mathbf{r})\mathrm{d}\mathbf{r} \\ &+ \frac{1}{2}\int \hat{\Phi}^\dagger(\mathbf{r}')\hat{\Phi}^\dagger(\mathbf{r})V(\mathbf{r}'-\mathbf{r})\hat{\Phi}(\mathbf{r}')\hat{\Phi}(\mathbf{r})\mathrm{d}\mathbf{r}'\mathrm{d}\mathbf{r},\end{aligned} \tag{3.2}$$

with m the particle mass. The first integral gives the kinetic energy, the second integral the one from an external potential $V_{\mathrm{ext}}(\mathbf{r})$ and the last integral yields the interaction energy.

For the low energies involved in typical atomic BECs, the scattering processes are dominated by s-wave scattering. The precise shape of the interparticle potential is not relevant and the potential can be replaced by a contact interaction [62]

$$V(\mathbf{r}'-\mathbf{r}) \to g\delta(\mathbf{r}'-\mathbf{r}), \tag{3.3}$$

with the interaction constant

$$g = \frac{4\pi\hbar^2}{m}a_s. \tag{3.4}$$

We introduced the scattering length a_s, which is a quantitative measure of the magnitude of the resulting effective interaction that is agnostic to the true shape of the original potential. More details on this in the context of the experiment and how to tune it dynamically can be found in section 5.4.

3.1 Mean Field Approximation

In the context of low temperatures and weak interactions, the number of particles in the ground state N_0 is large. A reasonable approximation is replacing the creation and annihilation operators of the ground state by $\sqrt{N_0}$. Effectively this replaces the ground state part of the field operator with a classical field defined via its mean value

$$\hat{\phi}_0(\mathbf{r}) = \psi_0(\mathbf{r})\hat{a}_0 \sim \sqrt{N_0}\psi_0(\mathbf{r}) \equiv \phi_0(\mathbf{r}) \tag{3.5}$$

Therefore, this Bogoliubov approximation is oftentimes called mean field approximation. Errors in this approximation occur whenever commutators of the original operators appear and are of the order $1/N_0$. This is also the reason why the same approximation can not be applied to the less occupied higher energy states, such that the new field operator reads

$$\hat{\Phi}(\mathbf{r}) = \phi_0(\mathbf{r}) + \delta\hat{\Phi}(\mathbf{r}) \tag{3.6}$$

where $\delta\hat{\Phi}(\mathbf{r})$ denotes the sum over all the higher states as in Equation (3.1) and can be interpreted as the fluctuations on top of the condensed fraction, which is well described by this classical field.

The Gross-Pitaevski Equation

If the fluctuations can be neglected (e.g. for large particle numbers N), the field operator reduces to a classical field $\phi(\mathbf{r})$ - often called the order parameter - and the time evolution generated by the full Hamiltonian (Eq. 3.2) reduces to the Gross-Pitaevskii equation (GPE)

$$\left(-\frac{\hbar^2}{2m}\nabla^2 + V_{\text{ext}}(\mathbf{r}) + g|\phi(\mathbf{r})|^2\right)\phi(\mathbf{r}) = i\hbar\partial_t\phi(\mathbf{r}). \tag{3.7}$$

Note that $|\phi(\mathbf{r})|^2$ is just the density distribution $n(\mathbf{r})$. For a vanishing external potential and a uniform density distribution we find for the ground state

$$i\hbar\partial_t\phi_0(\mathbf{r}) = gn \equiv \mu, \tag{3.8}$$

where we introduced the chemical potential μ.

If we keep the external potential in the GPE but discard the kinetic term, we get

$$\left(V_{\text{ext}}(\mathbf{r}) + g|\phi(\mathbf{r})|^2\right)\phi(\mathbf{r}) = \mu\phi(\mathbf{r}). \tag{3.9}$$

This is called Thomas-Fermi approximation. Its solution

$$n(\mathbf{r}) = \frac{\mu - V_{\text{ext}}(\mathbf{r})}{g} \tag{3.10}$$

is a good first approximation for the ground state density profile of a trapped BEC [63]. The approximation breaks down if the kinetic energy from the curvature of the density profile is of the order of the interaction energy. This happens, for example, at the edges of a box trap where the potential changes abruptly. Instead of showing the same jump, the density changes smoothly on the order of the healing length (defined in the next section, Eq. 3.19). The GPE can also be used to approximate the time evolution of the system in an excited state. The mean field approximation including the excited states is only justified if all the excited states that generate the dynamics have occupations much larger than one.

3.2 Bogoliubov Quasi-Particles

We now consider the regime of a highly occupied ground state, but small occupation of the excited states. For this, we set the external potential to a box of volume V. The single particle states in Equation (3.1) take the form of discrete box modes that are momentum eigenstates, such that we can sum over momenta $\mathbf{k}$. We get the Hamiltonian in momentum space [63]

$$\hat{H} = \sum_{\mathbf{k}} \frac{\hbar^2 k^2}{2m} \hat{a}^\dagger_{\mathbf{k}} \hat{a}_{\mathbf{k}} + \frac{g}{2V} \sum_{\mathbf{k_1},\mathbf{k_2},\mathbf{q}} \hat{a}^\dagger_{\mathbf{k_1}-\mathbf{q}} \hat{a}^\dagger_{\mathbf{k_2}+\mathbf{q}} \hat{a}_{\mathbf{k_1}} \hat{a}_{\mathbf{k_2}}, \tag{3.11}$$

where the first term is now simply the particle number operator for each mode $\mathbf{k}$ multiplied by its kinetic energy and the second term includes all two particle scattering processes with conserved net momentum.

Again, we approximate $\hat{a}^\dagger_0, \hat{a}_0 \sim \sqrt{N_0}$ and keep all terms up to quadratic order for $\mathbf{k} \neq 0$. This is done by keeping only combinations of $\mathbf{k_1}$, $\mathbf{k_2}$ and $\mathbf{q}$ for which maximally two of the four indices ($\mathbf{k_1} - \mathbf{q}$,$\mathbf{k_2} - \mathbf{q}$, $\mathbf{k_1}$ and $\mathbf{k_2}$) are non-zero. This leaves only combinations of $\pm\mathbf{k}$ and we get

$$\hat{H} = \frac{gN_0^2}{2V} + \sum_{\mathbf{k}\neq 0} \frac{\hbar^2 k^2}{2m} \hat{a}^\dagger_{\mathbf{k}} \hat{a}_{\mathbf{k}} + \frac{gN_0}{2V} \sum_{\mathbf{k}\neq 0} \left(4a^\dagger_{\mathbf{k}} \hat{a}_{\mathbf{k}} + \hat{a}^\dagger_{\mathbf{k}} \hat{a}^\dagger_{-\mathbf{k}} + \hat{a}_{\mathbf{k}} \hat{a}_{-\mathbf{k}} \right). \tag{3.12}$$

This can be rewritten in a symmetric form

$$\hat{H} = \frac{gN^2}{2V} + \frac{1}{2} \sum_{\mathbf{k}\neq 0} \left[\left(\frac{\hbar^2 k^2}{2m} + gn_0 \right) (a^\dagger_{\mathbf{k}} \hat{a}_{\mathbf{k}} + a^\dagger_{-\mathbf{k}} \hat{a}_{-\mathbf{k}}) + gn_0 (\hat{a}^\dagger_{\mathbf{k}} \hat{a}^\dagger_{-\mathbf{k}} + \hat{a}_{\mathbf{k}} \hat{a}_{-\mathbf{k}}) \right], \tag{3.13}$$

where the symmetry in $\mathbf{k}$ was used, n_0 is defined as $n_0 = N_0/V$ and $N = \langle \hat{N} \rangle$. For details, see reference [63] where this was adapted from. We note that the single particle states that are the eigenstates of $a^\dagger_{\mathbf{k}} \hat{a}_{\mathbf{k}}$, are not eigenstates of the interacting Hamiltonian because of the off-diagonal terms in the last brackets.

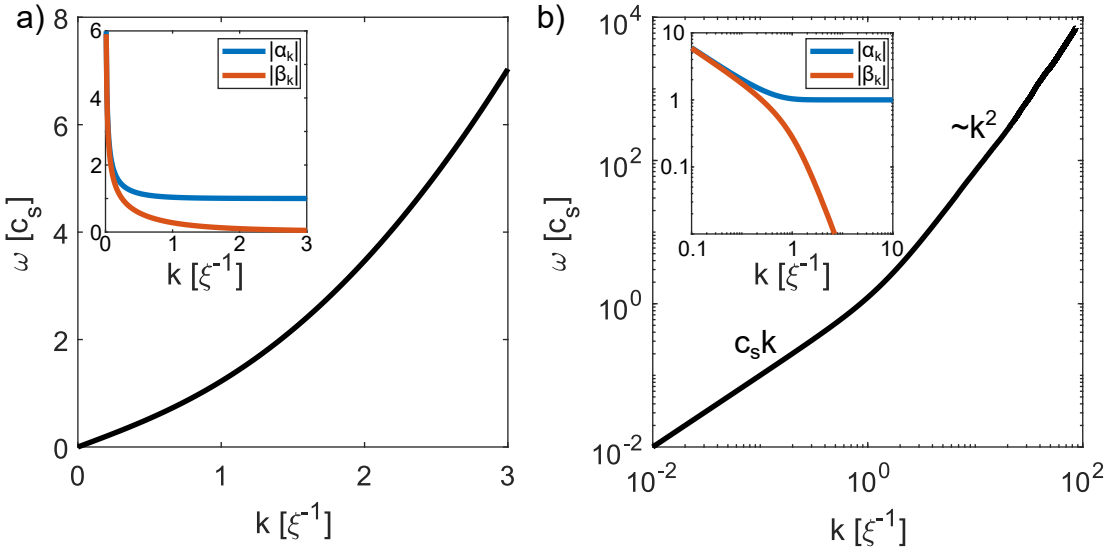

Figure 3.1: Bogoliubov dispersion relation in linear (a) and double logarithmic scale (b). The transition scale from a linear relation at low momenta to a quadratic one at higher momenta is given by $k = \xi^{-1}$ (unity in the chosen scale). This is best seen in subplot (b). Insets show the absolute values of the corresponding Bogoliubov coefficients α_k and β_k. Even though the experiments shown in this thesis include different ξ and a wide momentum range is analyzed, these are typically in the regime of ξ^{-1} ($k \in [0.1\xi^{-1}, 3\xi^{-1}]$).

The Bogoliubov Dispersion

We can express the Hamiltonian in terms of its energy eigenstates if we diagonalize the Hamiltonian with a Bogoliubov transformation. We introduce the quasi-particle creation (and annihilation) operators

$$\hat{b}^\dagger_{\mathbf{k}} = \alpha_k \hat{a}^\dagger_{\mathbf{k}} + \beta_k \hat{a}_{-\mathbf{k}}, \tag{3.14}$$

for which we have the usual Bosonic commutation relations and the normalization condition just like in the last chapter (Eq. 2.18). We find the Bogoliubov coefficients

$$|\alpha_k|^2 = \frac{1}{2}\left(\frac{\frac{\hbar^2 k^2}{2m} + gn_0}{\hbar\omega_k} + 1\right), \quad |\beta_k|^2 = \frac{1}{2}\left(\frac{\frac{\hbar^2 k^2}{2m} + gn_0}{\hbar\omega_k} - 1\right). \tag{3.15}$$

that diagonalize the Hamiltonian

$$\hat{H} = E_0 + \sum_{\mathbf{k}} \hbar\omega_k \hat{b}^\dagger_{\mathbf{k}} \hat{b}_{\mathbf{k}}, \tag{3.16}$$

with the ground state energy E_0. For real weakly interacting gases E_0 is dominated by $gN^2/(2V)$ like one expects from Equation (3.13). Here it diverges with

the sum over all momenta (because of a commutator $[\hat{a}_k^\dagger, \hat{a}_k]$ leaving us with a factor $-\hbar\omega_k|\beta_k|^2$). The divergence is a consequence of the choice of the contact interaction (for details, see reference [63]).
The eigenfunctions of this Hamiltonian are the quasi-particles that are created by the $\hat{b}_k^\dagger$ creation operators. They are non-interacting (for this quadratic order of approximation) and have eigenenergies given by the Bogoliubov dispersion relation

$$\hbar\omega_k = \sqrt{\frac{\hbar^2 k^2}{2m}\left(\frac{\hbar^2 k^2}{2m} + 2gn_0\right)}. \tag{3.17}$$

For low momenta, we find a linear behavior $\omega_k = c_s k$, with

$$c_s = \sqrt{\frac{gn_0}{m}}, \tag{3.18}$$

defining the speed of sound. For high momenta, we find the quadratic dispersion relation of the free particles. This is depicted in Figure 3.1. We can understand this by looking at the momentum dependence of the Bogoliubov coefficients α_k and β_k that are shown as insets in Figure 3.1. At high momenta, $|\alpha_k| \to 1$ and $|\beta_k| \to 0$. The quasiparticles are simply the free particles and we get the dispersion relation of the original atoms. At low momenta, however, both coefficients are almost equally large and the quasiparticles are a superposition of the $\mathbf{k}$ and $-\mathbf{k}$ modes. This gives them a phononic character and the dispersion relation of massless particles. We will call this the acoustic regime throughout this thesis. The relevant scale to differentiate the two is given by the balance of kinetic and interaction energy. The healing length ξ defined as

$$\xi^2 = \frac{\hbar^2}{2mgn_0}, \tag{3.19}$$

is the inverse of the momentum $k = \xi^{-1}$ that marks this balance. Indeed, we find the transition between the two regimes in Figure 3.1 b) at $k = \xi^{-1}$. Because of the smooth character of the transition, we will later see its influence over a broad range of momenta.
Like in the previous chapter, the new operators also come with their own vacuum state. It is the lowest energy state of the Hamiltonian and fulfills $\hat{b}_k|0\rangle = 0$. Again, this is different from the vacuum of the free particle operators. In other words, not all atoms are in the ground state, even though this is the lowest energy state ($T = 0$). This is a result from the interaction and called quantum depletion of the the ground state ([63]).
The condition we set on the quasi-particle operator, namely to diagonalize the Hamiltonian, is identical to the one we had in the previous chapter where we restricted the mode equations in region I and III to plane waves (see Eq. 2.17). The Bogoliubov coefficients that led to the creation and annihilation operators in region III are very different, however, because they mapped the result from the time-dependent operators in region II to the (quasi-)particle operators.

3.3 Quasi-Two-Dimensional Condensates

In our experiments, the BEC is strongly confined in the z-direction (aligned with gravity). This is achieved with a repulsive light potential described in section 5.3.2. Around the potential minima this is well approximated by a harmonic potential $V_{\text{ext}}(z) = m\omega_z^2 z^2/2$. If the energy spacing $\hbar\omega_z$ of the transverse confinement is larger than the energy scales involved in the system, only the ground state is occupied (in z-direction) and the system can be considered quasi-two-dimensional. We can then describe it with an effective two-dimensional theory.

On the mean field level, we can replace the order parameter in z-direction with the ground state of the harmonic oscillator

$$\phi_0(z) = \frac{1}{\pi^{\frac{1}{4}} l_z^{\frac{1}{2}}} e^{-\frac{z^2}{2l_z^2}}, \tag{3.20}$$

with the harmonic oscillator length $l_z = \sqrt{\hbar/(m\omega_z)}$. The ground state in z-direction factorizes with the new two-dimensional order parameter and density $|\phi(\mathbf{r}_\perp)|^2 = n_{\text{2D}}(\mathbf{r}_\perp)$. After integrating out the z-direction, we find the same set of equations for kinetic energy and potential energy, where all integrals (and sums) now run over two dimensions. The exception is a ground state energy shift of $\hbar\omega_z/2$ from confinement. For the interaction, however, integrating out the z-direction yields an effective interaction constant for two dimensions

$$g_{\text{2D}} = \frac{g}{\pi l_z^2} \int e^{-2\frac{z^2}{l_z^2}} \mathrm{d}z = g\sqrt{\frac{1}{2\pi l_z^2}} = \sqrt{\frac{8\pi\hbar^3\omega_z}{m}} a_s. \tag{3.21}$$

This is only a result of the density distribution in the z-direction. The character of the interaction is still three dimensional, as in our regime $a_s \ll l_z$. This is important for the applicability of the mean field approximation [61].

All the equations we derived in this chapter are now equally applicable to the quasi-two-dimensional system, simply by replacing g with g_{2D}. From now on, we will drop the 2D index for everything except the interaction parameter g_{2D}.

4
Analog Cosmology

The basic idea of analog gravity and analog cosmology is to map the differential geometry necessary to describe general relativity as well as a (quantum) field theory to describe (quasi-) particle excitations onto a hydrodynamic theory. In other words, given the right set of parameters, the excitations of a fluid should behave as if they were subject to a curved spacetime. Quantized sound waves in the fluid (phonons) play the role of the excitations of the quantum field, while the speed of sound in the fluid sets a physical scale connecting time- and space-like dimensions, analogous to the speed of light. While we assume the speed of light to be constant in space and time, the speed of sound in a fluid can depend on various parameters. Spatial and temporal changes of the speed of sound, as well as fluid flows, can then be used to mimic a variety of spacetime structures for the phonons.

As laid out in chapter 1, analog gravity was first proposed by Bill Unruh [17], where he brought up the idea to simulate a black holes event horizon and the creation of Hawking radiation in a moving fluid.

Similarly in analog cosmology, one can simulate particle production in isotropic and homogeneous cosmologies like described in chapter 2. In this case, the fluid is stationary and the change in scale factor is implemented via a dynamic change of the interaction strength. This section includes the details of how to connect our BEC system with a scalar quantum field in curved spacetimes. For an even more in-depth discussion, see reference [49] where this was developed for our system. Afterwards, we show the connection between speed of sound (or light) and the scale factor. We take the full Bogoliubov dispersion into account and find that the analogy can still be applied if we consider a momentum depended scale factor (or potential). Finally, we look at the quantities that we extract from the experiment and how to relate them to the excitation power spectrum from before. We find that this changes in context of the dispersion. These final two sections are based on unpublished work by our theory collaborators [64].

4.1 Definition of the Fluctuation Field

We start similar to the last chapter, but will describe the BEC through the action of a complex scalar field. By choosing a certain splitting of the fluctuations into two real fields and with a few restrictions, namely no flow of the background condensate and momenta in the acoustic regime, we will find an effective field theory with the action in the form of the action of the scalar field in curved spacetimes in Equation (2.1). In later sections, we again lift the restriction on the low-momentum regime.

The complex scalar field Φ that describes a two-dimensional BEC has the action:

$$\Gamma[\Phi] = \int dt d^2r \left[i\hbar\Phi^* \left(\partial_t + iA_0\right)\Phi - \frac{\hbar^2}{2m}(\nabla - iA)\Phi^*(\nabla + iA)\Phi - \frac{g_{2D}}{2}(\Phi^*\Phi)^2 \right] \tag{4.1}$$

with the gauge field $\boldsymbol{A} = (A_0, A)$, which only includes the external potential $A_0 = V/\hbar$. Similar to the splitting after the Bogoliubov approximation (Eq. 3.6), we can split this field Φ into background field ϕ_0 and fluctuations

$$\Phi = \phi_0 + \frac{1}{\sqrt{2}}(\phi_1 + i\phi_2), \tag{4.2}$$

where the fluctuations itself are split into the two real fields $\phi_{1/2}$. The background field is, again, a solution of the mean field GPE (Eq. 3.7) and can be represented by background density n_0 and phase S_0

$$\phi_0 = \sqrt{n_0}e^{iS_0}. \tag{4.3}$$

With this definition and using the gauge freedom of Equation (4.1), ϕ_1 can be interpreted as the in-phase component of the fluctuation field relative to the background field and ϕ_2 as the out-of-phase component (if the background phase is flat). As a result of the gauge transformation $\Phi \to e^{-iS_0}\Phi$, the gauge field $\boldsymbol{A}$ is modified to $A_0 = V/\hbar + \partial_t S_0$, $A_i = \partial_i S_0$.

Because ϕ_0 is a solution to the GPE, we can plug Equation (4.3) into the GPE and get particle conservation

$$0 = \partial_t n_0 + \nabla(n_0 v), \tag{4.4}$$

from the imaginary coefficients and energy conservation

$$0 = \hbar\partial_t S_0 + V + g_{2\mathrm{D}} n_0 + \frac{1}{2}mv^2 + q, \tag{4.5}$$

from the real coefficients. Here, we introduced the background velocity

$$v = \frac{\hbar}{m}\nabla S_0, \tag{4.6}$$

and the quantum pressure

$$q = -\frac{\hbar^2\nabla^2\sqrt{n_0}}{2m\sqrt{n_0}}. \tag{4.7}$$

With this, one can expand the action around the background field solution ϕ_0. When extremizing the action, the relevant terms depend on the fluctuations ϕ_1 and ϕ_2 to quadratic order (including mixed terms), because linear terms vanish at the extremum. Terms that only depend on ϕ_0 are already solved by the mean-field solution. We get the quadratic contribution [64]

$$\begin{aligned}\Gamma_2[\phi_1,\phi_2] = \int dtd^2r \Bigg[&\hbar\phi_2\partial_t\phi_1 - \frac{\hbar^2}{4m}\left((\nabla\phi_1)^2 + (\nabla\phi_2)^2\right) \\ &-\frac{1}{2}\left(V + \hbar\partial_t S_0 + \hbar^2\frac{(\nabla S_0)^2}{2m}\right)\left(\phi_1^2+\phi_2^2\right) \\ &-\frac{\hbar^2}{2m}(\nabla S_0)\left(\phi_1\nabla\phi_2 - \phi_2\nabla\phi_1\right) - \frac{g_{2D}n_0}{2}\left(3\phi_1^2+\phi_2^2\right)\Bigg]\end{aligned} \tag{4.8}$$

where $n_0 = |\phi_0|^2$ was used. Using Equation (4.5), Γ_2 can be simplified to

$$\begin{aligned}\Gamma_2[\phi_1,\phi_2] = \int dtd^2r \Bigg[&\frac{1}{2}\phi_2\left(\frac{\hbar^2}{2m}\nabla^2 + q\right)\phi_2 + \frac{1}{2}\phi_1\left(-2g_{2\mathrm{d}}n_0 + \frac{\hbar^2}{2m}\nabla^2 + q\right)\phi_1 \\ &-\phi_1\left(\hbar\partial_t\phi_2 + \frac{1}{2}v\nabla\phi_2 + \frac{\hbar^2}{2m}(\nabla^2 S_0)\phi_2\right)\Bigg].\end{aligned} \tag{4.9}$$

The Acoustic Approximation

Going further, we make multiple approximations. First, we assume that the background velocity is constant, that is, $\nabla^2 S_0 = 0$. Second, we neglect the quantum pressure. This is justified if the background density is flat (or at least slowly varying in comparison to other scales in the BEC). Finally, we rule out background flows altogether and set $v = 0$. This step is not necessary to find an acoustic metric but will lead to the FLRW-metrics (see App. D). With these approximations, one obtains the equations of motion from variation of Γ_2 [64]:

$$\left(2n_0 g_{2\mathrm{D}} - \frac{\hbar^2}{2m}\nabla^2\right)\phi_1 + \hbar\partial_t\phi_2 = 0, \text{ and} \tag{4.10}$$

$$\frac{\hbar^2}{2m}\nabla^2\phi_2 + \hbar\partial_t\phi_1 = 0. \tag{4.11}$$

Note that the field ϕ_1 has an additional contribution $2n_0 g_{2\mathrm{D}}$ from the interaction with the background. If we assume this is dominating over the kinetic term $\frac{\hbar^2}{2m}\nabla^2\phi_1$, we can drop this and obtain

$$\phi_1 = -\frac{\hbar}{2n_0 g_{2\mathrm{D}}}\partial_t\phi_2. \tag{4.12}$$

This is referred to as the acoustic approximation, because it is the same as going to the low-momentum limit of the Bogoliubov dispersion (3.17) where quasi-particles are phonons. We will see that this is not always justified and discuss the consequences in section 4.2.2. The real part of the fluctuations ϕ_1 can be integrated out of the action. By redefining $\phi = \frac{1}{\sqrt{2m}}\phi_2$ we end up with the final form of the effective action

$$\Gamma_2[\phi] = \frac{\hbar^2}{2}\int dt d^2r \left[\frac{1}{c_s^2}\left(\partial_t\phi\right)^2 - \left(\nabla\phi\right)^2\right] \tag{4.13}$$

where the speed of sound in the condensate $c_s = \sqrt{\frac{g_{2\mathrm{D}} n_0}{m}}$ (Eq. 3.18) was used. The next section shows how this is related to the definition of the acoustic metric.

4.2 The Effective Metric and the Scale Factor

To show that the action for ϕ is the action of a free relativistic scalar field in curved spacetime, c_s is used to a define a metric

$$(g_{\mu\nu}) = \begin{pmatrix} -1 & 0 \\ 0 & c_s^{-2}\delta_{ij} \end{pmatrix} \tag{4.14}$$

together with its inverse

$$(g^{\mu\nu}) = \begin{pmatrix} -1 & 0 \\ 0 & c_s^{2}\delta^{ij} \end{pmatrix} \tag{4.15}$$

With $\sqrt{g} = \sqrt{-\det(g_{\mu\nu})} = 1/c_s^2$ Equation (4.13) can now be rewritten in the desired form:

$$\Gamma_2[\phi] = -\frac{\hbar^2}{2}\int dt d^2r \sqrt{g} g^{\mu\nu}\partial_\mu\phi\partial_\nu\phi. \tag{4.16}$$

This is the form of a massless scalar field in curved spacetime (compare to Eq. 2.1). At first glance, the newly found metric in Equation (4.14) looks like the flat Minkowski metric (with signature (-,+,+)) and we get the line element ds^2

$$\begin{aligned} \mathrm{d}s^2 &= g_{\mu\nu}\mathrm{d}x^\mu \mathrm{d}x^\nu \\ &= -\mathrm{d}t^2 + c_s^{-2}\left(\mathrm{d}x^2 + \mathrm{d}y^2\right). \end{aligned} \tag{4.17}$$

Because c_s is not a physical constant, this metric is not necessarily restricted to the Minkowski metric. By making the speed of sound a function of space and time, it can be used to implement spatial curvature and time dependent scale factors.

4.2.1 Expanding Spacetimes - Time-Dependent Scale Factor

In cosmology, the metric is typically defined, such that the speed of light c is multiplied with the time coordinate, giving the product the units of space. We define x and y as co-moving coordinates of space. This means objects that are stationary in space (relative to this choice of coordinates) keep their coordinates fixed. The expansion of space and an increasing distance is encoded in an increasing dimensionless scale factor $\lambda(t)$

$$\mathrm{d}s^2 = -c^2\mathrm{d}t^2 + \lambda(t)^2\left(\mathrm{d}x^2 + \mathrm{d}y^2\right). \tag{4.18}$$

Photons move at the speed of light such that $ds^2 = 0$. For two objects A and B that are stationary in our co-moving coordinates, we can measure the proper distance (including the scale factor) by measuring the time it takes for light to go from A to B (and back). As illustrated in Figure 4.1, this time only depends on the ratio λ/c but not on their actual values. This can be shown formally by setting $ds^2 = 0$ in the line element (4.18). In cosmology this freedom is typically used to set the current value of λ to one and thus set the co-moving distance to today's proper distance.

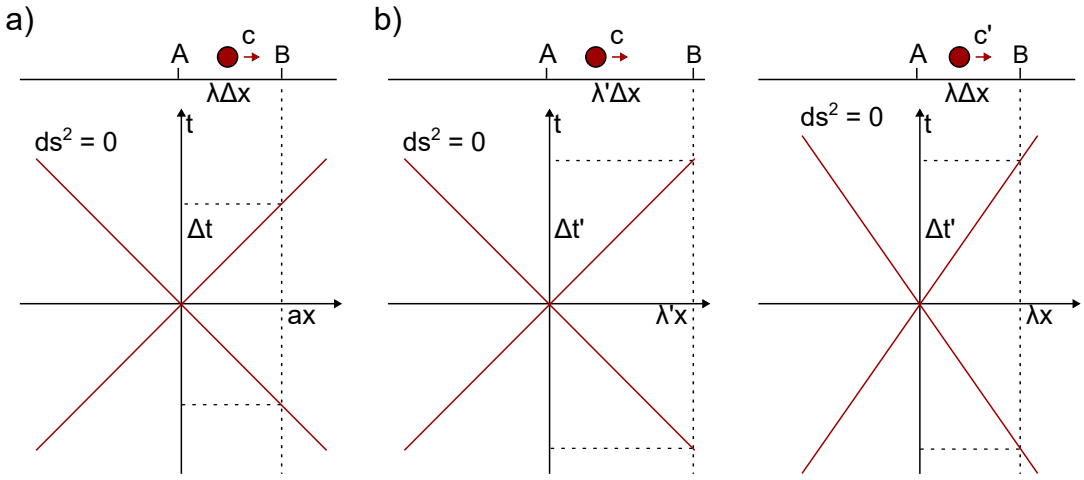

Figure 4.1: a) Two observers A and B that are stationary relative to each other, measure the scale of their spacetime by performing a round trip experiment. B sends out a photon (phonon) that is traveling at the speed of light c (c_s). As soon as the signal reaches A, it is sent back. B can measure the time Δt, between sending and receiving the signal. Origin of the spacetime diagram shown is the spacetime-coordinate in which A receives the signal. b) The two observers repeat the same experiment, but measure a larger time $\Delta t'$. They can not distinguish between an increase of the scale factor $\lambda \to \lambda'$ and a decrease of the speed of light $c \to c'$.

Because the speed of sound is not a fundamental constant and we change it to mimic an expanding scale factor, we employ this freedom to combine c_s and λ to the scale factor $a = 1/c_s$

$$\mathrm{d}s^2 = -\mathrm{d}t^2 + a(t)^2 \left(\mathrm{d}x^2 + \mathrm{d}y^2\right). \tag{4.19}$$

giving our coordinates the units of time. The phononic excitations of the fluctuation field ϕ are massless (relativistic). They also obey $ds^2 = 0$, which means that they are moving along the geodesics of this metric at the speed of sound. The geodesics are the curved spacetime equivalent to straight lines in flat space and given by the curves with tangent vectors along the curve at all points. In other words, this is a generalization of going straight and describes the path of an object without external forces. The shortest path between two points A and B is a subsection of a geodesic through both points. We measure the spatial distances between two points A and B in our condensate in units of time, that is, the time it takes for a phonon to cover the distance between A and B. For a constant scale factor, the geodesics also define sound cones that are analogous to light cones in cosmology. Imagine a 2+1-dimensional version of the 1+1-dimensional spacetime diagram in Figure 4.1, in which the red $ds^2 = 0$ lines form a cone. In our example, the scale factor is different between (a) and (b), but does not change on the timescale of the round-trip experiment. A scale factor that is dynamic on these timescales would result in a curvature of the sound cones.

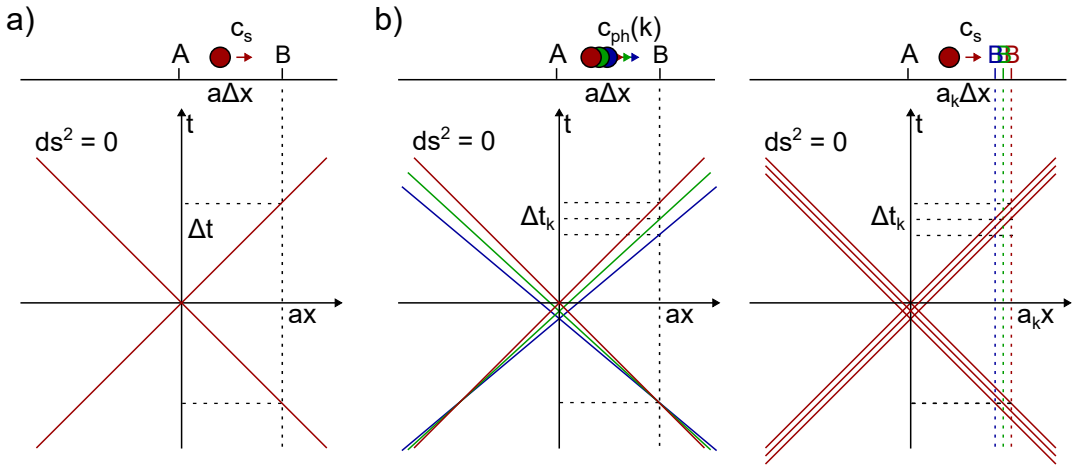

Figure 4.2: a) Two observers A and B that are stationary relative to each other measure the scale of their spacetime by performing a round trip experiment (same as in Fig. 4.1, but specific to the analog case). b) If the kinetic energy difference of the quasiparticles can not be neglected, a pulse sent out by B disperses according to the difference in phase velocities. Higher energies (blue) complete the round trip faster then lower ones (red). This is also the case if the metric is made momentum dependent. Now all momenta move at c_s but are sent and received at different proper distances.

The explicit time dependence of the scale factor is implemented through a time-dependence of the speed of sound. To implement an expansion where the scale factor increases in time, the speed of sound is dynamically decreased. In turn, the time it takes for a phonon to go from A to B is increased. This is implemented by making the interparticle-interaction g_{2D} time dependent through a magnetic Feshbach resonance and is explained in more detail in context of the experimental apparatus in section 5.4 and the experimental results in chapter 6. Because the physical size of the BEC does not change, we can take the lab coordinates as our comoving coordinates.

Because the speed of sound depends on the density $n(\mathbf{x})$, it can change throughout the condensate. This can be used to implement spatial curvature. A detailed description of how this is done can be found in [65]. Experimental results can be found in [47] and [66].

With the combined capability of an adjustable scale factor and spatial curvature, all parameters of the FLRW-metric can be adjusted. Because the curvature is on the order of the size of the condensate, the energy shifts from the curvature are small and have minor effects on the particle production process. For a complete treatment including the set of eigenfunctions and eigenenergies in both positively curved spaces and negatively curved spaces, refer to [49]. All the experiments shown in this thesis are performed with flat density distributions that correspond to no spatial curvature.

4.2.2 Rainbow Metric

So far, our ability to describe the fluctuations of the BEC in terms of a massless scalar field in curved spacetime relied on the assumption that the fluctuations are phononic. This ensures that they move at the speed of sound. Theoretically, this was implemented by applying the acoustic approximation ($2n_0 g_{2\mathrm{D}}\phi_1 \gg \frac{\hbar^2}{2m}\nabla^2\phi_1$) leading from Equation (4.11) to Equation (4.12).

However, this is only justified in the low-momentum regime. If one does not apply this approximation, one can still define a metric via the phase velocities $c_{\mathrm{ph}}(k)$

$$(g_{\mu\nu}) = \begin{pmatrix} -1 & 0 \\ 0 & c_{\mathrm{ph}}^{-2}(k)\delta_{ij} \end{pmatrix}, \tag{4.20}$$

where the phase velocity set a momentum dependent inverse scale factor $a_k = c_{\mathrm{ph}}^{-1}(k)$ and is calculated from the Bogoliubov dispersion

$$c_{\mathrm{ph}}(k) = \frac{\omega_{\mathrm{Bog}}(k)}{k} = c_s\sqrt{1 + \frac{1}{2}k^2\xi^2}. \tag{4.21}$$

Because this introduces a dispersion in the metric, this is sometimes referred to as the rainbow metric [37].

Figure 4.2 illustrates the effect of incorporating the dispersion in the scale factor $a \to a_k$. Then a_k simply replaces the original one in the mode equation for region II

$$\ddot{v}_k(t) + 2\frac{\dot{a}_k(t)}{a_k(t)}\dot{v}_k(t) + \frac{k^2}{a_k^2(t)}v_k(t) = 0. \tag{4.22}$$

In this form, it can be solved for every momentum mode as before.

To regain a single scale factor that is valid for all momenta, we can put the dispersive factor in rescaled mode functions

$$v_k(t) = a^{-1/2}(t)\sqrt{1 + \tfrac{1}{2}k^2\xi^2(t)}\psi_k(t). \tag{4.23}$$

This way, we can unambiguously define conformal time $\mathrm{d}\eta = \frac{1}{a(t)}\mathrm{d}t$ and write the mode function in form of the Schrödinger equation

$$\left(-\frac{\mathrm{d}^2}{\mathrm{d}\eta^2} + V_k(\eta)\right)\psi_k(\eta) = k^2\psi_k(\eta), \tag{4.24}$$

albeit with a potential that is momentum dependent

$$V_k(\eta) = \frac{\xi^{-4}(\eta) - 5k^2\xi^{-2}(\eta) + 4k^4}{4(\xi^{-2}(\eta) + k^2/2)^2}\dot{a}^2(\eta) + \frac{1}{2}\frac{\xi^{-2}(\eta) - k^2/2}{\xi^{-2}(\eta) + k^2/2}\ddot{a}(\eta)a(\eta) - \frac{1}{2}k^4\xi^2(\eta). \tag{4.25}$$

For $k \ll \xi^{-1}$ we recover the original form of the acoustic limit (Eq. 2.34). The last term introduces the dispersion, now in the form of a momentum-dependent potential offset. Especially, the term proportional to $\ddot{a}(\eta)$ is less important at high momenta. Because $\xi(\eta)$ changes as the scale factor does, this introduces an additional time dependence. This is part of ongoing work ([64]).

4.3 Extraction of Observables

Ultimately, we want to extract the spectrum of fluctuations S_k, which we can calculate from the connected correlation function $G_{\pi\pi}$ by inverse transformation of (see Eq. 2.27, now $\hbar \neq 1$)

$$G_{\pi\pi}(t, \mathbf{x} - \mathbf{x}') = \frac{1}{2} \int \frac{\mathrm{d}^2\mathbf{k}}{2\pi} a_f^4 |\dot{v}_k(t)|^2 e^{i\mathbf{k}(\mathbf{x}-\mathbf{x}')} = \int \frac{\mathrm{d}^2\mathbf{k}}{2\pi} \frac{\omega_k a_f^2}{\hbar} S_k(t) e^{i\mathbf{k}(\mathbf{x}-\mathbf{x}')}. \tag{4.26}$$

However, we can not measure the canonical momentum field π directly. Instead, we always measure density distributions at some time t (see chapter 6). From these, we construct the density contrast

$$\delta_c(t, \mathbf{x}) = (n(t, \mathbf{x}) - n_0(\mathbf{x})) \frac{n_0^{\frac{1}{2}}(\mathbf{x})}{\bar{n}_0^{\frac{3}{2}}}, \tag{4.27}$$

where $n_0 = |\phi_0|^2$ and

$$n = |\Phi|^2 = |\phi_0|^2 + |\phi_0 \phi_1| + \mathcal{O}\left(\phi_1^2, \phi_2^2\right), \tag{4.28}$$

for our definition of the background and fluctuation fields (see Eq. 4.2). Note that we get an interference term between ϕ_0 and ϕ_1, but not for ϕ_2, due to this choice of splitting the fluctuations and their phase relative to the mean field ϕ_0. Experimentally, $n(t, \mathbf{x})$ would be a single experimental realization, where we get the density including all the fluctuations. The background density $n_0(\mathbf{x})$ is estimated by averaging many realizations. Finally, $\bar{n}_0$ denotes the density in a reference area in the center of the BEC. This is equal to the mean density n_0 if it does not depend on position, for example because of the implementation of curvature or experimental deviations.

From this density contrast, we now calculate the two-point correlations

$$G_{\mathrm{nn}}(t, \mathbf{x}, \mathbf{x}') \equiv \langle \delta_c(t, \mathbf{x}) \delta_c(t, \mathbf{x}') \rangle = \frac{1}{n_0} \langle \{\phi_1(t, \mathbf{x}) \phi_1(t, \mathbf{x}')\} \rangle_c = \frac{2}{n_0} G_{\phi_1\phi_1}(t, \mathbf{x}, \mathbf{x}'). \tag{4.29}$$

In the acoustic approximation, $\phi_1 = -\frac{\hbar}{2n_0 g_{2\mathrm{D}}} \dot{\phi}_2$ (Eq. 4.12). From $\pi = a_f^2 \dot{\phi}$ and $\phi = \frac{1}{\sqrt{2m}} \phi_2$ in our analog, we get

$$\begin{aligned} G_{\pi\pi} = \frac{m n_0}{\hbar^2} G_{nn} &= \int \frac{\mathrm{d}^2\mathbf{k}}{2\pi} \frac{\omega_k a_f^2}{\hbar} S_k(t) e^{i\mathbf{k}(\mathbf{x}-\mathbf{x}')} \\ \Rightarrow S_k(t) &= \frac{m n_0}{\hbar \omega_k a_f^2} \int \frac{\mathrm{d}^2\mathbf{k}}{2\pi} G_{nn} e^{-i\mathbf{k}(\mathbf{x}-\mathbf{x}')}, \end{aligned} \tag{4.30}$$

where we used $g_{2\mathrm{D}} n_0 = m c_s^2$ and $c_s = a_f^{-1}$. With this, we can extract the spectrum by performing a Fourier-transform of the density contrast correlations.

The Bogoliubov Prefactor to the Spectrum

If we are not within the acoustic regime, we get $\omega_k = \omega_{\mathrm{Bog}}(k)$ instead of $\omega_k = c_s k$. More importantly, we lose the simple relation Equation (4.12) between ϕ_1 and ϕ_2. In other words, ϕ_1 is no longer proportional to the conjugate field of ϕ.
Instead, we have to evaluate the equations of motion (4.11), including the kinetic energy. In momentum space, these still separate and we find

$$-\hbar\partial_t\phi_{2,\mathbf{k}} = \left(2g_{2\mathrm{D}}n_0 + \frac{\hbar^2k^2}{2m}\right)\phi_{1,\mathbf{k}}. \tag{4.31}$$

Because of this separation, we still get a spectrum albeit with more prefactors

$$\begin{aligned} G_{nn} &= \int \frac{\mathrm{d}^2\mathbf{k}}{2\pi}\frac{4m\hbar}{a_f^2 n_0}\frac{\omega_{\mathrm{Bog}}(k)}{\left(2g_{2\mathrm{D}}n_0 + \frac{\hbar^2k^2}{2m}\right)^2}S_k(t)e^{i\mathbf{k}(\mathbf{x}-\mathbf{x}')} \\ \Rightarrow S_k(t) &= \frac{a_f^2 m n_0}{\hbar k}c_{\mathrm{ph}}^3(k)\int\frac{\mathrm{d}^2\mathbf{k}}{2\pi}G_{nn}e^{-i\mathbf{k}(\mathbf{x}-\mathbf{x}')} \\ &= \frac{m^2c_s^3}{\hbar k g_{2\mathrm{D}}}\left(1+\frac{1}{2}k^2\xi^2\right)^{\frac{3}{2}}\int\frac{\mathrm{d}^2\mathbf{k}}{2\pi}G_{nn}e^{-i\mathbf{k}(\mathbf{x}-\mathbf{x}')}, \end{aligned} \tag{4.32}$$

where we used the phase velocity defined in Equation (4.21). Compared to the acoustic approximation, we get the extra prefactor $\left(1+\frac{1}{2}k^2\xi^2\right)^{\frac{3}{2}}$, which we will call the Bogoliubov prefactor in the following. All factors in front of the integral, but with the bracket to the power $\frac{1}{2}$ instead of $\frac{3}{2}$ can be related to the squeezing parameter [45]

$$\frac{m^2c_s^3}{\hbar k g_{2\mathrm{D}}}\left(1+\frac{1}{2}k^2\xi^2\right)^{\frac{1}{2}} = \frac{2n_0}{C}, \tag{4.33}$$

that is given by the ratio between the kinetic energy of the free particles and the Bogoliubov quasi-particles

$$C = \frac{\hbar k^2}{2m\omega_{\mathrm{Bog}}(k)}. \tag{4.34}$$

The density and consequently the correlations and its Fourier transform of the ground state will show less noise on long length scales, because of the interaction. This makes it like squeezed modes in the particle basis, although in the energy eigenbasis of the quasi-particles that we are considering, they are not. Because we are interested in $G_{\pi\pi} \sim G_{\dot{\phi}_2\dot{\phi}_2}$, we get the additional factor $\left(1+\frac{1}{2}k^2\xi^2\right)$ from Equation (4.31). When we discuss experimental spectra, we will always refer to the quantity defined in Equation (4.32) that can be compared with our expectation from Equation (2.28), including quasi-particle occupations N_k, coherent oscillations $\Delta N_k(t)$ and a vacuum noise level of 1/2. More details on this topic will be published in [64]. The experimental spectra are additionally corrected for a length-scale dependent imaging sensitivity (see section 5.5.3).

5
Experimental Platform

The core of the simulator used in this work is a quasi-two-dimensional Bose-Einstein condensate of potassium-39. This bosonic isotope of the alkali metal potassium is well-suited for simulation purposes because it has an almost freely tunable interaction strength. Together with an adjustable external potential, all terms of the Hamiltonian (see, for example, 3.2) can be experimentally tuned relative to the kinetic term. The other constituents of the simulator, namely the BEC preparation and readout of the density distribution, are also discussed in this chapter.

We start with the most important properties of ^{39}K and provide a very brief description of the cooling and condensation stages in our experiment. These are based on established mechanisms and have been well and comprehensively described in previous publications of the group, which will be referenced accordingly. More emphasis will be put on the description of the tunable interaction strength via a magnetic Feshbach resonance and the light potentials that form the final trap configuration and with that provide an adjustable external potential. Finally, the density readout via two-frequency absorption imaging will be covered in detail, especially its length scale (i.e. momentum)-dependent sensitivity arising from imaging aberrations.

5.1 Important Properties of Potassium-39

^{39}K is a bosonic isotope of potassium and the most abundant natural isotope. It is part of the alkali metals on the very left of the periodic table and thus has only one valence electron. Together with a nuclear spin of $I = 3/2$ (and electronic spin $S = 1/2$) we find the ground state $^2S_{1/2}$ and the excited states $^2P_{1/2}$ and $^2P_{3/2}$ that split due to spin-orbit coupling in $J = 1/2$ and $J = 3/2$. Transitions between the ground and these excited states define the $D1$ line at 770.1 nm and the $D2$ line at 766.7 nm respectively. These are shown in Figure 5.1 a). The cooling of the atoms

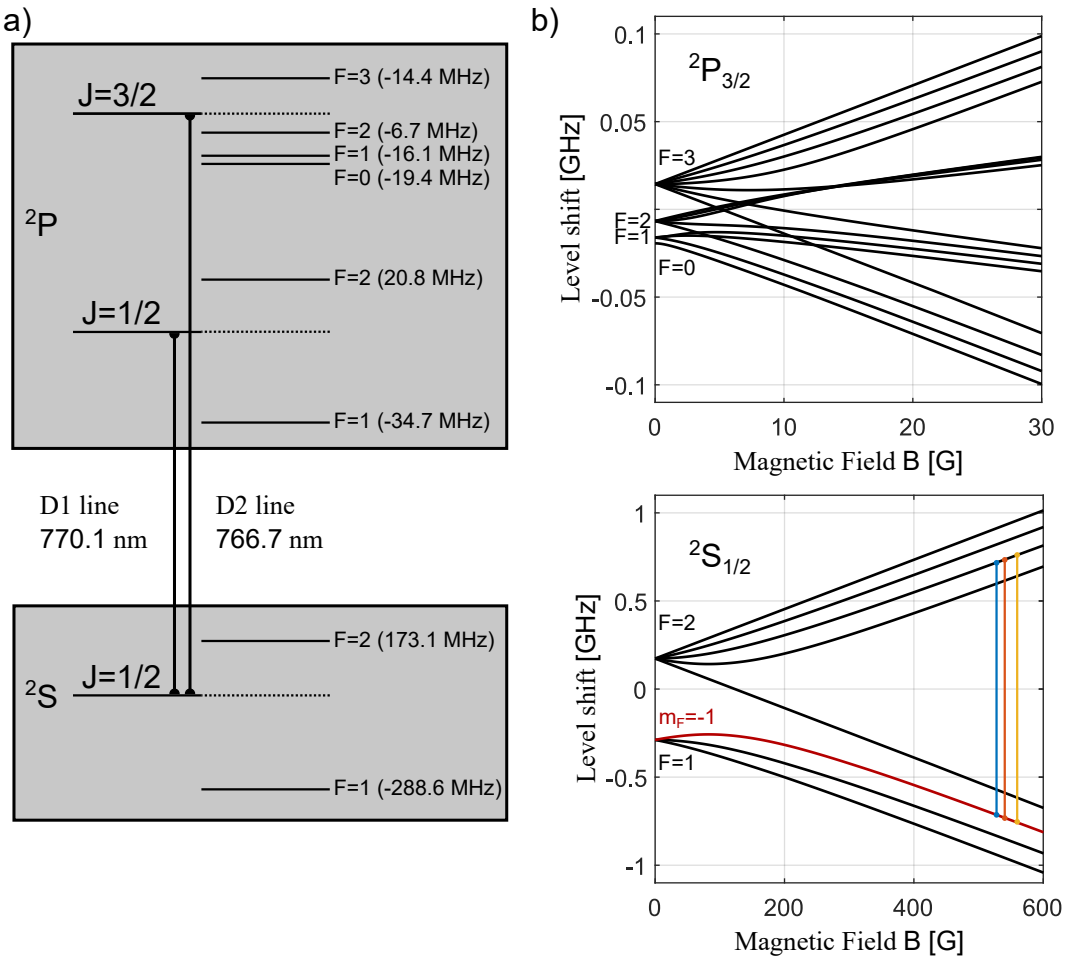

Figure 5.1: a) Level structure of ^{39}K showing the ground state $^2S_{1/2}$ and the excited states $^2P_{1/2}$ and $^2P_{3/2}$ as well as their hyperfine structure. b) Hyperfine splitting and level shift as a function of external magnetic field for the ground state $^2S_{1/2}$ and the excited state $^2P_{3/2}$. Marked in red is the state that is used in the experiments. This is the only substate of the $F = 1$ ground state manifold with positive magnetic moment at low magnetic fields. Colored vertical lines mark the microwave transitions used for the calibration of the magnetic field. Values to generate the diagrams are taken from [67].

in the magneto-optical traps and the imaging system make use of the $D2$ line. Sub-Doppler cooling with gray molasses adresses the $D1$ line. Both are described in the next section.

At zero magnetic field, the ground state and the excited state $^2P_{1/2}$ split into total angular momenta $F = 1$ and $F = 2$. The excited state $^2P_{3/2}$ splits into four hyperfine manifolds. Note that the ground-state splitting is much larger than the splitting of the excited states and not on an equal scale. Especially in the $^2P_{3/2}$ state, this splitting is small when compared to the natural linewidth of $\Gamma = 2\pi \times 6\,\mathrm{MHz}$.

Under an external magnetic field, each of these hyperfine manifolds splits into $2F + 1$ Zeeman sub-levels ($-F \leq m_\mathrm{F} \leq F$). This is shown in Figure 5.1 b) for the ground state and the excited state $^2P_{3/2}$. At low magnetic fields the energy shift of the sub-levels are (anti-)proportional to their magnetic quantum number m_F. For high magnetic fields, the interaction with the magnetic field dominates over the hyperfine interaction. The $|F, m_\mathrm{F}\rangle$ basis is no longer a good basis. For very high fields, m_I and m_J, instead the magnetic quantum numbers of the total electronic angular momentum J and the nuclear spin I form a good basis. Then, the energy shift is dominated by and proportional to the quantum number m_J. The four possible m_I states are almost parallel. This limit is reached at much lower fields for the $^2P_{3/2}$ state (see the difference in magnetic field axis in Figure 5.1 b). All experiments shown are performed in the energy eigenstate marked in red (subsequently called the experimental substate), that is selected via the magnetic trap. This state corresponds to the $|F = 1, m_\mathrm{F} = -1\rangle$ state at low field and the $|m_\mathrm{J} = -1/2, m_\mathrm{I} = -1/2\rangle$ at high fields. Our experiments will typically be performed between 540 G and 560 G, just below a magnetic Feshbach resonance of our experimental substate.

5.2 Production of the BEC

Vacuum System

To cross the BEC transition, the bosons need to have a high phase space density, that is, a combination of high density (in real space) and low temperature (high density in momentum space). For this, it is paramount to put the the atoms in ultra-high vacuum, minimizing collision with room-temperature background gas. Our vacuum system is divided into two parts, connected via a differential pumping stage (a tube of small diameter). The first part includes the potassium oven that is our atom source and is operated at a higher pressure (10^{-7} mbar to 10^{-8}mbar). The second part includes the glass cell that makes the science chamber where the BEC is produced ($< 10^{-11}$ mbar). A detailed description of the vacuum system can be found in [68]. Since then, the Rubidium oven and the coils in the vacuum system have been removed.

Magneto-Optical Traps

The first cooling stage is a two-dimensional Magneto-Optical Trap (MOT). Two pairs of counterpropagating laser beams are red detuned to the D2-line (767 nm, see

Fig. 5.1 a). Because of the Doppler-shift in the reference frame of a moving atom, scattering rates of the two counterpropagating beams are not equal. The rate is higher for the beam that propagates against the direction of movement of the atom. Because every scattering process includes a momentum transfer of $\hbar k_{\mathrm{phot}}$ from the laser to the atom, the atoms slow down rapidly. This cooling technique is known as optical molasses. The spontaneous emission in the scattering process is expected to be isotropic. Therefore, the net momentum will average to zero, however, the variance will be substantial. This variance equates to a velocity distribution and temperature limit for this technique known as the Doppler-limit. With this setup, the atoms are cooled, but not trapped. A magnetic field with a zero crossing in the center of the trap and gradients in all directions is added by a pair of coils in anti-Helmholtz configuration (opposite directions of current flow). This shifts the energy of the Zeeman sub-levels of the atom (low magnetic field region in Fig. 5.1 b)) as a function of distance from the trap center. With the right set of circular polarizations of the laser beams, this is used to produce a restoring force towards the center of the trap. The optical molasses and this kind of magnetic field and polarization configuration combine cooling and trapping in the MOT.

Ideally, a closed cycle is used as the cooling transition. This is the excitation from a ground state to an excited state, that can only decay back to the original ground state (due to the selection rules). For potassium-39, such a cycle exists between the $F = 2$ hyperfine manifold of the ground state and the $F = 3$ hyperfine manifold of the excited state $^2P_{3/2}$. This transition is driven by the cooling laser. However, the hyperfine splitting of the excited state is small, such that atoms can be lost into the ground state $F = 1$. Consequently, this is addressed by a second laser (repumper) that also drives the $D2$ transition. In practice both of these lasers are used with equal intensities and contribute to the cooling. For the first MOT in our setup, only two pairs of beams cool and trap the atoms in two dimensions. In the third dimension, a single beam accelerates the atoms through the differential pumping stage into the low-pressure science chamber.

In the science chamber, this stream of precooled atoms is trapped and cooled in a three-dimensional MOT. A compressed MOT stage is implemented by increasing the magnetic field and laser detunings towards the end of the MOT stage. Magnetic fields in the science chamber are generated by a pair of top and bottom mounted coils in anti-Helmholtz configuration that are also used for the magnetic trap and Feshbach fields.

All the near-resonant laser light is generated on a separate optical table and transferred to the experiment via fibers that can be shuttered to avoid resonant stray light at later stages of the experiment. The $D2$ lights are generated by a frequency-doubled fiber laser in the telecom wavelength range. This reference laser is locked via Doppler-free absorption spectroscopy on the crossover resonance of the $D2$ line via a potassium spectroscopy cell. From this, the detunings needed for the MOT are generated via acousto-optic-modulators (AOM), that shift the frequency for the two-dimensional MOT and the three-dimensional MOT as well as cooler and repumper independently.

The complete MOT setup can be found in [65]. Since then, the MOT beam from

the top had to be changed to pass through a top objective. This objective is used for the final trap described in 5.3.2. These changes to the setup can be found in [69]. A detailed description of the light generation can be found in [70]. The reference laser and a tapered amplifier have been replaced by the fiber laser that can be found in [71].

Gray-Molasses

Early experiments on optical molasses measured temperatures below the Doppler-limit [72]. This was explained by the Zeeman sub-level structure of the states, together with a position dependent polarization. Two counterpropagating laser beams with perpendicular polarization form a spatially varying polarization that changes periodically along their propagation axisover half their wavelength. This results in position-dependent light shifts (energy shifts) of the Zeeman sub-levels. The optical pumping rates between these sub-levels also depend on this local polarization. The pumping rate can be tuned (by detuning of the laser) to achieve a locally increased pumping rate from the state with a high internal energy at a given position to a state with lower internal energy. In this case, some energy is lost to the light field. Further movement will transform the low internal energy state into one of high internal energy and the cycle repeats. This tendency to roll more up- than down hill in the potential landscape gives the phenomenon the name Sisyphus cooling. Because atoms have a considerable probability to be in an excited state, they will sometimes spontaneously emit photons. This restricts the achievable temperatures to the energy of a single photon (recoil energy). For potassium this is below 1 µK.

The gray molasses combines Sisyphus cooling with velocity-selective coherent population trapping. It mitigates the photon recoil problem by storing cool (slow) atoms in a dark state, that does not couple to the excited states at all. For a simple model system with two non-degenerate ground states and one excited state (lambda system), this can be achieved by driving transitions from both ground states to the excited state. This coherently couples the two ground states and, for equal detunings of the two transition lasers, results in destructive interference of their contributions to the excited state amplitude. In other words, the probability for these atoms to be in the excited states is zero, and no spontaneous emission can occur. However, this is only true for atoms at rest. All others will experience a velocity dependent detuning from the Doppler-shift and scatter light. Atoms end up at low momentum either by the Sisyphus process or just by chance after a photon scattering event and accumulate in the low momentum state because they stop participating in the cooling cycles. An overview of the phenomena described here can be found in [73].

In our experiment, such a situation can be realized by off-resonant coupling of the ground state $^2S_{1/2}$ and the excited state $^2P_{1/2}$ (blue detuned to the 770.1 nm $D1$ line, see Fig. 5.1 a). Because of the more involved level structure of potassium, this does not result in a dark state, but a state with small coupling to the excited state. Consequently, this is called a gray state, giving the technique its name, gray-molasses. During the gray-molasses stage the detuning of the two lasers is ramped in parallel to larger values, to ensure a low scattering rate in the end (despite the

non-zero scattering rate in the gray state). At the end of the stage, the laser that adresses the $F = 1$ ground state is switched off first, such that the atoms are pumped to the $F = 1$ manifold.

With this setup, we achieve temperatures on the order of 7 µK, extracted via time-of-flight measurements. Special care needs to be taken to ensure equal detuning of the two lasers during the whole stage. A detailed description of the frequency generation and locking scheme can be found in [74]. More information regarding the experimental setup can be found in [65]. The generation of the $D1$ laser light has also been switched to a frequency doubled telecom-range fiber laser.

Magnetic Trap

For strong enough magnetic fields, the Zeeman shift of the atomic substates can be sufficient to provide the sole trapping force without any light. To achieve this, the magnetic coils are driven in anti-Helmholtz configuration. Just like for the MOT stages this results in zero magnetic field in the center and large gradients. Magnetic hyperfine states for which the energy increases with magnetic field (so called low-field seekers) can be trapped in this configuration. From the $F = 1$ manifold of the ground state of potassium this is the case only for $|F = 1, m_F = -1\rangle$ (see Fig. 5.1 b). Because the other states are lost from the trap, this results in effective substate cleaning of the sample, and we end up with our experimental substate. The magnetic trap is also used to compress the cloud. Additionally, its center can be shifted during the magnetic trap stage via three pairs of offset coils. This enables efficient loading from the gray molasses to the magnetic trap and from there to the dipole trap.

Details on the design and characteristics of the magnetic coils can be found in [75] and [76]. Control circuits that enable the operation of the coils in Helmholtz and anti-Helmholtz configuration with up to 400 A can be found in [69].

Dipole Traps and Evaporative Cooling

The final steps towards condensation are performed in dipole traps. These are generated by far-off resonant infrared light (1064 nm). Because of the large detuning, scattering rates and heating are much smaller than for the near-resonant light considered before. Via an induced dipole moment, the light beams can still exert forces on the atoms. In case of the red detuned light, these are attractive. More details on the working principle of dipole traps are described in the next section. To generate large trapping forces, a lot of power and large intensity gradients are needed. Up to 12 W can be provided by each of the two beams that are crossed and focused (to a beam waist of ~ 50 µm) in the science cell to form a local intensity maximum to trap the atoms.

This deep crossed-dipole trap can directly load the atoms from the magnetic trap. In the crossed-dipole trap we start the evaporative cooling process. For this, the trap depth is continuously lowered by reducing the power in the beams. Atoms in the tail of the momentum distributions are statistically more likely to escape the trap. Thermalization processes will redistribute the remaining energy with a tendency to-

ward the new equilibrium distribution that corresponds to a lower temperature. To aid in the formation of the BEC, a third smaller beam is added that produces a local dimple in the potential (in the context of this experiment called condensor). While the power of this beam is also ramped down, it is ramped slower than the power of the crossed-dipole trap (reservoir). Just before the big reservoir trap is turned off, a fourth beam is added. This has a tighter focus in gravity direction than in the other directions. This pre-compresses the BEC (and is in the context of this experiment called compressor) to enable an efficient loading of the final two-dimensional trapping configuration. BEC formation occurs during a final evaporation ramp of the condensor and compressor powers. During the whole evaporation process the interatomic interaction is tuned with an external magnetic field. This is important to increase the scattering cross section that is crucial for the thermalization. Additionally, the interaction at zero magnetic field is of attractive nature. For this, the formation of a large BEC would not be stable but lead to a collapse of the cloud [77]. A good visualization of the evaporation process, the power ramps in the individual beams, as well as the technical details of the hardware that enables their precise control can be found in [65]. Since then, the top beam has been removed and some absolute values changed.

The whole sequence from the MOT stages to the production of a BEC takes less than 20 s. This sets the repetition rate of our experiment. MATLAB-written control scripts and user interfaces enable the continuous operation of the experiment. This includes scans through a multi-dimensional parameter space as well as gathering statistics. Actively water-cooled parts are connected to a system of temperature sensors and interlocks that shut off if increased temperatures or errors of the cooling system are detected.

5.3 External Potential

5.3.1 Dipole Forces

After the magnetic trap, all relevant potentials are formed by the dipole force that far detuned lasers exert on neutral atoms. The laser induces a small shift of the electron distribution polarizing the atoms. The polarized atoms, in turn, feel a force from the light field. This can be calculated in perturbation theory. To motivate the arising forces we will first consider a classical picture. For this we imagine the atoms as a two-level system with a single transition frequency. In the simple picture, driving this transition with a laser is equivalent to driving a harmonic oscillator. If the laser is far detuned from atomic resonances, the oscillator is driven far off resonance and does not show a large response. More importantly, however, driving the oscillator below the resonance frequency gives an in-phase response, while driving it above gives an out-of-phase response. As a result, the polarization of the atom is in phase with the light field for red detuned lasers (lower frequency), leading to a reduction in

energy. For blue detuned lasers we get an increased energy instead. Consequently, the atoms are attracted by red detuned light and can be trapped in maxima of the light field. Conversely, they are repelled by blue detuned light and can be trapped in minima of the light field.

The same phenomenon can be found with semiclassical perturbation theory (results taken from [78]). For this, we treat the atom as a two level system. The ground state $|g\rangle$ and the excited state $|e\rangle$ are coupled via the external electric field of the laser E and their electric dipole moment μ

$$\Delta E_{g/e} = \pm \frac{|\langle e| \mu |g\rangle|^2}{\hbar \Delta} |E|^2, \tag{5.1}$$

where the ground state and the excited state are shifted in opposite directions. The detuning $\Delta = \omega - \omega_0$ is given by the energy difference of the corresponding dressed states (including the light field) and is given by the difference of the unperturbed transition $\hbar\omega_0$ and the actual photon energy $\hbar\omega$. The transition matrix element is the same that defines the spontaneous decay rates and the natural linewidth Γ.

$$\Delta E_{g/e} = \pm \frac{3\pi c^2}{2\omega_0^3} \frac{\Gamma}{\Delta} I, \tag{5.2}$$

where I is the intensity of the laser light. While the energy shift goes directly with the overlap between the ground and excited states, the probability to actually scatter one of the photons goes with this quantity squared

$$\Gamma_{\mathrm{sc}} = \frac{3\pi c^2}{2\hbar\omega_0^2} \left(\frac{\Gamma}{\Delta}\right)^2 I. \tag{5.3}$$

For a desired trap depth, a combination of large detunings and high intensities minimizes the heating due to scattering.

In general, potassium atoms cannot be treated as a two-level system because the $D1$ line and the $D2$ line have similar energy. For detunings that are large compared to the hyperfine splitting and for linearly polarized laser light we get the ground state energy shift

$$\Delta E_g = \frac{\pi c^2 \Gamma}{2\omega_0} \left(\frac{2}{\Delta_2} + \frac{1}{\Delta_1}\right) I, \tag{5.4}$$

where Δ_2 denotes the detuning to the $D2$ line and Δ_1 the detuning from the $D1$ line. The factors one and two stem from the relative line strengths [78].

If we now want to generate large trapping forces without excessive heating, we have to combine high intensity gradients with a large detuning. This is what was done for the crossed dipole trap in the last section. For red detuned light, the potential minimum is at the intensity maximum, that is naturally in the center of a laser beam. Trapping in the third dimension along the beam path can be achieved by focusing the laser beam, or by crossing two or more laser beams. In the crossed dipole trap, a combination of the two is employed.

However, as the atoms reside in the region of maximal intensity, large potential depths come with increased scattering rates. This can be mitigated by choosing

a blue detuned, repulsive potential instead. There an intensity minimum has to be constructed in which the atoms are trapped. This is done for our final trap configuration in which the experiments have been performed. The working principle and setup are described in the next section.

5.3.2 The Final Trap Configuration

Confinement in Gravity Direction

To achieve a quasi-two-dimensional condensate, we confine the BEC to a single site of a one-dimensional lattice. This lattice is achieved with an interferometer setup that interferes two blue detuned laser beams (at 532 nm) under a shallow angle in the science cell. A schematic representation is shown in Figure 5.2. The resulting interference pattern forms light sheets with normal vectors in gravity direction (referred to as pancakes) that are spaced by $\sim 5\,\mu$m. Because of the blue detuning, potential minima (lattice sites) will be in the intensity minima of the interference pattern. With enough precompression of the BEC with the attractive compressor beam, the BEC can be loaded into a single lattice site. The lattice power is subsequently increased, tightly confining the BEC in the direction of gravity. Differences in path length of the interferometer arms set the phase of the lattice and with that the position of the lattice sites. Short-term stability is provided passively by a compact interferometer setup mounted on a massive aluminum wedge. This aluminum block is not rigidly connected to the optical table but rests under its own gravity on three contact points. In addition, the temperature of the optic table is passively stabilized by tightly closed curtains around the edge of the table and actively stabilized by a temperature stabilization of the whole lab (with its reference point located on this optic table). Long-term drifts can be compensated with a piezo-crystal driven mirror in one of the interferometer arms. The mirror position is scanned and readjusted multiple times a day to ensure loading of a single pancake.

For the typical lattice power used in the experiments, the trap frequency in gravity direction is $\omega_z = 2\pi \times 1.5\,$kHz. The corresponding energy spacing in z-direction is larger than the interaction energy set by the chemical potential at the interaction strengths and densities used in the experiments in this work (ensuring the quasi-two-dimensionality). This trap frequency was measured by modulating the lattice power at different frequencies. Resonances appear in the form of substantial atom losses from the trap.

To decrease the interaction between the lattice light and the BEC, the atoms are additionally magnetically levitated against gravity. The atoms in the experimental substate have a substantial magnetic moment (see red line in Fig. 5.1 b)). They are low-field seekers at the magnetic fields in the vicinity of the Feshbach resonance (towards the higher end of magnetic field axis). A difference in current in the top and bottom coils that produce the Feshbach field generates a magnetic field gradient to compensate the gravitational force on the atoms.

Details on the lattice design and the trap frequency calibration can be found in [65].

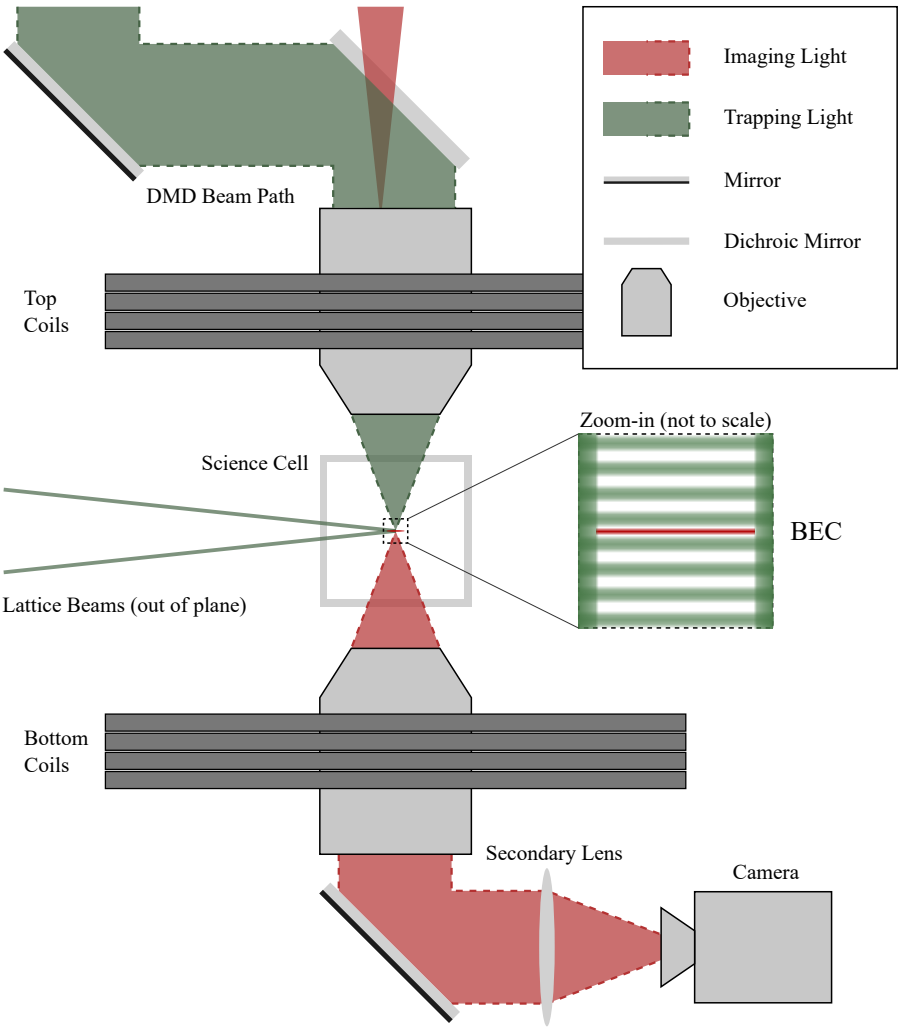

Figure 5.2: Experimental scheme including the final trapping lights (green) and imaging beam path (red). Shaded regions denote the beam paths. Paths with dashed outlines represent the imaging (projection) of a single point while those without dashed outlines represent the beam profile. Note that the focus of the imaging light is slightly off center in the backfocus of the objective. This results in an imaging beam that is angled in the atom plane. The main pair of magnetic field coils is also shown.

Tunable in-Plane Potentials

In addition to the confinement to the two-dimensional plane, there is an adjustable potential in the plane. It can be used to provide a variety of boundary conditions and trap shapes, by shaping the intensity profile of a blue detuned laser. Furthermore, it enables dynamic adjustment of the external potential $V_{\text{ext}}(t, x, y)$ in the region occupied by the BEC. The parameter space available to modern quantum gas experiments has grown tremendously with the potential shaping capabilities that are available through modern light shaping technologies. An overview can be found in [79].

At the heart of our potential shaping setup is a Digital-Micromirror-Device (DMD). These devices are widely used for video projectors or lithography applications. The DMD employed in this setup consists of an array of 2560 by 1600 micrometer sized mirrors (7.6 µm) which can be turned off and on individually. In practice, the two states correspond to a small tilt of the mirrors by $\pm 12°$. Depending on the mirror state, the light is either blocked or projected onto the atoms through a setup of output optics. The DMD then acts as an adjustable intensity mask. The output optics consist of two $4f$ setups that form a real image of the intensity mask in the atom plane, demagnified by a factor of ~ 90.

At this scale a single mirror would be < 90 nm, which is well below the optical resolution limit. We use light at 532 nm and a diffraction limited objective with a numerical aperture of NA = 0.5 as the last lens. This gives a theoretical smallest spot size of

$$\frac{1.22\lambda}{2\text{NA}} = 0.65\,\mu\text{m} \tag{5.5}$$

(Rayleigh criterion). It assumes an ideal diffraction limited point spread function (PSF) in the form of an airy disc and measures the distance from its central peak to the first minimum. We can use the fact that multiple mirrors fall below this spot size to implement an adjustable potential height despite the binary nature of the mirror states. To do this, the desired potential is discretized to the size of the array (2560 by 1600), essentially giving a gray-scale image of the desired potentials. The square root of the image values is taken which ensures the right intensity scaling in the atomic plane after interference of the sub-resolution spots is taken into account. This can be interpreted as ensuring that the following binarization and subsequent convolution with the PSF are happening at the field level and not on the intensity. The square root image is binarized with the Floyd-Steinberg dithering algorithm. This method sweeps through the array, rounds pixel values (mirrors) to either one (on) or zero (off), and forwards the rounding error to neighboring pixels (that have not been rounded yet). The image after the output optics and in the atomic plane then closely resembles the desired potential.

Further optimization of the potentials can be performed using an active feedback algorithm ([66, 80]). It assumes the Thomas-Fermi approximation to be valid and infers the potential from the atomic density distribution 3.10. The differences to the desired potential shape are then iteratively minimized. This algorithm was not used for the homogeneous density distributions used in the scale factor measurements.

Dynamical adjustment of the potential is implemented by switching through a series of images that are stored in the DMDs onboard memory. The time between two switches can be as low as 100 µs and is currently limited by the experimental control system (but close to technical limitations of the DMD). Alternatively, the total potential landscape can be dynamically scaled, by adjusting the intensity of the ingoing laser. We use the dynamic switching in the loading process of the final trap configuration. For the homogeneous density distributions in circular box boundaries, we start with an elongated and off-center trap shape, that closely resembles the form of the cloud in the compressor beam. Then, the trap shape is slowly transformed to the round box of the desired size over the course of 130 different intensity masks. This minimizes a possible sloshing motion of the cloud from the change in trap geometries. Errors in this loading sequence have been found to reduce the prevalence of holes in cloud (consistent with the expected size of vortizes). These capabilities can also be used to produce initial states in density (used in [81]) as well as by imprinting a phase (used in [82] and [83]).

Details on the DMD setup in the experiment can be found in [69]. The design and testing stage is described in [84]. The influence of different boundary shapes and spatial noise on the potential was studied in [85]. In addition to optimization algorithms, reference [66] also includes detailed plans and test setups to enhance local control by employing a second DMD.

5.4 Interaction Strength

To simulate the expansion of space, we need to have an adjustable interaction strength. In this section we motivate the usage of the effective contact potential for the description of the low momentum atomic interactions in our condensate.

We will see that the scattering behavior at the low energy scales boils down to a phase shift of the atomic wave function, that is associated with the scattering length a_s. This is similar to what we have seen for the delta peaks in one-dimensional scattering theory.

Additionally, the phase shift can differ in the energetic vicinity of a molecular bound state of a closed scattering channel. Its presence therefore alters the strength of the interaction. If this bound state and the individual particles in the open channel have a different magnetic moment, a magnetic field can be used to tune the bound state in and out of resonance with the scattering process. This is called a magnetic Feshbach resonance. By applying a magnetic field close to one of those resonances, the interaction can be tuned.

Finally, we show some technical details on the magnetic field calibration and the compensation of magnetic field gradients. The first is important for an accurate control of the interaction constant, while the latter is important to not exert unwanted forces on the cloud.

5.4.1 Scattering Length

A realistic potential between two neutral atoms consists of a Van-der-Waals attraction at short distances and a repulsion due to Pauli exclusion of the electrons at even shorter distances. Figure 5.3 a) shows Lennard-Jones potentials, for which the Van-der-Waals attraction is modeled proportional to $1/r^6$ and the repulsion is proportional to $1/r^{12}$. The precise potential requires solving the full quantum mechanical many body problem, which is infeasible. Even with a model potential, we need to solve the Schrödinger equation for the scattering states $\psi(\mathbf{r})$

$$\left(-\frac{\hbar^2}{2m^*}\nabla^2 + V(r) - E\right)\psi(\mathbf{r}) = 0, \tag{5.6}$$

where $\mathbf{r}$ is the relative position of the atoms, $V(r)$ is the spherically symmetric potential that depends on $r = |\mathbf{r}|$ and goes to zero for large distances, m^* is the reduced mass $m/2$ of the system and E is associated to some positive energy of the state. This condition of positive energy restricts the solutions to unbound states and is simply the kinetic energy in the limit of large distances r and vanishing potential. In this limit, we also know the solutions for the scattering states

$$\psi(\mathbf{r}) = e^{ikx} + f(k,\theta)\frac{e^{ikr}}{r}, \tag{5.7}$$

where the first term is the incoming wavefunction (arbitrary chosen along the x-axis) and the second term describes the scattered wavefunction. This is similar to what we have discussed for the one-dimensional scattering process, where the solutions reduced to plane waves in region I and III with zero potential. Instead of a reflection amplitude b_k, we get a continuous scattering amplitude as a function of angle θ between the incoming and reflected direction. This can be calculated for the potential $V(r)$ via a decomposition of the wavefunctions into spherical harmonics and radial wavefunctions χ_{kl} [63].

At the extremely low temperatures we are working at only the solutions with zero angular momentum χ_{k0} contribute to the scattering amplitude (s-wave scattering) and one finds

$$f(k,\theta) \to f(k) = \frac{e^{i2\delta_0} - 1}{2ik}. \tag{5.8}$$

The influence of the potential at large distances only appears as a phase shift δ_0, even though the full solution of the wavefunction might oscillate very fast for small distances where the potential is substantial (and $|V(r)| \gg E$).

For low momenta this phase shift can be found by setting $E = 0$ in Eq. 5.6 and matching the solutions to the solutions for large distance [61]. One finds, that the phase shift is proportional to k

$$\delta_0 = -a_s k, \tag{5.9}$$

with the scattering length a_s.

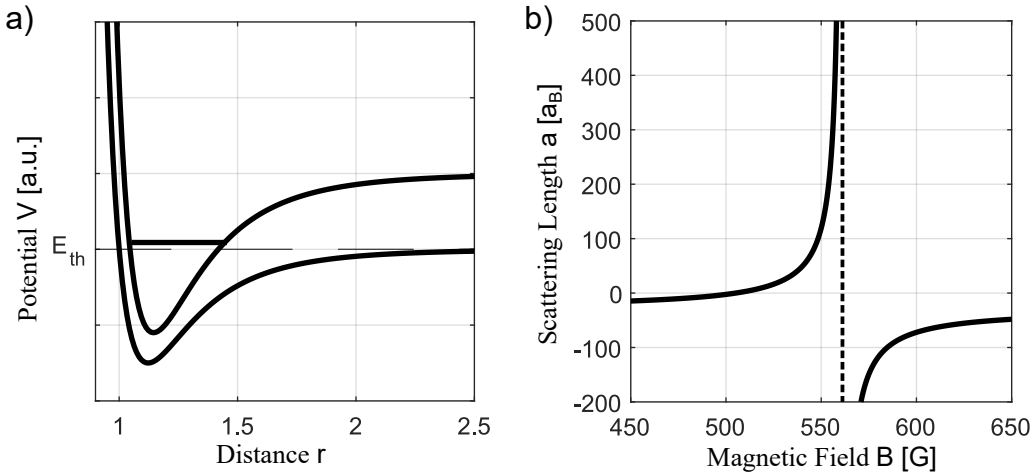

Figure 5.3: Schematics of a Feshbach resonance. a) An interatomic potential (represented by a Lennard-Jones potential) with asymptotic energy at large distances E_{th} describes the scattering of two particles with a given internal state (open channel). A second potential that represents a different internal state of the particles has a bound state in the energetic vicinity of E_{th}, but a much higher asymptotic energy. In this case, the two scattering particles do not have the kinetic energy needed to exit the collision in the other internal state (closed channel). Their scattering length can still be influenced by the existence of the bound state. If the magnetic moment of the internal states differs, the energy difference to the bound state can be tuned via an external magnetic field. This is called a magnetic Feshbach resonance. b) Scattering length as a function of the external magnetic field in the vicinity of the Feshbach resonance for the experimental substate ($|F = 1, m_{\mathrm{F}} = -1\rangle$ at low fields). The dashed vertical line marks the position of the resonance at 561.14(2) G. Values to generate this graph have been taken from [86].

The same phase shift can be obtained by replacing the potential with a δ-peak like we did for Equation 3.3. For a positive scattering length, the interaction energy increases with the density, and for a negative scattering length, it decreases. Positive scattering lengths can be associated with a repulsive character of the interaction (positive δ-peak), and negative scattering lengths can be associated with an attractive character (negative δ-peak). However, this is only accurate for low momenta and is useful only after the scattering length is known, either from an experiment or calculations involving the actual potential. Note that the low momentum regime discussed here is not the same as for the acoustic approximation and will always be a valid assumption.

5.4.2 Feshbach Resonances

The scattering behavior changes in the energetic vicinity of molecular bound states. Figure 5.3 a) shows two interatomic potentials. The lower one corresponds to the potential discussed earlier. A particle coming from positive infinity carries at least the energy associated with the asymptotic behavior of the potential E_{th}, which means it is a free particle. Just as before its scattering state has a non-zero amplitude at infinity and it will accumulate a phase shift. This is what we call an open channel. In contrast, the second potential represents the interatomic potential for some other internal state of the atoms. In general, a scattering process can mix these different channels. In the example in Figure 5.3 a), the kinetic energy of the incoming particles is not high enough to exit the collision in the new internal state of higher energy. This is called a closed channel. If the energy difference to a bound state of a close channel is small, it can alter the scattering behavior nonetheless. This can be imagined as a higher order process in which the atoms form a short lived bound state that contributes to the energy and phase accumulation in the process.

The energy shift can be calculated via second order perturbation theory [63] and, therefore, is proportional to $1/(E_{\mathrm{th}} - E_{\mathrm{res}})$. E_{th} is the threshold energy to get an unbound state in the lower energy open channel and E_{res} is the energy of the molecular bound state. If the internal states of the scatterers in the open channel and the molecular bound state have a different magnetic moment, the energy difference in the denominator can be tuned via an external magnetic field. This can be the case for different spin states in the two channels.

The scattering length can then be approximated by

$$a_s(B) = a_{\mathrm{bg}} \left(1 - \frac{\Delta B}{B - B_0}\right), \tag{5.10}$$

where B_0 is the the magnetic field where $E_{\mathrm{th}} - E_{\mathrm{th}} = 0$, a_{bg} is the unperturbed scattering length and ΔB characterizes the width of the resonance. The latter depends on the difference of the magnetic moments of the states, but also on the overlap between the unperturbed scattering state and the resonant bound state that is generated by the perturbation. This coupling of the channels, as well as the energy of the bound states, depend on the precise shape of the potentials. Therefore, it is hard to predict the exact positions and width of Feshbach resonances. Measurements of Feshbach resonances can in turn give insight into the potentials.

Figure 5.3 b) shows the dependence of the scattering length on the magnetic field in the vicinity of the Feshbach resonance used in the experiments in this work. The open channel has both atoms in the $|F = 1, m_F = -1\rangle$ state of the ground state manifold and a Feshbach resonance at $561.14(2)\,\mathrm{G}$ with a width of $-56.2(2)\,\mathrm{G}$ and a background scattering length of $-29.5(4)\,a_B$. These values have been taken from reference [86]. Multiple other Feshbach resonances are available for potassium ^{39}K, including ones for different substates or scattering processes between different substates.

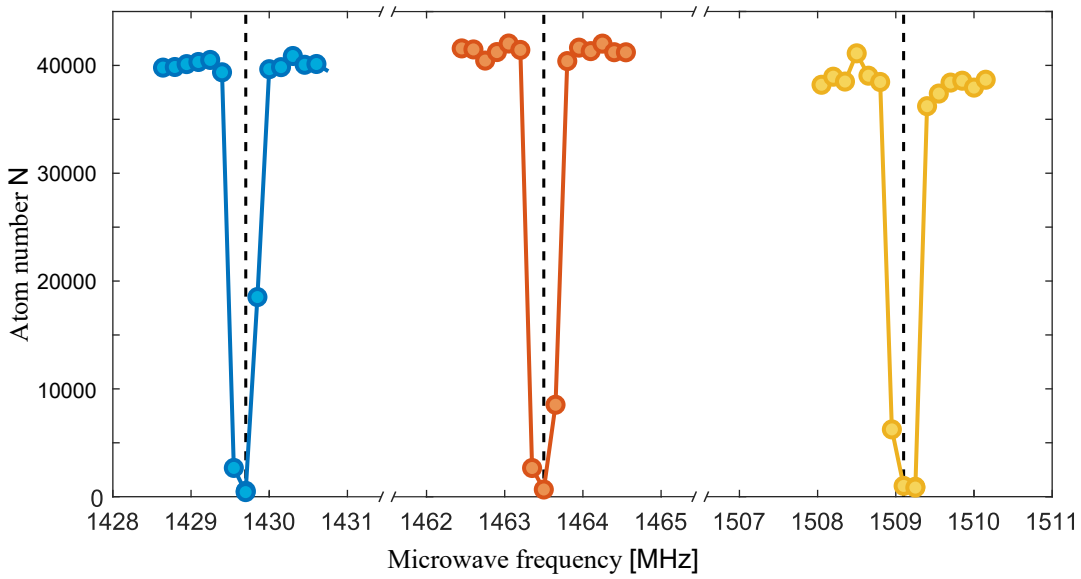

Figure 5.4: Measurement of the microwave transitions between different ground state sub-levels used for the calibration of the magnetic field. Measurements where taken for 527.62 G (blue, corresponding to $20\,a_{\mathrm{B}}$), 540.27 G (orange, corresponding to $50\,a_{\mathrm{B}}$), and 557.28 G (yellow, corresponding to $400\,a_{\mathrm{B}}$) set in the experiment. Expected values for the transition from theory are marked with dashed lines.

5.4.3 Calibration of the Magnetic Field

Especially because of the divergent nature of the Feshbach resonance, the tuning of the interaction strength depends on the accuracy of the magnetic field. To ensure this, we perform measurements of the magnetic field multiple times a day. Typically, no drifts are detected on this timescale.

The energy shift of the Zeeman sub-levels is very sensitive to the external magnetic field as can be seen in Figure 5.1. We calibrate the magnetic field at a microwave transition from the experimental substate (red), to another ground state with a different magnetic moment for different values of the magnetic field that correspond to $20\,a_{\mathrm{B}}$, $50\,a_{\mathrm{B}}$, and $400\,a_{\mathrm{B}}$, (marked in colors). By scanning the frequency of the microwave, we can identify the resonance at the frequency where the number of atoms in the experimental substate becomes minimum. From comparison to theoretical values for the transition frequency we can infer the actual magnetic field and recalibrate the experiment.

An example for such a measurement is shown in Figure 5.4. The theoretical values for the transition are marked as dashed vertical lines. For the experiments shown in this work, no calibration measurement was taken that is consistent with a shift larger than 0.5 MHz. The resonance frequencies in this magnetic field range change by 2.7 MHz/G, which puts the bound on the magnetic field error below 0.2 G. This gives an upper limit to the relative error of the scattering length of 3% for the measurement of the coherent oscillations at $200\,a_{\mathrm{B}}$, which is the experiment that is most sensitive to an offset in the magnetic field. During such a measurement, the microwave is

turned on for 100 ms and at relatively high power. Therefore, the complete loss of the atom signal at resonance cannot be attributed to a coherent transfer to the other state that is not sensitive to the imaging transition (π-pulse). Instead, the signal loss at resonance can mainly be attributed to atoms being lost from the trap. This is because the magnetic moment of the state coupled by the microwave is opposite to the original state. Instead of being levitated by the magnetic field gradient, it effectively experiences twice the acceleration from gravity. While the process could be optimized for a higher level of precision of the resonance extraction, this also puts a limit on the short-term fluctuations of the magnetic field (within the $100ms$).

5.4.4 Compensation of Magnetic Field Gradients

To compensate for magnetic field gradients generated by the main coils, two wires close to the glass cells are used to generate a counteracting magnetic field gradient. The compensation is optimized with respect to the center of mass of the atom distribution in a large trap for different values of the magnetic field. With the calibrated values for the offset and a slope of the gradient relative to the magnetic field value, the center of mass does not move for changes in the magnetic field. This is important to avoid a sloshing of the cloud when driving ramps in the magnetic field. Because the compensating field also contributes to the overall magnetic field, a calibration of the field of the magnetic field is required after large adjustments of the magnetic field gradients.

5.5 Density Readout via Absorption Imaging

We extract the density distribution via absorption imaging of the cloud at the high magnetic fields in the vicinity of the Feshbach resonance. In this section, we first give some important details on the imaging process in this regime and the technical capabilities of the setup. Then we discuss in-depth how the capabilities of our imaging system influence the extracted data quantitatively and how we can compensate for this. We will see that imaging aberrations and other distortions result in a length-scale-dependent imaging sensitivity. It is important to compensate for this in extracted data to get accurate results.

5.5.1 Working Principle

In absorption imaging, light is shone in on resonance with the $D2$-transition, taking into account the energy shift from the magnetic field (see Fig 5.1). Some of the light is scattered by the atoms and the BEC is destroyed in the process. Light that is not scattered (or scattered in the opening angle of the objective) is imaged via a diffraction limited objective, a slow secondary lens and a CCD camera (details of the setup in next section). The comparison to a second image (reference picture) that is taken shortly after (and without atoms) allows us to extract the light intensity that is scattered by the atoms in a spatially resolved manner and from this extract the density distribution. We assume a two-level system with the effective saturation Intensity $I_{\text{sat}}^{\text{eff}}$ and effective light scattering cross section σ_{eff} [87]. The two-dimensional density is then extracted from the intensity distributions of the atom image $I_f(\mathbf{x})$ and the reference image $I_i(\mathbf{x})$ via

$$n(\mathbf{x}) = \frac{1}{\sigma_{\text{eff}}} \left[\ln\left(\frac{I_i(\mathbf{x})}{I_f(\mathbf{x})}\right) + \frac{I_i(\mathbf{x}) - I_f(\mathbf{x})}{I_{\text{sat}}^{\text{eff}}} \right] \tag{5.11}$$

If we interpret the intensity on the reference $I_i(\mathbf{x})$ as the intensity of the light before entering the cloud and the intensity on the atom image $I_f(\mathbf{x})$ as the intensity after passing through the cloud, we get an interpretation of the two terms in the square brackets. The term involving the natural logarithm is dominating in the low intensity regime, where the intensity is exponentially depleting as the light passes through the cloud according to the likelihood of classical scattering (Lambert-Beer law). The second term captures the quantum effect of saturating the transition. At high intensities the system approaches 50% likelihood to be in the excited state and one finds a constant scattering rate $\Gamma/2$ per atom, independent of the intensity, where Γ is the spontaneus decay rate of the excited state. This constant rate shows up as the difference between the intensities $I_i(\mathbf{x}) - I_f(\mathbf{x})$. The saturation intensity the transition that sets the relevant scale between those two extremes can be calculated from the resonant wavelength and spontaneous decay rate. However, the effective value absorbs uncertainties from the calibration of the absolute intensity distribution in the atom plane, imperfect polarization of the imaging light, and the more complex picture of the real multi-level system. It was determined experimentally by measuring identically prepared density distributions at various imaging intensities [87]. The proper value for $I_{\text{sat}}^{\text{eff}}$ makes the extracted densities independent of the intensity they were measured at. Similarly, σ_{eff} normalizes the result to actual atom numbers. This value has been inferred by matching density profiles at different interaction strengths and trapping potential with GPE-simulations [69]. The extracted densities are consistent with measurements of the speed of sound at known interaction strengths. Nevertheless, we replace the density by these quantities for the extraction of the spectra (see 4.32).

Reference Picture Optimization

The coherent nature of our imaging light allows for the formation of interference fringes, for example from diffraction by dust particles in the imaging path. In addition, these interference fringes can vary slightly from image to image. This is due to small fluctuations of the imaging system caused for example by vibrations, air currents, or temperature drifts. Such effects occur on various timescales, sometimes between taking an atom image and the corresponding reference. We use an algorithm (adapted from [88]) that optimizes the reference picture to better represent the light distribution on the atom picture and to reduce the statistical fluctuation (photon shot noise) of the reference images. For this optimization a set of 200 reference images that were taken closest in time to the atom picture is used, from which we construct a new reference image as a linear combination of all reference images in the set

$$I_i^{\mathrm{opt}} = \sum_{j=1}^{200} c_j I_i^j, \tag{5.12}$$

where $I_i^j(\mathbf{x})$ denotes the j^{th} reference image in the set and c_j its weight in the linear combination. These weights are chosen such that the least square difference C between the optimized reference image and the atom image is minimized in a region that we assume to be free of any atom signal

$$C = \sum_{\mathrm{px}} m \left(I_f - I_i^{\mathrm{opt}}\right)^2, \tag{5.13}$$

where $m(\mathbf{x})$ is a mask function that is equal to a band of 100 pixels (px) in width around a chosen region of interest. This algorithm can reduce the total noise in two ways. First, if there is a significant change in the light distribution between atom image and reference image, it can identify other reference images with a similar light distribution and assign them large weights. This way, the optimized reference image captures the change in light distribution. Second, if there are multiple reference images with a matching light distribution, the least square difference is minimized by equal weights for those images. This essentially reduces the photon shot noise of the reference image by averaging multiple images. In practice it will be some trade-off between the two effects. Most of the time, we find nonzero weights for a large number of images, suggesting that the averaging effect is important.

For the measurements shown, the region of interest comprises the 300 central pixels, which is slightly larger than the 200 by 200 pixels shown for the density profiles in this work. Therefore, the optimization region defined by the mask m is well outside the trapping potential of the DMD. This does not ensure that there are no atoms in this region, but any atom signal in this area should not be correlated to signal in the trap and can only lead to a worse performance of the algorithm.

We employ an imaging transition of the $D2$-line that is a closed cycle in the high magnetic field range ($|m_\mathrm{J} = -1/2, m_\mathrm{I} = -1/2\rangle_g \rightarrow |m_\mathrm{J} = -3/2, m_\mathrm{I} = -1/2\rangle_e$). In this magnetic field range, the energy eigenstates of the Zeeman sub-levels of the ground state manifold are not perfectly eigenstates of the $|m_\mathrm{J}, m_\mathrm{I}\rangle_g$ basis, but have small admixtures of another state. As a consequence, the excited state of the imaging transition can spontaneously decay in the other ground state (the one with the opposite admixture). For our system and magnetic fields, the probability for this decay is on the order of 2%. If the transition is saturated, this corresponds to a loss of 50% of the atoms to the other ground state within $\sim 2\,\mu\mathrm{s}$. Therefore, we employ a second imaging laser driving a symmetric transition to an excited state that has spontaneous decay to the original ground state. Because the decay rates are equal, we employ both lights at the same power. In this way, the signal can be collected for longer imaging times. For all measurements in this work the imaging time was set to $5\,\mu\mathrm{s}$. The large frequency differences to the low field $D2$-line are generated with two separate lasers that are locked to the $D2$ reference laser via an offset-locking scheme. The two-frequency imaging scheme and the extraction of atom densities in the intermediate intensity regime have been published in [87]. More details can be found in [69]. The offset-locking scheme is described in [89].

5.5.2 Imaging Setup

A scheme of the imaging setup is shown in Figure 5.2. The imaging light is combined with the DMD light for the trapping potential via a dichroic mirror, before both enter the top objective. This objective is needed to create the precise intensity distributions for the potential. For imaging, the light beam should be collimated. Therefore, the objective is compensated with a setup containing two lenses that focus the beam in the backfocal plane of the objective. This point of focus is slightly off-center from the center of the objective. This results in a slight tilt of the imaging beam when it passes through the atom plane. The reason for this is two-fold. It avoids interference fringes from multiple reflections at the glass-air transitions of the glass cell that are not anti-reflection coated. Additionally, the imaging light does not have to be overlapped with the MOT beam that also passes through the objective. This would be more involved, because both the imaging light and the MOT light each consist of two frequencies with orthogonal polarizations. We will see later in this chapter, that the tilted imaging beam negatively impacts the image quality. As a consequence of these findings, the imaging system was recently upgraded.

After interaction with the atoms, light is collected by the lower objective. It is identical to the top objective and is specified to be diffraction limited for 767 nm light (imaging light) and 532 nm light (trapping light) with a numerical aperture of NA= 0.5. At 767 nm this corresponds to a resolution of $\sim 1\,\mu\mathrm{m}$ (see Eq. 5.5). The objective is infinity corrected, which means it produces a Fourier image in its backfocal plane. This is subsequently refocused with a 1000 mm lens onto the camera sensor that takes images with a resolution of 1024×1024 pixels. The overall magnification of the system has been calibrated with a Bragg pulse. For this a standing wave of light of a well-known wavelength λ is created via back-reflection

off a mirror. This transfers some fraction of the atoms in the momentum modes $k = \pm 4\pi/\lambda$. A time of flight measurement enables the calibration of absolute scales in the image. This resulted in an equivalent pixel size in the atom plane of 0.455 µm/px. Comparison to the actual pixel size results in a magnification factor of 35.

The calibration measurement, details on the generation of imaging lights, and details on the general setup can be found in [69]. Measurements and numerical simulations regarding the imaging setup and properties of the CCD camera can be found in [90].

5.5.3 Experimental Extraction of the Imaging Sensitivity

Ideally, a diffraction limited imaging system would have a sharp cutoff in momentum space that is set by the opening angle or numerical aperture (NA) of the objective (which is usually the limiting component). This sharp cutoff corresponds to an airy function in real space. This is what a sub-resolution sized point source will look like after such an imaging system. In practice, a multitude of abberations that diminish the quality of the imaging system also alter this shape. This point-spread function (PSF) and its Fourier space counterpart are not only a good indicator for imaging quality but can also be used to calibrate the imaging sensitivity at different length scales. In this section, the quality of the imaging system is quantized by measuring the PSF in order to enable this kind of correction of the results.

To measure the imaging sensitivity we adapted a method by Hung et al. [43, 91]. First, we drive a large BEC multiple times close to the Feshbach resonance. This results in large atom losses and a thin cloud with densities ten or more times smaller than the usual distributions. Then we wait for 100 ms before taking an image of the cloud. We expect this to be reasonably thermalized at some temperature that is above the critical temperature (for BEC formation) at these low densities. A simple comparison of the thermal wavelength with the interparticle distance, $\lambda_{\mathrm{DB}} < 1/\sqrt{n}$, gives an estimate for this critical temperature of about 75 nK, above which we need to be.

In the limit of high temperatures the atoms behave as randomly distributed independent scatterers. For the images we expect this white noise distribution convoluted with the point-spread function

$$n^{\mathrm{exp}}(\mathbf{x}) = n_{\mathrm{wn}}(x) * P(\mathbf{x}). \tag{5.14}$$

We construct a simple density contrast to the mean

$$\Delta n^{\mathrm{exp}}(\mathbf{x}) = n^{\mathrm{exp}}(\mathbf{x}) - \langle n^{\mathrm{exp}}(\mathbf{x}) \rangle, \tag{5.15}$$

where the brackets denote the mean over many realizations. For white noise, this is expected to be flat. Because there is no interference with a background condensate, this is sufficient. We can calculate the density noise power spectrum by taking the

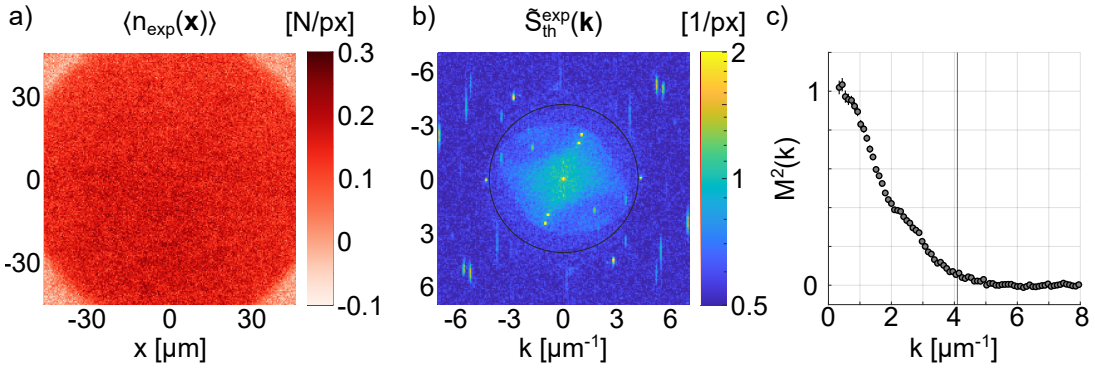

Figure 5.5: Mean density distribution over more than 200 realizations of a thin thermal cloud (a), extracted two-dimensional spectra that hold information of the two-dimensional imaging response (b) and the extracted imaging response $M^2(k)$ (c). The solid black lines in b) and c) show the theoretical resolution limit. The errors in c) show 1σ standard errors of the mean from the statistical fluctuations of the imaging response.

absolute square of the Fourier transform of the density contrast.

$$\begin{aligned} S_{\mathrm{th}}^{\mathrm{exp}}(\mathbf{k}) &= \frac{1}{N}\left\langle \left(\int \frac{\mathrm{d}^2\mathbf{k}}{2\pi} \Delta n^{\mathrm{exp}}(\mathbf{x}) \right)^2 \right\rangle \\ &= \frac{1}{N}\left\langle \left[\mathcal{FT}\left(\Delta n_{\mathrm{wn}}(\mathbf{x})\right)\right]^2 \left[\mathcal{FT}(P(\mathbf{x}))\right]^2 \right\rangle, \end{aligned} \tag{5.16}$$

where N denotes the mean total atom number. This is a quantity comparable to the spectrum from the last chapter if we take the radial average $S_{\mathrm{th}}^{\mathrm{exp}}(k) = \int_\varphi S_{\mathrm{th}}^{\mathrm{exp}}(\mathbf{k})$. In Fourier space, the thermal spectrum $S_{\mathrm{th}}(\mathbf{k})$ and the imaging abberations separate into a multiplication of their Fourier transformations denoted by $\mathcal{FT}$. We assume that the point spread function does not change over the course of a measurement run. Over many realizations, the white noise means to the (theoretical) thermal spectrum

$$S_{\mathrm{th}}(\mathbf{k}) = \frac{1}{N}\left\langle \mathcal{FT}\left(\Delta n_{\mathrm{wn}}(\mathbf{x})\right)^2 \right\rangle = 1. \tag{5.17}$$

This is the noise floor of uncorrelated particles, equivalent to the noise floor 1/2 we found for the spectra (Eq. 2.28). The difference is the result of a chosen normalization. With this, the momentum dependence of the experimentally extracted spectra is a measure of the imaging response function $M^2(k)$

$$S_{\mathrm{th}}^{\mathrm{exp}}(k) = \int_\varphi \mathcal{FT}(P(\mathbf{x}))^2 \equiv M^2(k), \tag{5.18}$$

a measure of the imaging sensitivity in Fourier space.

Figure 5.5 a) shows the density distribution of a thermal cloud averaged over more than 200 realizations. The spectrum $\tilde{S}_{\mathrm{th}}^{\mathrm{exp}}(\mathbf{k})$ in Figure 5.5 b) corresponds to the one in Equation 5.16 and is normalized to its value in a center region between 3px and

10px ($k \in [0.2\,\mu\text{m}^{-1}, 0.7\,\mu\text{m}^{-1}]$). The black circle marks the theoretical resolution limit in Fourier space. To extract $M^2(k)$, which is shown in Figure 5.5 c), we mask the effect of imaging fringes in b) (an example of this can be found in Appendix A). These fringes show up either as a pair of dots or in the form of stripes. Then, the spectrum in b) is averaged radially. A region well outside the resolution limit (black line) is used to infer a noise background ($k > 6.5\,\mu\text{m}^{-1}$). This is subtracted and the result divided by one minus the background, which normalizes $M^2(k)$ to one in the center (maximal sensitivity) and zero at high k (no signal).

The elongated fringes in b) are probably caused by the movement of the stripes between individual realizations and over the course of a measurement. This is indicated by the dots showing low statistical fluctuations and the stripes showing large statistical fluctuations when compared with the atom signal. In both cases, they do not scale with the atomic signal. The very low momentum regime also shows an enhancement. This is probably not an indication for a temperature below T_c, but is caused by atom number fluctuations larger than statistically expected, which is probably a result of the preparation of the cloud. Both of these features saturate the color scale in b) for some pixels. The errors in c) show 1σ standard errors from the statistical fluctuations of the measured spectra.

We find something that looks like an asymmetric cutoff that does not reach the theoretical limit towards the top-right (bottom-left). This is caused by the tilted imaging beam. Because of this, the objective acts as an asymmetric cut-off in momentum space. For some $\mathbf{k}$, its counterpart $-\mathbf{k}$ is blocked. Fourier transformation of the real-valued images symmetrizes the result. Therefore, the cut-off takes the form of the overlap of two off-center circles the size of the theoretical cut-off. This also explains the signal found beyond the theoretical cut-off (best visible in c)), as the extended region where one of the momenta $\mathbf{k}$ propagates through the imaging system while its counterpart is blocked. Data from high density clouds that better illustrate this phenomenon can be found in Appendix A. We can also see some substructure of the spectra resulting from imaging aberrations. While this shifted cut-off gives some super-resolution properties, it comes at the cost of most of the signal in those regions. The tilt of the imaging beam and with it the asymmetric cutoff were minimized during the writing stage of this thesis. The MOT beam was rebuilt to overlap the axis of the objective via a moving mirror during the MOT stage. A similar design is used for the bottom MOT beam. The new (and old) designs are described in [66].

For low temperatures, the spectrum of a bosonic gas is not necessarily flat, even in the absence of a BEC. Boson bunching in real space can enhance the spectrum at low momenta (up to a factor two for low temperatures). This decays to one as a function of momentum on the order $1/\lambda_{\text{DB}}$. By normalizing the spectrum to its value at zero, we could therefore underestimate our sensitivity by up to a factor two. A normalization of the spectrum using the extracted atom number instead of the normalization to one in the center differs by a factor of 1.17, suggesting $S_{\text{th}}(0) = 1.17$. This would not equate to an underestimation of 15% at high momenta (but less), because this thermal spectrum would not drop to one within our resolution limit. The normalization to the atom number was not used for an approximation of the

temperature and a full thermal spectrum, because we do not have an independent way to verify the accuracy of the atom number extraction at these low densities. Instead, we stick to the assumption $S_{\mathrm{th}}(k) = 1$ for all k.

In the experiment, multiple effects add to the imaging distortions that are captured in the imaging response $M^2(k)$. The pixel size of the camera can have an effect similar to the PSF. In our case, the equivalent size of a pixel in the focal plane of the objective is smaller than the PSF. In Figure 5.5 b) this translates into the spectrum being well within the frame. Furthermore, the atoms move during the illumination time of 5 µs. Accelerated by the imaging lasers, they move out of (or through) the focal plane of the objective. In addition, their spontaneous emission results in a random walk in velocity space and consequently movement in the plane [90]. A detuning of the imaging lasers can also have an impact on the shape of the imaging response. Because the imaging lasers have to be to be adjusted to the Zeeman shift whenever the magnetic field changes, this could differ for measurements at different scattering lengths. Therefore, we measure the imaging response function at all interaction strengths used in the measurements. Although we did not find a significant difference between these, we found differences for measurements taken months apart. To minimize the effect of long term drifts, we interleave the thermal cloud measurements with our experiments.

Correction of Extracted Spectra

Here, we show how the extracted imaging response function $M^2(k)$ can be used to correct the experimentally extracted spectra.
In the experiment we always measure density distributions. The experimentally measured distribution will be the real distribution convoluted with the point-spread function of the imaging system:

$$n^{\mathrm{exp}}(\mathbf{x}) = n(\mathbf{x}) * P(\mathbf{x}) \tag{5.19}$$

As we have seen in section 4.3, experimentally extractable density-density correlations $G_{\mathrm{nn}}(\mathbf{x}, \mathbf{x}')$ are related to the $G_{\pi\pi}(\mathbf{x}, \mathbf{x}')$. The measured correlations are also influenced by the PSF

$$G_{\mathrm{nn}}^{\mathrm{exp}}(\mathbf{x}, \mathbf{x}') = G_{\mathrm{nn}}(\mathbf{x}, \mathbf{x}') * P(\mathbf{x}) * P(\mathbf{x}') \tag{5.20}$$

Because of homogeneity, this will not depend on absolute position but only on $\Delta\mathbf{x} = \mathbf{x} - \mathbf{x}'$. This we can transform to distance $L \equiv |\Delta\mathbf{x}|$ and angle φ. Theoretically, the system is expected to be isotropic such that $G_{\mathrm{nn}}(L, \varphi) = G_{\mathrm{nn}}(L)$. However, this is not true for the experimentally extracted quantities that suffer from the anisotropic imaging response (as seen in Fig. 5.5)

$$\begin{aligned} S_k^{\mathrm{exp}} \sim \int_\varphi \mathcal{FT}(G_{\mathrm{nn}}^{\mathrm{exp}}(L, \varphi)) &= \int_\varphi \mathcal{FT}(G_{\mathrm{nn}}(L, \varphi)) \left[\mathcal{FT}(P(L, \varphi))\right]^2 \\ &= \mathcal{HT}(G_{\mathrm{nn}}(L)) \int_\varphi \left[\mathcal{FT}(P(L, \varphi))\right]^2 \\ &= \mathcal{HT}(G_{\mathrm{nn}}(L)) M^2(k), \end{aligned} \tag{5.21}$$

where we used the isotropy of the unperturbed correlation function and the fact that the Fourier-transformation retains this symmetry (enabling us to split the integral). Additionally, we introduced the Hankel-transform of zero order

$$\mathcal{HT}(f(r)) = 2\pi \int_0^\infty f(r) J_0(kr) r \mathrm{d}r \tag{5.22}$$

with J_0 the zero order Bessel-function of the first kind. Finally, we used

$$\int_\varphi \mathcal{FT}(f(r,\varphi)) = \mathcal{HT}\left(\int_\varphi f(r,\varphi)\right), \tag{5.23}$$

which means Fourier transforming and then averaging over all angles in reciprocal space is the same as averaging over all angles in real space and then Hankel transforming (for details see appendix A.1). This is an important identity. It enables us to extract the experimental spectra from radially averaged density correlations $G_{\mathrm{nn}}^{\mathrm{exp}}(L)$ even though the two-dimensional experimentally measured density correlation is not isotropic. Therefore, we can avoid calculating the full four-dimensional density correlation function $G_{\mathrm{nn}}^{\mathrm{exp}}(\mathbf{x},\mathbf{x}')$ or even the two dimensional correlations $G_{\mathrm{nn}}^{\mathrm{exp}}(L,\varphi)$ at any point and instead only calculate correlations as a function of distance L (for details on this algorithm, see [65]). Finally, we compensate the anisotropic imaging response from the thus obtained spectra

$$S_k = \frac{S_k^{\mathrm{exp}}}{M^2(k)}, \tag{5.24}$$

where S_k is the spectrum as would be obtained from the unperturbed density correlations $G_{\mathrm{nn}}(L)$ (compare Eq. 5.21). In practice we extract $M^2(k)$ like described above and interpolate its values and errors to the momenta used for the extraction of the spectra. This calibration is crucial for a quantitative analysis of the experimentally extracted spectra. Especially, the level of vacuum fluctuations could not be identified without this.

6
Experimental Results

In this chapter we show the results of simulations of a spatially flat FLRW-metric with time-dependent scale factors in the quasi-two-dimensional BEC experiment. We investigate three different scenarios for the time dependence, starting with a linear expansion. This is the prototypical expansion scenario that we used as an example in chapter 2 and that corresponds to a box potential in the scattering framework. This measurement is shown for two different expansion times $\Delta t = 3\,\mathrm{ms}$ and $\Delta t = 1.5\,\mathrm{ms}$. In addition, we compare two periodic scenarios that correspond to periodic potentials. One is a sinusoidal variation of the scale factor, and the other a cusped shape with a jump in the first derivative. These correspond to a potential that is dominated by a single frequency and one that consists of sharp peaks with large contributions of higher harmonics. For this, we measure a significant signal of squeezing below the level of vacuum fluctuations. Some of the results shown here have been published before in [92].

We start the experiments with a flat density distribution of $N \approx 40000$ atoms in a circular box trap produced with the DMD and at some constant scale factor a and scattering length a_s (region I). To ensure a thermal initial state in the quasi-particle occupations, the scale factor is held constant for a hundred milliseconds. Afterwards the scale factor is changed dynamically (region II) in an almost freely programmable manner via a magnetic Feshbach resonance that enables us to adjust the scattering length with external magnetic fields. To prevent motion of the background condensate arising at the potential walls, we adjust the DMD power proportionally to the chemical potential $V_{\mathrm{ext}}(t) \propto \mu(t) = mc_s^2(t)$. Finally, we again keep the scale factor constant for a hold time t_h (region III) before reading out the density distribution via absorption imaging.

We start with a quick overview of the core theoretical concepts that are laid out in detail in the previous chapters. The change in scale factor $a(t) = 1/c_s(t)$ is implemented by a change in the speed of sound c_s (not a change of the physical

size of the BEC). The resulting particle production is interpreted in the scattering framework, where the time dependence of the scale factor turns into a scattering potential in conformal time η

$$V(\eta) = \frac{1}{4}\,\dot{a}^2(t(\eta)) + \frac{1}{2}\,\ddot{a}(t(\eta))\,a(t(\eta)), \tag{6.1}$$

(or its dispersion including counterpart in Equation (4.25)). The time dependence of the mode functions is encoded in the scattering states. The original (vacuum) state in region I sets the boundary condition and corresponds to the transmitted state $\psi_k^{\mathrm{trans(I)}} = c_k e^{-i\omega_k^{\mathrm{I}} t}$, where ω_k^{I} is set by the Bogoliubov dispersion in region I. In region III we get the incoming $\psi_k^{\mathrm{inc(III)}} = a_k e^{-i\omega_k^{\mathrm{III}} t}$ and reflected wavefunctions $\psi_k^{\mathrm{ref(III)}} = b_k e^{-i\omega_k^{\mathrm{III}} t}$. The production of particles as a result of the mixing of positive and negative frequency solutions by the expansion turns into the reflection at the potential. The interference between incoming and reflected wavefunctions gives the density-fluctuation power spectrum

$$S_k(\eta) = \frac{|\psi_k^{\mathrm{III}}(\eta)|^2}{2|c_k|^2} = \frac{1}{2} + N_k + \Delta N_k(t), \tag{6.2}$$

with the particle number $N_k = |b_k|^2/|c_k|^2$ and the coherent oscillations from the interference term

$$\Delta N_k(t) = \frac{|a_k b_k|}{|c_k|^2} \cos\left(2\omega_k^{\mathrm{III}} t_h + \vartheta_k\right). \tag{6.3}$$

By adjusting the hold time t_h in region III (before taking an image), multiple phases of the oscillation are measured.

6.1 Extraction of the Scale Factor

The scattering length a_s can be tuned via the magnetic Feshbach resonance and is expected to be accurate as long as the magnetic field calibration is ensured (see section 5.4.3). In addition, the scale factor depends on other experimental factors such as the density and the trapping frequency in gravity direction. Therefore, we measure the speed of sound for every expansion scenario and interleaved with the actual measurement. In the example shown in Figure 6.1, this is done after performing the linear expansion (with $\Delta t = 3\,\mathrm{ms}$) to ensure comparable densities and magnetic field conditions. The sound speed is measured by injecting a wave packet and extracting its speed. To do this, we project a small repelling spot in the center of the condensate in addition to the box potential, which produces a density dip. When expansion stops at $t_h = 0$, this spot is turned off, and the dip turns into a radially moving wave packet. This measurement is repeated for different hold times and enough statistics to clearly distinguish the deterministic density dip from the random fluctuations. Figure 6.1 shows the results of such a measurement. Mean profiles over ~ 35 realizations (per hold time) are shown (a), in which the moving dip is clearly visible. In addition, we find a second dip moving inwards from the edges,

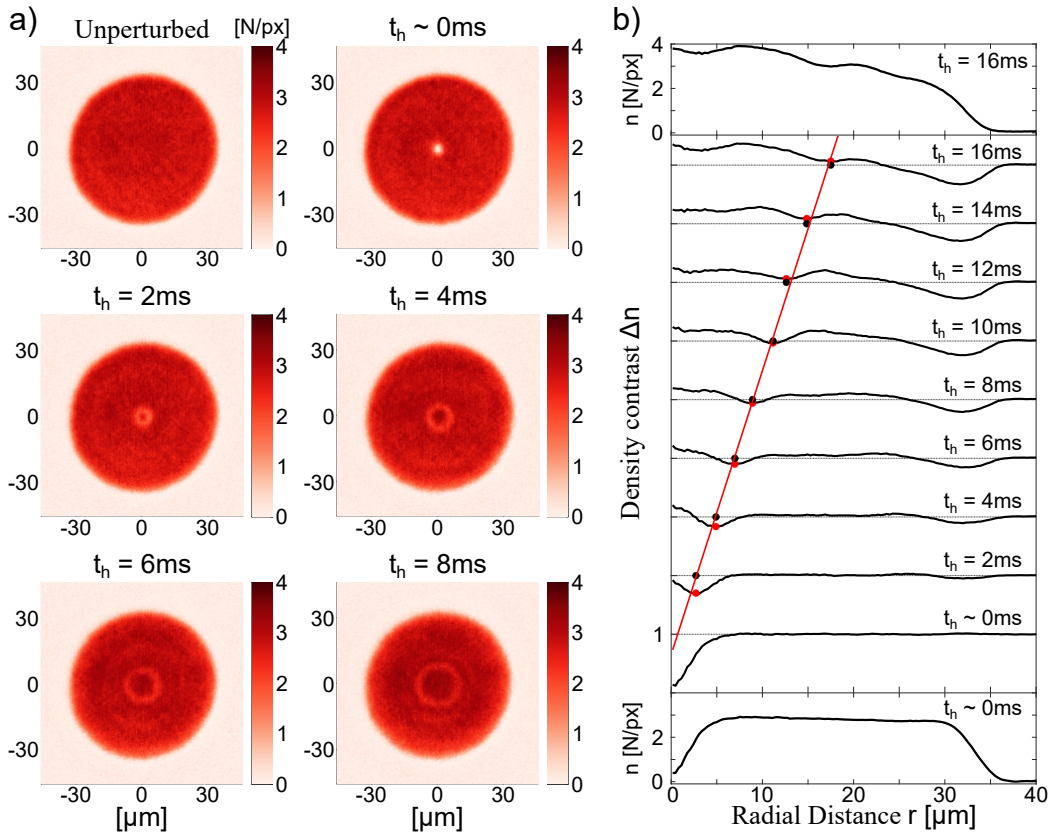

Figure 6.1: Wave-packet measurement to extract the sound speed $c_s = 1/a(t)$ after a 3 ms expansion. A wave-packet is generated by loading the BEC into a potential with a central peak. At $t_h = 0$ this peak is switched off, generating a circular wave-packet. a) Mean density profiles over 35 shots at different times t_h. b) Corresponding radially averaged density contrasts (defined in Eq. 6.4) showing the relative change to the unperturbed profile. Positions of the minima are extracted by parabolic fits and marked with red dots (black dots are projected to $y = 1$). A linear fit on these minimima is used for the extraction of the speed of sound (red solid line). We find $c_s = 1.02(3)$ µm/ms. Full density profiles for the shortest and longest hold times are shown on the bottom and top.

even though we ramp the external potential proportional to the chemical potential. This residual motion can likely be attributed to the change in healing length (from $\xi \sim 0.4\,\mu\text{m}$ to $\xi \sim 1.1\,\mu\text{m}$) that results in less steep edges of the condensate and in turn in an increased bulk density. Note that the largest hold time does not represent this new equilibrium state, but the system is in a breathing motion instead (this motion is shown in App. B).

Fig. 6.1 b) shows radial averages of a simple density contrast to the unperturbed profile

$$\Delta n(r) = \langle n(r,\varphi) - n_{\text{unp}}(r,\varphi)\rangle_\varphi / n_{\text{unp}}(0). \tag{6.4}$$

We extract the dip positions by parabola fits to $\Delta n(r)$. The red dots show the extracted minima, while the black dots show a projection on the x-axis. Only the interval $t_h \in [2\,\text{ms}, 8\,\text{ms}]$ is used to fit the speed of sound, to make sure that the positions are not influenced by the inward moving dip. The red line shows the result of this fit, where we find a sound speed of $c_s = 1.02(3)\,\mu\text{m/ms}$. The same measurement for a faster expansion with $\Delta t = 1.5\,\text{ms}$ over the same range in scale factor results in the same speed of sound. The errors given in brackets are the 1σ standard deviations of the fit, as will always be the case, if not stated otherwise.

6.2 Density Contrast Correlations

To extract the correlations of produced particle pairs and with that gain access to the excitation power spectrum, we extract the equal-time connected correlation function of the density $G_{nn}(t,\mathbf{x},\mathbf{x}') \equiv \langle \delta_c(t,\mathbf{x})\delta_c(t,\mathbf{x}')\rangle$ (Eq. 4.29). The angled brackets denote averaging over all experimental realizations, t is either a hold time t_h in region III or at the end of region I to extract the inital state, δ_c is the density contrast

$$\delta_c(t,\mathbf{x}) = \left(\frac{\bar{N}}{N} n(t,\mathbf{x}) - n_0(t,\mathbf{x})\right) \frac{n_0^{\frac{1}{2}}(t,\mathbf{x})}{\bar{n}_0^{\frac{3}{2}}(t)}. \tag{6.5}$$

In comparison to the definition in Eq. 4.27 we added a normalization factor $\bar{N}/N$ that scales the density of a single realization $n(t,\mathbf{x})$ to the mean density over all realizations to avoid introducing correlations on all length scales from fluctuations of the total number of atoms. Furthermore, the mean density $n_0(t,\mathbf{x})$ is only evaluated for measurements at the same hold time t_h, to reduce the effects of motion of the mean profile, as found in the measurement of the sound speed. The mean density in the center $\bar{n}_0$ is evaluated in a central region with radius 10 px. Measurements in which the mean number of atoms in the central half of the cloud deviates more than 10% from the mean in the data set are discarded, to ensure comparable speeds of sound. We take the innermost 90% of the cloud (in terms of a fit of the radius) to calculate the (equal-time) density-density correlations. Because of homogeneity and isotropy these correlations will only depend on distance. Therefore, we do not have to calculate the four-dimensional object $G_{nn}(t,\mathbf{x},\mathbf{x}')$ (for a fixed time), but instead directly calculate $G_{nn}(t,L)$. For a spatially flat spacetime, L is simply the Euclidean distance $L = \sqrt{(\mathbf{x}'-\mathbf{x})^2}$. Calculating $G_{nn}(t,L)$ is the same as averaging

the full object over space $\mathbf{x}$ (homogeneity) and angle (isotropy), only keeping the distance between the points $\mathbf{x}$ and $\mathbf{x}'$. In practice, the imaging system introduces some anisotropy. However, we are still able to extract spectra from the averaged correlations $G_{nn}(t, L)$ and correct for the anisotropies after the fact. This is described in detail in section 5.5.3.

6.3 Density Fluctuation Power Spectra

Experimentally, we extract the density fluctuation power spectrum from the correlation functions $G_{nn}(t, L)$ via the Hankel transform $\mathcal{HT}$, to be

$$S_k(t) = \frac{m^2 c_s^3}{\hbar k g_{2\mathrm{D}}} \left(1 + \frac{1}{2} k^2 \xi^2\right)^{\frac{3}{2}} \frac{\mathcal{HT}\left(G_{nn}(t, L)\right)}{M^2(k)}. \tag{6.6}$$

This formula includes a lot of details from the previous chapters. The momentum dependent prefactors combine multiple effects of the interatomic interaction that become relevant on the order of the inverse healing length $k \sim \xi^{-1}$. Details on this can be found in section 4.3. The division by the imaging response function $M^2(k)$ corrects for a length scale dependent sensitivity of our imaging system. The fact that we used the Hankel transform $\mathcal{HT}\left(G_{nn}(t, L)\right)$ instead of a Fourier transform results from the azimuthal averaging of the correlations (effectively) performed previously. For this relation between Fourier and Hankel transformations in the context of radial averages, see App. A.1. The imaging system and the imaging response function are discussed in section 5.5.3.

Importantly, absolute quantities are heavily dependent on the uncertainties in the speed of sound c_s that we extracted experimentally. Even more so, because the healing length is also calculated from this number ($\xi \propto 1/c_s$, see Eq. 3.19).

We take 70% of the maximal distance in the correlations to extract the spectra. This is done because at large distances the number of pairs of points $(\mathbf{x}, \mathbf{x}')$ is rather limited, leading to worse statistics. This is equivalent to the cosmic variance problem in cosmology, which describes the lack of statistics for the lowest modes of the CMB [12].

The different steps for the extraction of the density contrast, its correlations and the resulting spectrum is shown in the next section on the example of the initial state of the linear expansion. Data analysis is done using MatLab and code developed and maintained by the group. The Hankel transform is taken from [93].

6.4 Initial State

To characterize the initial state in region I we take the density contrast correlation function calculated from images of the BEC that are taken at $400 a_B$ and calculate a spectrum from those. Figure 6.2 a) shows an exemplary density distribution and its corresponding density contrast. The density contrast correlation function $G_{nn}(t_i, L)$ is shown in b). By construction, it averages over all pairs of points with a distance

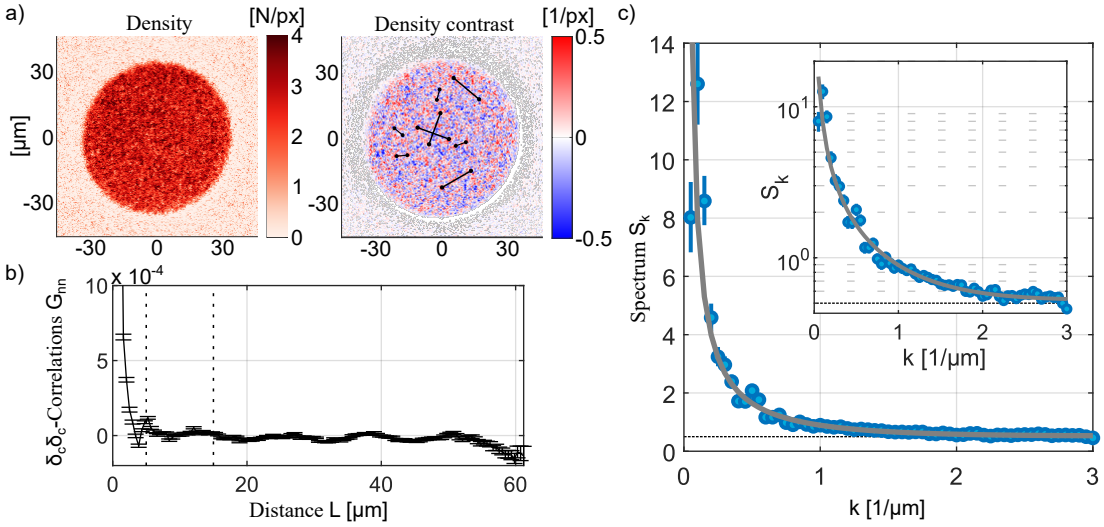

Figure 6.2: Extraction of the density fluctuation power spectrum, shown for the initial state. a) Exemplary density profile $n(\mathbf{x})$ and density contrast $\delta_c(\mathbf{x})$ of the BEC held at $400a_\mathrm{B}$. b) Density contrast correlation function G_{nn} as a function of distance L. This is averaged over all possible pairs of points with distance L and 236 experimental realizations. Exemplary point pairs are shown in a) with their corresponding distances in b) marked as dashed lines. Errorbars represent 1σ standard errors from the statistical fluctuations of the correlations. c) Initial spectrum before the expansion (at $400a_\mathrm{B}$) in linear and log scale (inset). The dotted line marks the level of vacuum fluctuations (1/2). Errorbars represent 1σ standard errors from the statistical fluctuations of the spectra, combined with 1σ errors of $M^2(k)$ and 1σ errors on c_s. The solid curve represents a thermal fit to the data points for $k \geq 0.1\,\mu\mathrm{m}^{-1}$ and of the form shown in Eq. 6.7 We find an initial temperature of 17.4(5) nK and an offset of 0.53(1).

L and is averaged over 236 experimental realizations. Note that the auto-correlation peak at $L = 0$ is on the order 0.04 which is considerably larger than the limit of the y-axis. Errorbars represent 1σ standard errors from the statistical fluctuations of the correlations. The spectrum is shown in c). All errorbars on the spectra are 1σ standard errors from the statistical fluctuations of the spectra, combined with 1σ errors from the extraction of the imaging response function $M^2(k)$ and 1σ errors from the fit of the speed of sound c_s. For the latter, asymmetric error bounds were calculated from the limits of the confidence interval for c_s because of its non-linear contribution in the spectrum.

The initial state is not described by vacuum in every mode, that is 1/2 for all modes. Instead, we expect that the initial occupation N_k^{in} can be described by a Bose-Einstein distribution with some temperature T and $\Delta N_k = 0$. This leaves us with a spectrum of the form

$$S(k) = \frac{1}{e^{\frac{\hbar\omega(k)}{k_B T}} - 1} + \frac{1}{2}, \tag{6.7}$$

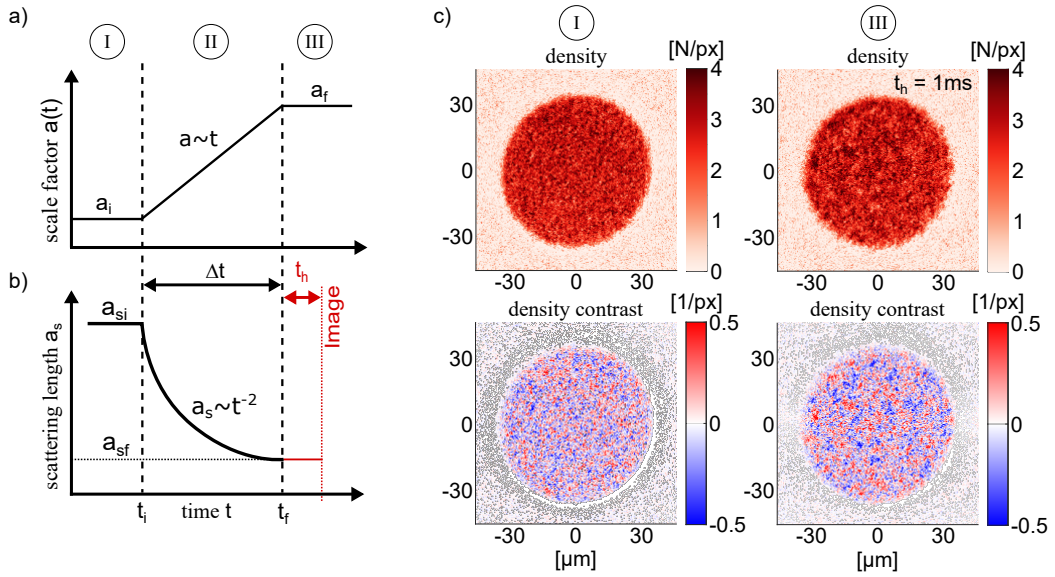

Figure 6.3: a) Schematic of the linear expansion. After region I of constant scale factor (a_i), the scale factor increases linearly in region II over a timescale Δt. In region III the scale factor is again constant (a_f). b) Corresponding time dependence of the scattering length. After the ramp has finished, the scattering length is held constant for an adjustable hold time t_h. This enables state tomography. c) Density distributions and corresponding density contrasts (defined in Eq. 6.5) for the initial state in region I and after the expansion in region III with $t_h = 1\,\mathrm{ms}$. The images show the result of a single experimental realization in region I and III respectively.

with $\omega(k)$ the Bogoliubov dispersion relation and k_B the Boltzmann constant. The solid gray line in Figure 6.2 c) shows a fit of this form, but with a free offset B instead of 1/2. We find that the initial state is well described by a thermal state with $T = 17.5 \pm 0.5\mathrm{nK}$ and $B = 0.53(1)$. The errors in the extracted quantities are 1σ standard errors from the fit of the thermal spectrum.

An incoherent initial occupation of the modes will result in stimulated particle production[49]

$$S_k = \left(1 + 2N_k^{\mathrm{in}}\right) S_k^{\mathrm{vac}}, \tag{6.8}$$

where S_k^{vac} is the spectrum we would have measured for vacuum as the initial state, which was our assumption in the previous chapters. This expression can be found by plugging a thermal state into Eq. 2.26 where we get $2\langle\hat{N}\rangle + 1$. For the intitial state, without a change in scale factor and particle production, $S_k^{\mathrm{vac}} = 1/2$, and we get Equation 6.7.

6.5 Linear Expansion Scenario

A straightforward expansion scenario is the linear expansion $a^{\mathrm{II}}(t) = a_{\min}(1 + H_0 t)$. In 2+1 dimensions this corresponds to a matter-dominated universe [65].

We implement this by decreasing the scattering length from an initial value in region I $a_{s,i} = 400 a_{\mathrm{B}}$ to a final value $a_{s,f} = 50 a_{\mathrm{B}}$ in region III in a short time Δt with the form $a_s \sim t^{-2}$. This is depicted in Fig. 6.3 and corresponds to an expansion of a factor $a_f/a_i = \sqrt{8}$.

Fig. 6.3 c) shows density distributions and corresponding density contrasts δ_c from single experimental runs before and after such an expansion over $\Delta t = 1.5\,\mathrm{ms}$. Enhanced fluctuations that are connected in larger patches are clearly visible. The change in scattering length also results in less suppression of density fluctuations by the interaction energy (see section 4.3). For this reason, even with an adiabatically slow change in the interaction, stronger fluctuations would have been observed, and further analysis is required to attribute some of this to the particle production process. Similarly to what one expects from a classical pair of particles with zero net momentum ,i.e $\mathbf{k}_1 = -\mathbf{k}_2$, we expect fluctuations to be correlated over distances that increase with time. Because the phonons considered here are massless, they move at the speed of sound c_s.

Fig. 6.4 shows density contrast correlations $G_{nn}(t_h, L)$ at different hold times for a fast expansion with $\Delta t = 1.5\,\mathrm{ms}$ (a) and a slower expansion with $\Delta t = 3.0\,\mathrm{ms}$ (b). The plots show an equally spaced subset of the measured hold times, from 0 ms to 15 ms. Longer hold times are shifted along the y-axis. Additionally, the initial state before the ramp is shown as the lowest (unshifted) line. Errorbars represent 1σ standard deviations from the statistical distribution of the measurement outcomes over a set of ~ 60 shots. The precise numbers depend on the data set. We find that the expansion produced a feature consisting of a positive correlation peak and a trailing anti-correlation dip that linearly moves to larger distances over time. The red line shows, as a guide to the eye, a slope corresponding to an increase in distance that is twice the measured speed of sound. This is the growth in distance that we would expect from a pair of particles moving at c_s in opposite directions and evidence for the pair production of quasi-particles. The longer ramp shows a similar signal, but with much less intensity as well as starting at larger distances. The same line now trails the anti-correlation dip instead of the correlation peak. This is evidence that correlations already begin to build (and move) during expansion.

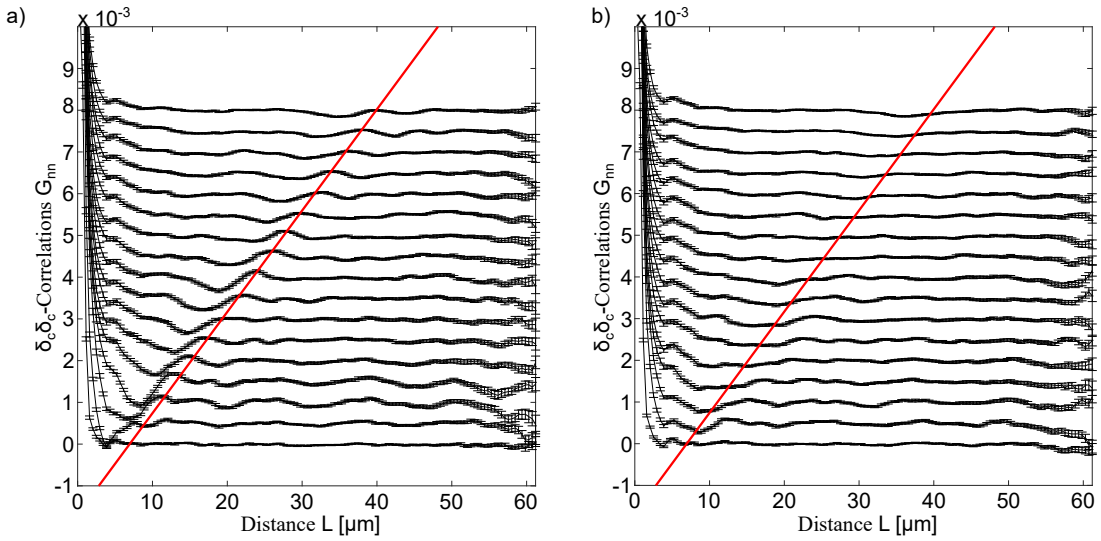

Figure 6.4: Density contrast correlations after a 1.5 ms expansion (a) and a 3 ms expansion (b) by a factor $a_f/a_i = \sqrt{8}$. The lowest lines show the initial correlations before the expansion, the higher ones a subset of all measured t_h, that are spaced by 1 ms and shifted along the $y-$axis. For the short expansion we find a correlation peak closely followed by an anti-correlation dip that move linearly in time and to larger distances. The red solid lines depict a distance increasing with twice the speed of sound, extracted previously. This is the kind of signal we expect for a pair of massless particles with opposite momenta. For the long expansion times, a similar signal is observed, albeit weaker. Additionally, the same line now follows the anti-correlation dip instead of the peak. Errorbars represent 1σ standard errors from the statistical fluctuations of the correlations (over ~ 60 realizations).

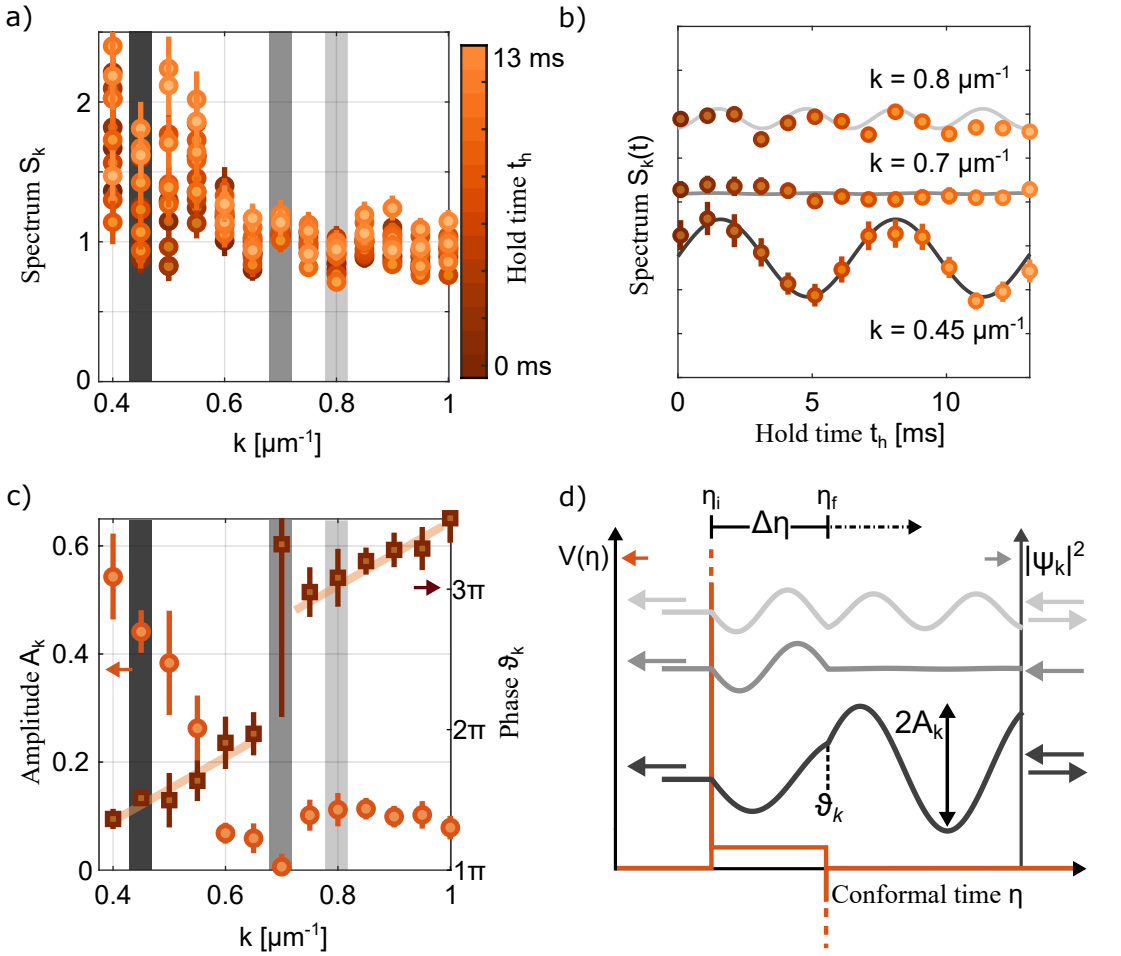

Figure 6.5: Ramsauer minimum from resonant forward scattering. a) Extracted spectra for a subset of hold times spaced by 1 ms. While most momenta show a large time-dependence some others do not. b) Coherent oscillations are visible in the individual momentum modes and corresponding cosine fits. Note that their $y-$axis is shifted for better visibility. While the hold times shown are equally spaced, the complete set is sampled pseudo-logarithmically and the fits are performed over the first two periods. c) Extracted amplitudes and phases from the fit on the coherent oscillations. The minimum in oscillation amplitudes falls together with a π phase shift in the extracted phases (solid lines are a guide to the eye). This can be understood in terms of the involved scattering states shown in d). The densities $\left|\psi_k^{\mathrm{III}}\right|^2$ reveal that this specific momentum oscillates with a half-period that exactly fits into the box potential. As a consequence it is not reflected and shows no coherent oscillations. Errorbars represent 1σ standard errors of the mean (a and b) or from the fit (c), together with the systematic errors from the modulation transfer function and the sound speed.

6.5.1 Coherent Oscillations and the Ramsauer Minimum

From the density contrast correlation we calculate the spectra for different hold times t_h after the expansion. Figure 6.5 a) shows the spectra after the slower expansion ($\Delta t = 3\,\mathrm{ms}$). We find that the spectrum shows a time dependence, the strength of which depends on the momentum k. These are the coherent oscillations and can be seen when the spectrum of individual momentum modes is plotted against hold time. Figure 6.5 b) shows this for three exemplary momenta. Note that the data is shifted along the y-axis to make the individual modes clearly discernible. The change in interaction strength induces a background motion that was briefly discussed and visible in Fig. 6.1. The effect of this background motion was extracted via another measurement that includes much longer hold times (see Appendix B) and has already been compensated in the shown spectra.

The solid lines in Figure 6.5 b) are cosine fits to the data of the form $A_k \cos(\omega_k t + \vartheta_k) + B_k$, where ω_k was fixed to be within 1σ of the expected Bogoliubov frequency (see Eq. 3.17). The errors in the frequency arise from the fit errors in the speed of sound from which we infer the chemical potential. Although an equally spaced subset is shown in Figure 6.5 b), the hold times were sampled pseudo-logarithmically in the experiment. This was done to ensure a good sampling rate over a wide range of frequencies. Two periods of an oscillation are included in the fit. This means that only the lowest momentum modes are fitted for all hold times. Higher momentum modes are only fitted up to $t_h = 2T_k$, where T_k is the period of the mode. The results for $A_k \hat{=} \Delta N_k^{\max}$ and ϑ_k from the fit of the coherent oscillations can be seen in Figure 6.5 c). We find a minimum in the oscillation amplitude A_k around $k = 0.7\,\mu\mathrm{m}^{-1}$. The phases ϑ_k of the modes just below or above this momentum differ by almost π. Solid lines are meant to serve as guides for the eye and show a linear relationship between k and ϑ_k left and right of this minimum. This is expected in the acoustic regime where $\omega_k \sim c_s k$. The inverse healing length ξ^{-1} is on the order of the highest momenta shown in the Figure.

We can turn to the scattering picture to understand where this minimum in coherent oscillations and the coinciding shift in phase come from. Figure 6.5 d) shows the corresponding potential and probability densities of exemplary scattering states below the resonant momentum, above the resonant momentum, and at the resonant momentum, which shows the minimum in amplitude. The measurements of the spectrum at different hold times t_h correspond to the measurements of these probability densities at different conformal times η. The standing wave contribution then shows up as coherent oscillations. The resonant momentum is the one with a half-period that fits exactly into the box potential. Interference of incoming and reflected components in region II make $|\psi_k|^2$ periodic inside the potential. The result is resonant forward scattering at the potential and no reflection. We can also interpret this as destructive interference of the reflections at η_f and η_i (and multiple scattering events). Therefore, there is no standing wave contribution in the outgoing state ψ_k^{III} and no coherent oscillations. This also means $b_k = 0$ and that no particles are produced. Momenta just below and above the resonance show an opposite sign in b_k and therefore in the complex reflection amplitude, showing up as a π difference

in ϑ_k. This phase shift is present in all modes above the resonance, making the phase a good indicator of this phenomenon. The resonance effect shows up with or without the singular contributions to the potential in the form of delta peaks that also contribute to the scattering (see section 2.4). They coincide with the potential steps of the box potential and share the same symmetry (opposite sign). The values of a_k and b_k of all off-resonant momenta are affected by their existence.

The resonance phenomenon is known from particle scattering and (in the context of electron scattering) is named after its discoverers, the Ramsauer-Townsend effect [94, 95]. In their experiments, electrons were scattered off of noble gases. Independently, the two found that the scattering cross section depends on the momentum of the called and shows minima, especially for low momenta. This was unexplainable at the time (1921), and Niels Bohr doubted the discovery in a letter to Albert Einstein: "...Ramsauer's almost crazy assertion (in Jena) that the path length of electrons in argon becomes infinite with decreasing speed (the atoms are freely flown through by slow electrons!)." (translated from German, [96]) The resonance effect was only explained after the development of quantum mechanics. He later admitted his mistake and acknowledged that this resonance effect can indeed be explained by "de-Broglies wave-mechanics".

We can also interpret this in the squeezing picture. After the original squeezing operation at t_i this mode experienced exactly a π rotation in phase space before the opposite anti-squeezing operation is applied. The result is the symmetric original state that does not show coherent oscillations and does not include extra particles. This heavily depends on the right amount of phase accumulation between the two operations, which is given for the resonant momentum. Additionally, both potential steps (at η_i and η_f) as well as the singular contributions need to be of equal magnitude. In reference [97] the authors investigate this squeezing and anti-squeezing formalism in context of cosmological inflation and find that it produces oscillations of the power spectrum in momentum space (Sakharov oscillations [98]) with minima for maximal desqueezing.

If this resonance condition is valid, one should be able to find more of these resonances for higher momenta that also fit into the box potential. For this we have to leave the acoustic regime.

6.5.2 Beyond the Acoustic Regime

To interpret the data beyond the acoustic regime, the full Bogoliubov dispersion relation needs to be included. In this section, we compare the experimental data with a fully acoustic model that assumes $\omega_k = c_s k$ for all k where the potential is given by 2.34 and an extended model that takes into account the complete Bogoliubov dispersion and the dispersive potential 4.25. Both models include an initial thermal state that is extracted from a fit to the initial state. All models shown are courtesy of our theory collaboration partners. Details on the derivation of the theory curves can be found in [99] and [50].

Figure 6.6 a) shows the fit results for phase ϑ_k, amplitude $A_k \hat{=} \Delta N_k^{\max}$, and offset $B_k \hat{=} N_k + 1/2$, along with the predictions of acoustic theory (dashed lines) and the

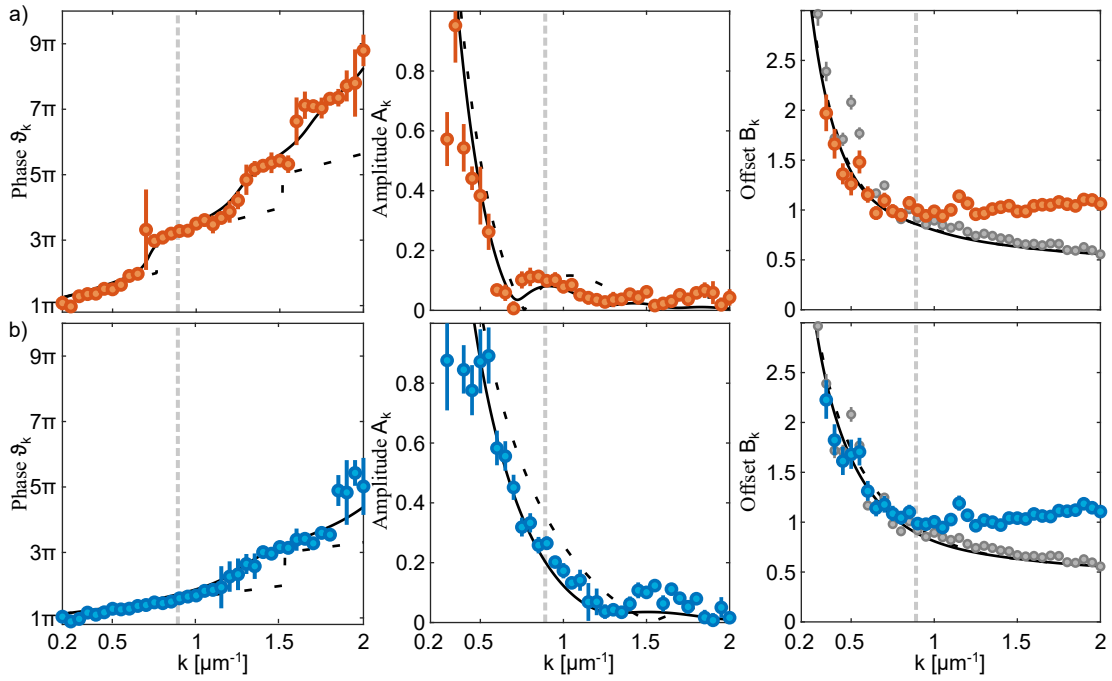

Figure 6.6: Comparison of the coherent oscillations to theory predictions. Phase, amplitude and offset as extracted from the cosine fits after a 3.0 ms expansion (a) and a 1.5 ms expansion (b). Gray dots in the offset mark the initial state. Dashed lines show theory predictions from acoustic theory, and solid lines from an extension to the full Bogoliubov dispersion. The vertical dashed line marks $\xi^{-1} \sim 0.9\,\mu\text{m}^{-1}$. The N_k and ΔN_k have been scaled by 1/2 to match the observations of A_k and B_K. Errorbars represent 1σ standard errors on the fit of the oscillations. For A_k and B_K this is quadratically added to systematic uncertainties from the errors on the Modulation transfer function and the speed of sound. Theory models are courtesy of our collaboration partners and adapted from [92].

extended model (solid lines). Vertical dashed lines mark the inverse healing length ξ^{-1}. This is the scale on which we expect deviations from the acoustic approximation and is at the high end of the momentum region considered so far.

In the extracted phases, we find the higher resonances of the slow expansion at $k \sim 1.2\,\mu\text{m}^{-1}$ and $k \sim 1.6\,\mu\text{m}^{-1}$, in addition to the first resonance at $k \sim 0.7\,\mu\text{m}^{-1}$. In b), we show the data of the faster ramp with $\Delta t = 1.5$ ms. The second resonance of the slow ramp coincides with the first one of the fast ramp. This is expected as its potential width is exactly half of the width of the slow expansion. In principle, there is a small shift between the two because the potential height also differs by a factor of four. However, the absolute heights with $\frac{1}{4}\dot{a}^2(\eta) = 0.01\,\mu\text{m}^{-2}$ for the slow expansion and $0.04\,\mu\text{m}^{-2}$ for the fast expansion are small. They correspond to momenta $k = 0.1\,\mu\text{m}^{-1}$ and $k = 0.2\,\mu\text{m}^{-1}$, respectively. Modes with momenta lower than that, would be tunneling through the potential and correspond to the decaying modes in cosmology [53, 100]. Because in the scattering picture the equivalent eigenenergies vary with k^2, the difference in potential heights does not yield a significant shift at

the resonance positions (see Eq. 2.33).

We find that the full model is much better at describing the data, especially for the phases at high momenta. Because the healing length and thus the momentum dependence of the potential changes during the ramp, the symmetry of the potential is broken and reflections are not fully suppressed at resonance. Instead of zero amplitude and a phase jump, we find a small amplitude and the phase jump being smeared out over a small range of momenta. To match the extracted amplitudes and offsets with the theoretical results for ΔN_k (and N_k) all models shown in this thesis had their resulting ΔN_k and N_k multiplied by 1/2. Additionally (for this scenario), Δt was modeled to be 10% less than the set value and c_s is reduced by $\sim 10\%$ of the measured value, possibly reflecting imperfections in the experimental form of the magnetic field ramp.

Finally, the experimental results for the offset B_k diverge from the model at high momenta. This might be the result of some other noise source that appears in the offset and is greatly exaggerated by the Bogoliubov prefactor, which gets large for small ξ^{-1}. This noise source is not present (to this extend) in the initial state (gray points), where it would be even more prominent in comparison to the strongly suppressed density fluctuations. A possible explanation could be an unintentional transfer of atoms to another minimum of the lattice in z-direction that provides the confinement to two dimensions.

6.6 Sinusoidally Periodic Scenario

By making the scale factor a periodic function in time, we can implement periodic cosmologies. For those, we can expect the particle production to increase with the number of periods, making them a prime scenario for investigating the process. As we will see in experimental data, the periodicity in time shows up as a periodic structure of the density fluctuations in space. We show that this is connected to particle production being dominated by a few narrow bands of resonant momenta, which correspond to the band gaps of the periodic potential.

For the first of these experiments we oscillate the scale factor with

$$a(t) = \frac{a_\mathrm{i} + a_\mathrm{min}}{2} + \frac{a_\mathrm{i} - a_\mathrm{min}}{2} \cos(\omega t). \tag{6.9}$$

This is implemented by a corresponding oscillation of the scattering length between $200a_\mathrm{B}$, setting a_i, and $400a_\mathrm{B}$, which sets a_min. We always perform full periods, such that $a_i = a_f$. Figure 6.7 shows density contrast correlations and their time evolution for different hold times t_h after two and four periods. We find a correlation feature consisting of several correlation peaks and anti-correlation dips moving to larger distances. The red line is meant as a guide to the eye and corresponds to movement at twice the speed of sound. After four periods the signal is more pronounced. Additionally, it periodically extends to even larger distances.

We can again calculate the spectra and fit the coherent oscillations. The results are shown in Fig. 6.8. After one period (a), the offset does not differ significantly

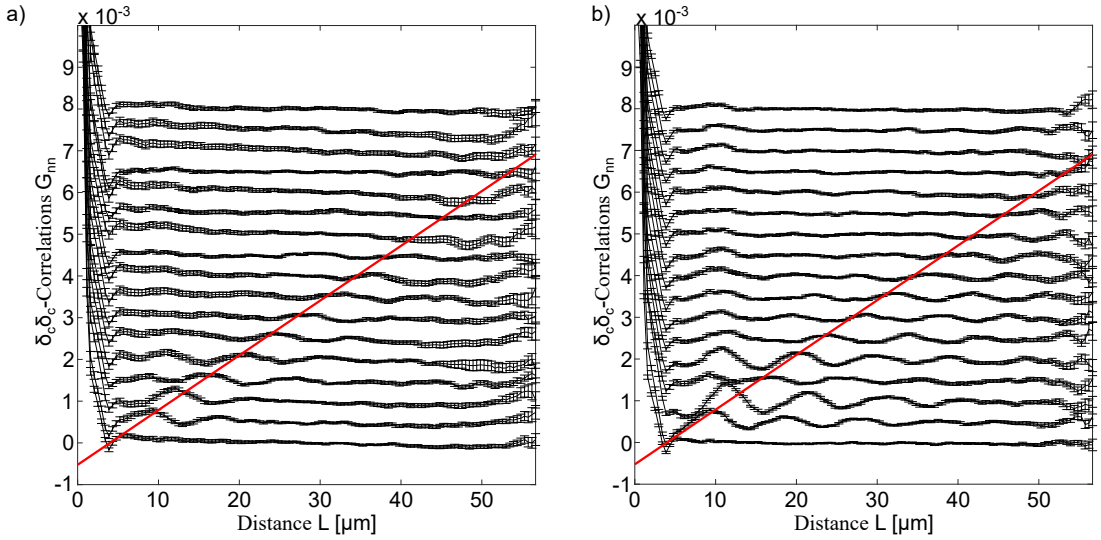

Figure 6.7: Density contrast correlations after two periods (a) and four periods (b) of a periodically contracting and expanding spacetime (in the form of a cosine). The lowest lines show the initial correlations before the expansion, the higher ones a subset of all measured t_h, that are spaced by 1 ms and shifted along the $y-$axis. Again, we find a correlation feature moving with twice the speed of sound as indicated by the red line. More periods make this signal more pronounced. Additionally, it periodically extends to larger distances.

from the initial spectrum (gray dots). However, the amplitude reveals significant coherent oscillations at low momenta. These are accompanied by a slope in the phase. For two and more periods, the amplitude forms a peak that is also visible in the offset. More periods lead to a growth of both A_k and B_K and a steeper phase profile across the narrowing peak. This is expected because the accumulated relative phase of the different momenta grows during the time evolution.

The solid lines show theory predictions including the Bogoliubov dispersion. The N_k and ΔN_k have, again, been scaled by 1/2 to match the observed values of A_k and B_K. For a low number of periods they model the data of the amplitude well. At four periods, the model is overestimating the peak. This could be due to loss channels in the experiment that lead to the decay of the coherent oscillations and inhibit their growth. The offset shows a discrepancy to the model for intermediate momenta. This missing offset is already present in the initial state, which is not well described by a thermal spectrum in this regime. A possible explanation for this could be a reduced thermalization time of only 50 ms (compared to 100 ms used for the other experiments).

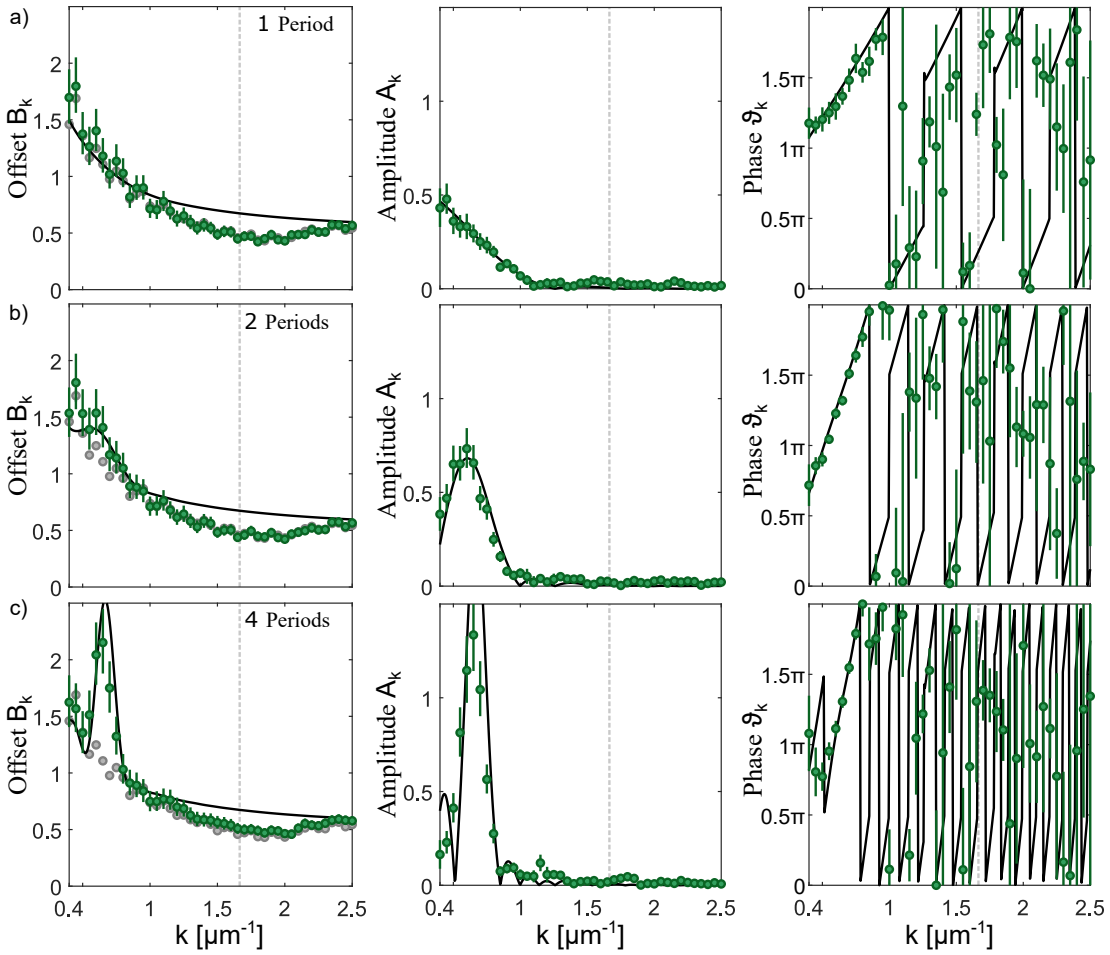

Figure 6.8: Coherent oscillations after a period of contracting and expanding spacetime. The scale factor is modulated in a sinusoidal fashion over one period (a), two periods (b), and four periods (c). With increasing periods offset and amplitude grow at a specific momentum and the corresponding peak narrows. ξ^{-1} is indicated with a dashed line. Theory predictions are marked with solid lines. The N_k and ΔN_k have been scaled by 1/2 to match the observations of A_k and B_K. Measurements of the initial spectrum are depicted as gray dots. Errorbars represent 1σ standard errors on the fit of the oscillations. For A_k and B_K this is quadratically added to systematic uncertainties from the errors on the Modulation transfer function and the speed of sound.

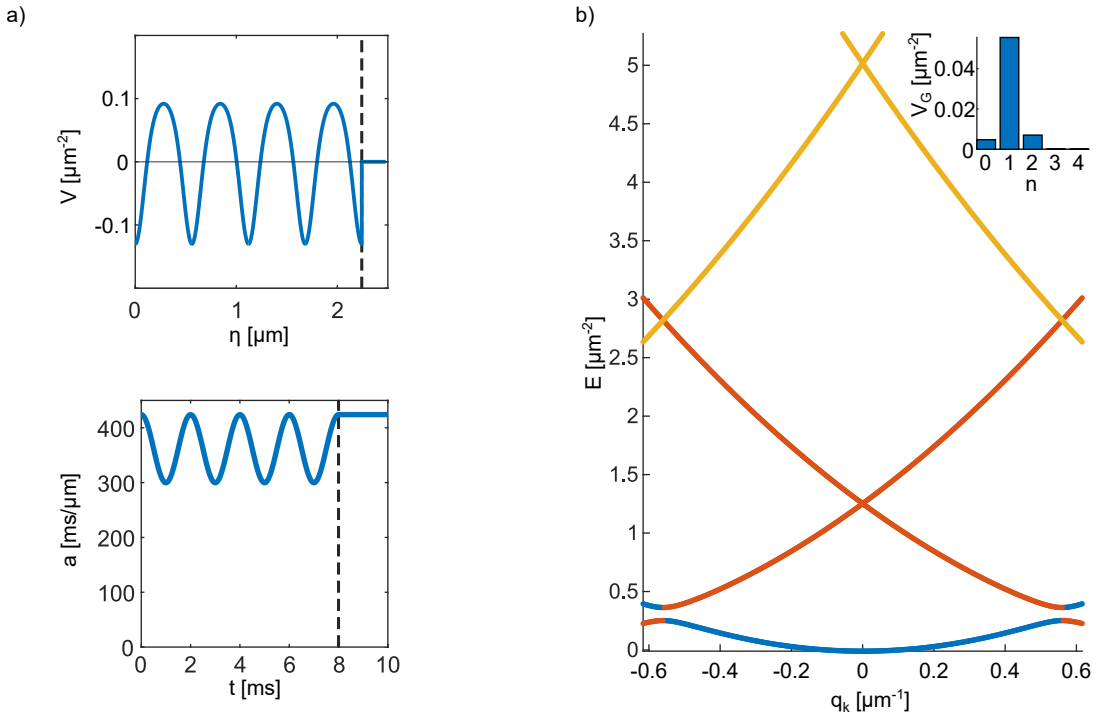

Figure 6.9: Band gap description of the phenomenon found for the sinusoidal modulation of the scale factor (see Fig. 6.8). a) The sinusoidal modulation of the scale factor corresponds to a periodic potential. The dashed vertical lines mark $\eta_h = 0$ and $t_h = 0$. b) Numerically calculated band-structure of the potential in (a) extended to infinite length. The Fourier components V_G of the potential (inset) are dominated by the first Fourier component. This leads to a single band gap opening up. Free states at energies in the gap can not propagate through the potential, but are reflected instead, leading to the single observed peak.

The growth of a single peak can be understood as a result of the periodic structure of the potential. The potential is periodic in $\Delta\eta$. In the limit of infinite number of periods, its Fourier components V_G are non-zero only for $k = n2\pi/\Delta\eta =: G_n$. This can then be used to build the Schrödinger Equation (2.33) in Fourier space:

$$\hat{p}^2\psi_k + V_G * \psi_k = E_k\psi_k, \tag{6.10}$$

where $*$ denotes a convolution with V_G, that couples pairs of modes with $\Delta k = G_n$. This is solved by Bloch-states and the eigenenergies form a band structure that is gapped at $q_k = G_n/2$, where q_k is the quasi-momentum in the potential. Results from numerical diagonalization of this are shown in Fig. 6.9 b). For this potential form, the first Fourier component is dominating, and only a single (first) gap is substantial and resolvable numerically. That said, a perfectly sinusoidal potential does have higher band gaps that decrease in width as energy increases [101]. While the new eigenstates inside the potential that are far off the gap are virtually unchanged, the eigenstates directly above and below the gap are a superposition of the (free) $\pm k$ states. To first order, a single gap translates into a single peak in the spectrum. Free modes with energies in the band gap cannot propagate in the periodic potential, but are reflected instead.

This is similar to Bragg-scattering on the periodic potential of a crystal [102]. Instead of probing the crystal structure with a monochromatic source where reflection occurs at the Bragg-angle, we probe the one-dimensional periodic potential with a wide range of momenta and reflection occurs for the resonant one.

In practice, the potential is far from infinitely extended, and the Schrödinger equation has solutions where the infinitely extended potential has gaps. These will show a decay from period to period as they penetrate deeper in the potential (which does not mean that the solution is not oscillating in between, in contrast to tunneling modes of the box potential). This leads to an exponential decay of the transmission amplitude as the number of periods is increased and in turn an exponential growth of the particle production. This can be interpreted the following way. To match the energy inside region II to the ones in region I and III, where $E_k = k^2$, the quasi-momentum corresponding to the state in the gap must have an imaginary part. This result comes naturally in a transfer matrix approach to the problem [103, 50].

6.7 Cusp Periodic Scenario

To get a richer band structure, we choose a potential landscape that has higher Fourier components. For this, we produce a potential of regularly spaced peaks. We find that this opens multiple band gaps for which particle production is measured. Additionally, we are able to measure a significant signal of squeezing below the level of vacuum fluctuations for some momentum modes.

One of the peaks is realized by a cusp-like modulation of the scale factor of the form

$$a(t) = \frac{a_\mathrm{i}}{\sqrt{2}}\left[1 - 1/2|\cos(\omega t)|\right]^{-1/2}. \tag{6.11}$$

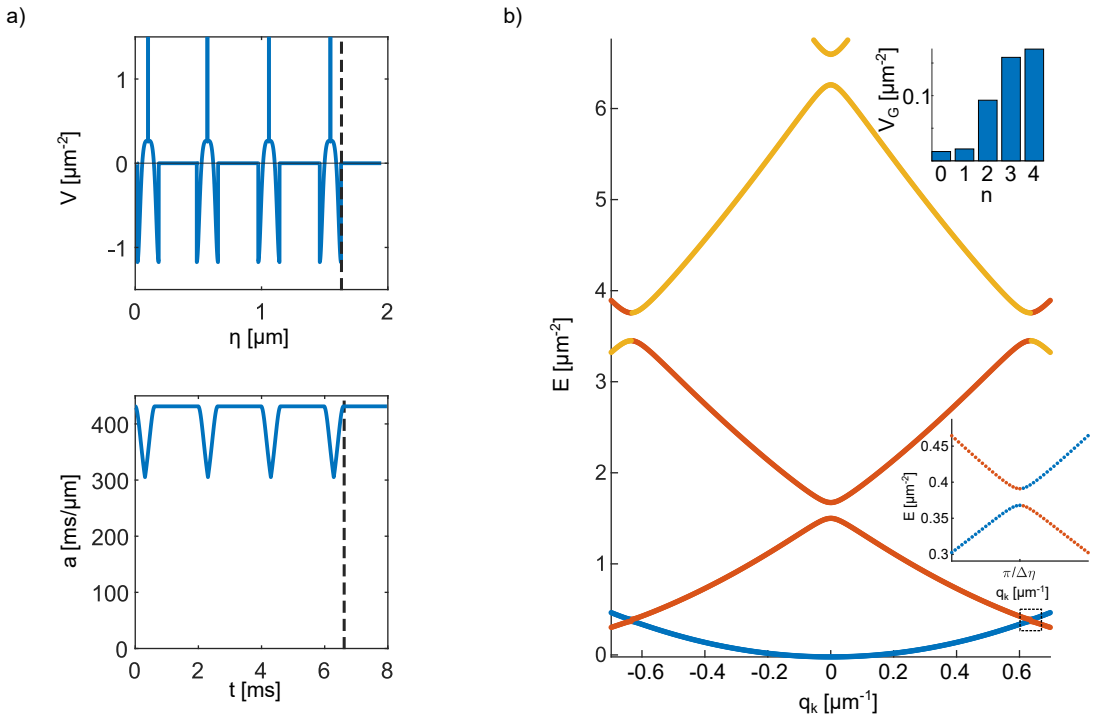

Figure 6.10: a) A potential consisting of periodic δ-peaks can be implemented by maximizing the irregular terms of the potential. This is done by including turning points in the scale factor (of the form given in Eq. 6.11). The dashed vertical lines mark $\eta_h = 0$ and $t_h = 0$. b) Numerically calculated band-structure of the δ peak potential in (a) extended to infinite number of periods. The Fourier components V_G of the potential (inset) are much larger than observed previously. Multiple band gaps open up. The first band gap is small but resolvable numerically and shown in the inset.

A single cusp is generated by this modulation over half a period of the cosine. In theory, the turning point generates a δ-peak contribution to the potential. In the experiment, changes in the magnetic field are limited by inductance of the coils and timescales of the magnetic field control. Therefore, the δ-peaks will be of some finite height and width. To keep the external potential in sync with the real magnetic field, we delay DMD power by 200 µs. We again take a_i to be the scale factor at $200a_B$. The peak is then at $400a_B$. This time, $\omega/(2\pi) = 800$Hz. However, we set the periodicity by keeping the scale factor constant at a_i between two peaks, such that the cusps are spaced by $\Delta t = 2$ms.

Figure 6.10 a) shows the functional form of the scale factor together with the corresponding potential. The potential shows a functional form going to negative values, in addition to the peaks. This is a consequence of the fact that every potential must support a zero energy bound state, which makes only positive δ-peaks impossible [50]. The Fourier components $n > 1$ are indeed much larger than before and multiple band gaps open up. In turn, particles are produced at various resonant momenta that correspond to the position of these gaps.

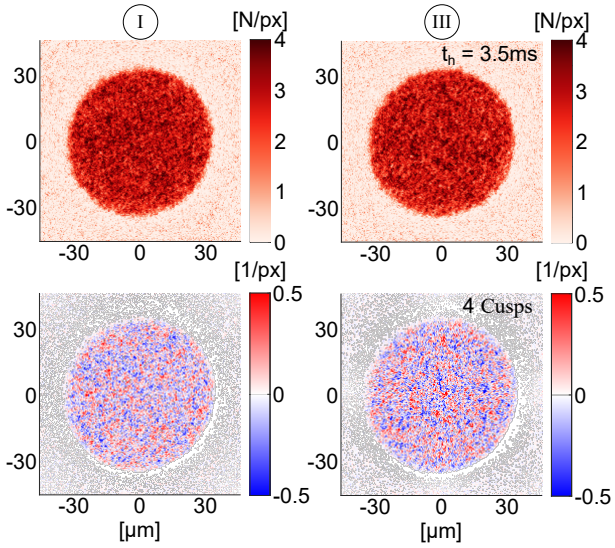

Figure 6.11: Density and density contrast of the initial state and after four cusps and a hold time $t_h = 3.5\,\mathrm{ms}$.

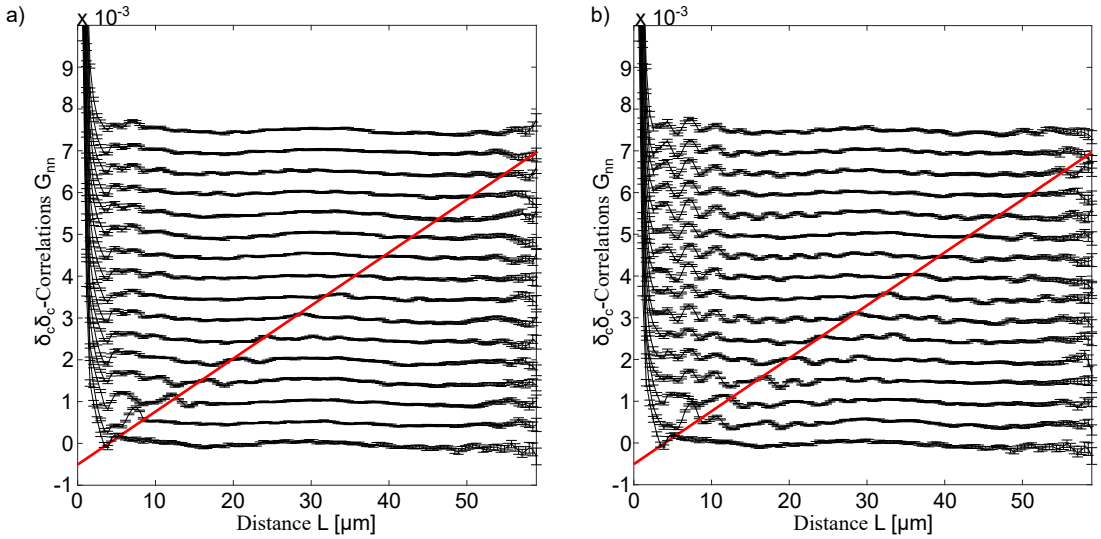

Figure 6.12: Density contrast correlations after one peak in the potential (a) and after two peaks (b). The lowest lines show the initial correlations before any modulation of the scale factor. These show larger statistical errors (1σ standard error) because of a factor three less statistics. The other lines are shifted along the y-axis and show hold times t_h, that are spaced by 1 ms. Again, we find a correlation feature moving with twice the speed of sound as indicated by the red line. More cusps make this signal more pronounced and extend to larger distances. In addition to the moving correlation feature, the buildup of correlations at smaller distances is also clearly visible.

Figure 6.11 shows the density distributions and corresponding contrasts of two randomly chosen single realizations, one of the initial state and one after four peaks and $t_h = 3.5\,\mathrm{ms}$. Because the interaction strength in region I and region III are identical, the increase in density fluctuations can be interpreted as a result of particle production. Density contrast correlations of an equally spaced subset of hold times can be found in Figure 6.12 and reveal a correlation signal moving at twice the speed of sound. In this experiment, we also clearly see a non-moving correlation building up at short distances for two (and more) cusps.

Figure 6.13 shows the results of fits of the coherent oscillations for one, two, four and six cusps (a-d). After a single peak we find elevated amplitudes over a broad range of momenta, while the offsets are comparable to the initial spectrum (gray points). Note that the statistics for the initial state is much weaker (21 realizations as compared to ~ 65 for all other hold times and multiple hold times are combined in the fit of the offset).

For two cusps the resonant momenta emerge in the form of increased amplitudes and offsets. For more cusps these peaks grow rapidly, both in offset and amplitude. Each peak is accompanied by a slope in the phase that, again, increases with the number of cusps. Solid black lines show a theory model including the full Bogoliubov dispersion relation. Again, the N_k and ΔN_k are scaled by 1/2. Additionally, a lag of the magnetic field control of 230 µs and a slightly adjusted value for $c_s = 1.91\,\mu\mathrm{m/ms}$ (compared to a measured value of $cs = 1.97(3)\,\mu\mathrm{m/ms}$) was used. These additional corrections were not necessary for the sinusoidal form. Then, the model describes the observations very well for one and two cusps. This also shows that the initial state is well described by an initial thermal distribution that is included in the model. For more cusps, we find very different growth rates of the different peaks.

One contribution to this is the experimental form of the scale factor ramps. The jump in the first derivative of the scale factor will certainly be a ramp over some finite time and with some delay to the input signal. This is supported by the fact that a delay had to be introduced for the theoretical predictions to match the observed phases, which is of the same order as the delay of the external potential. A difference in the corresponding potential can have very different effects on the growth rates of the individual peaks. Another contribution will be the multiple loss channels that are present in the experiment, but not in the theoretical model. For example, scattering processes between different momenta will lead to a net loss of particles from the resonant modes. A sign of this process could be the increase in the offset on all scales in comparison to both the initial state and the theoretical prediction for four and six cusps. This effect affects not only the offset, but even more so the coherences that make up the amplitudes. More on this is discussed at the end of this chapter.

This can also be interpreted as an example of Bragg reflection and calculated using the transfer matrix method [50, 103].

Because the peaks are localized in time, we can think of them as applications of a squeezing operator similar to the edges of the box potential. Between two peaks, the state evolves freely. If the phase space rotation is a multiple of π, the next squeezing operator is applied exactly at the squeezed axis. If not for the losses, one could expect the resonant momentum modes to show more squeezing with every additional cusp.

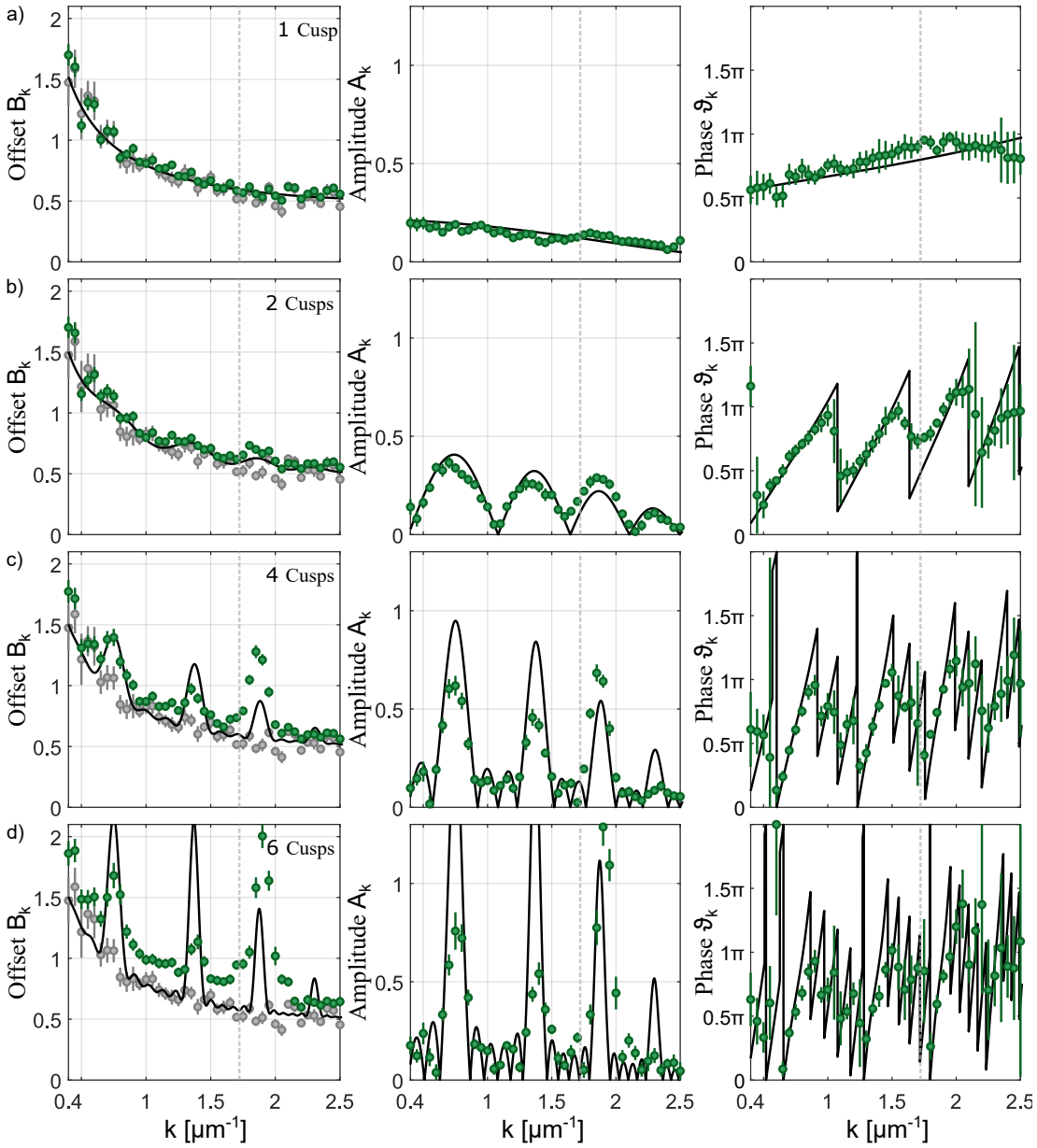

Figure 6.13: Bragg scattering at the δ-peaked potential. (a) to (d) show one, two, four and six cusps, respectively. Because all gaps are open, we find multiple (main) peaks in the offsets and amplitudes. Theory predictions are marked with solid lines. While they capture the experimentally extracted structure, relative growth rates of the different peaks divert from the model. ξ^{-1} is indicated with a dashed line. The N_k and ΔN_k have been scaled by $1/2$ to match the observations of A_k and B_K. Errorbars represent 1σ standard errors on the fit of the oscillations. For A_k and B_K this is quadratically added to systematic uncertainties from the errors on the Modulation transfer function and the speed of sound.

6.7.1 Squeezing Below the Level of Vacuum Fluctuations

Squeezing of a momentum mode below the level of vacuum fluctuations corresponds to S_k oscillating below 1/2. Figure 6.14 a) shows the spectra after a single peak for very short hold times ($t_h = 200 - 1100\,\mu s$). b) shows the same after two peaks. The errorbars now represent 3σ standard errors of the statistical fluctuation of the spectra, combined with 3σ standard errors of the statistical fluctuation of the imaging sensitivity and from the fit of the speed of sound. Points with black outlines mark the shortest hold time $t_h = 200\,\mu s$ and gray points show the initial spectrum before the ramp. Because this is meant as a comparison, its error bars only show the 3σ standard error from statistical fluctuations. Note that its statistical fluctuations are larger than those of the spectra after the ramp because of a factor of three less statistics. We find that the spectra drop below 1/2 for multiple momentum modes, both after one and two cusps. This equates to less density fluctuations than expected with classical correlations at this length scale and in turn indicates a squeezed state. We find these modes at the intermediate momentum range at or slightly above ξ^{-1}, where the influence of the initial thermal state gets small (Eq. 6.8).

Figures 6.14 c) and d) show the coherent oscillations for the wavenumbers $k \in [1.7\,\mu m^{-1}, 2.05\,\mu m^{-1}]$. Consecutive modes are shifted by 1/2 along the y-axis. Error bars on the data points are again the 3σ standard errors described above. Solid lines show the results from the fits with the values shown before in Fig. 6.13. Multiple data points breach the level of vacuum fluctuations that is marked as solid horizontal lines. We find that this signal is robust for changes in the size of the analyzed region of the cloud and even persists for an analysis without the reference picture optimization (see the Appendix C).

The fitted oscillations clearly show that the offset $B_k \hat{=} N_k + 1/2$ is greater than 1/2, while coherent oscillations with amplitude $A_k \hat{=} \Delta N_k^{\max} > N_k$ make the spectrum fall dynamically below 1/2. Figure 6.15 shows the difference of the extracted offsets and amplitudes after one, two, four and six peaks (a-d). The errorbars represent 3σ standard errors from the fit and covariance of the two parameters, again combined with the errors of imaging sensitivity and speed of sound. Solid black lines show the theory model from before and horizontal lines mark 1/2. In these extracted quantities, we also find a significant signal for squeezing below the level of vacuum fluctuations.

For more peaks, we do not find such a signal. Not only do the errors grow larger, but the means are also larger than 1/2 for most (4 cusps) or all momenta (6 cusps). The errors are not unexpected as both the offset and the amplitude grow and these large numbers are subtracted (see growing B_k and A_k in 6.13). However, the means should indicate more and more squeezing of the resonant momentum mode with every cusp of the potential. This is also predicted in the model. For four and more cusps, squeezing should be detectable in the lowest resonant momentum (first peak), even though its thermal initial occupation is large. Instead, the data diverge from the model. The fact we do not see squeezing below the level of vacuum fluctuations for four and more cusps indicates that effects that destroy the coherence of the particle pairs are important at this timescale. These are not included in the theory.

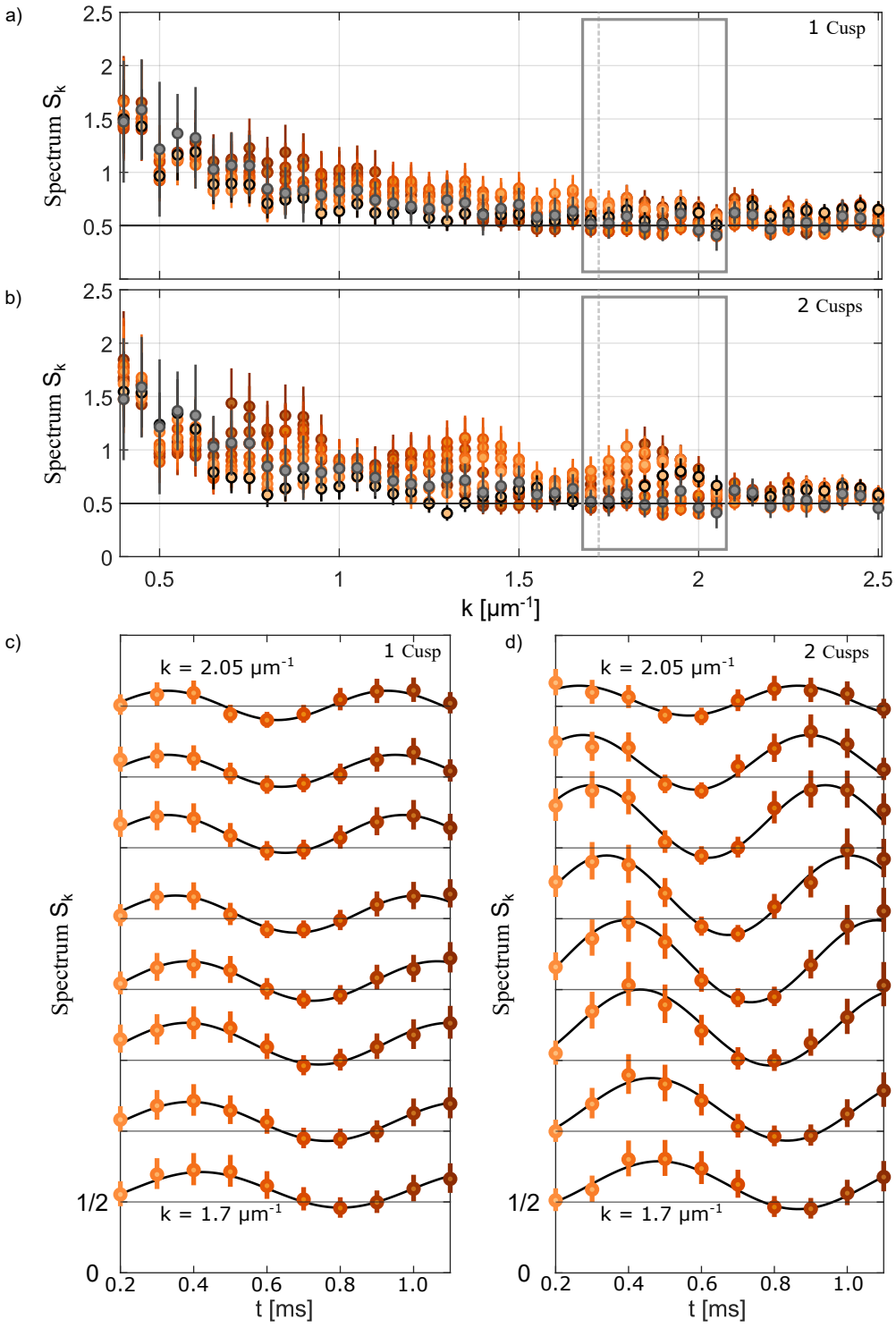

Figure 6.14: (a) Spectra after two cusps and for the shortest hold times $t_h \leq 1.1\,\mathrm{ms}$. Black outlines mark the shortest hold time $t_h = 200\,\mu\mathrm{s}$. b) Corresponding coherent oscillations and fit functions of the momenta ($k \in [1.7\,\mu\mathrm{m}^{-1}, 2.05\,\mu\mathrm{m}^{-1}]$). Squeezing of a momentum mode below the level of vacuum fluctuations corresponds to data points below 1/2 (horizontal lines). Solid lines are the fits shown in Fig. 6.13.

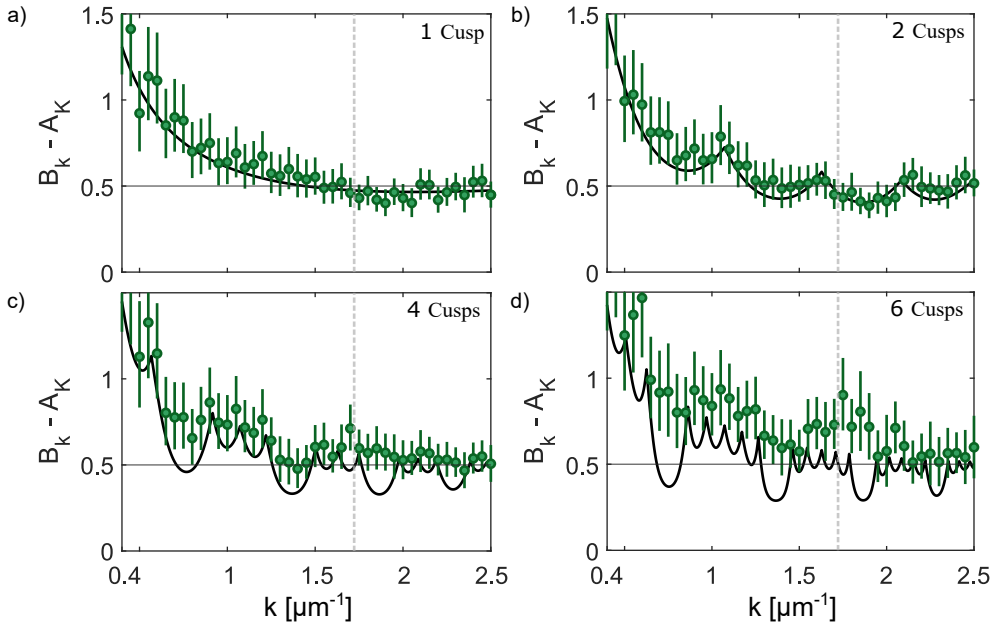

Figure 6.15: Testing for squeezing and entanglement in the extracted amplitudes and offsets. Squeezing of a momentum mode below the level of vacuum fluctuations (horizontal line) corresponds to $B_K - A_k < 1/2$. a) to d) show this quantity for one, two, four and six cusps. Solid lines are the theory model from Figure 6.13. The dashed vertical line marks ξ^{-1}. The errorbars represent 3σ standard errors of the fit of the oscillations (including the covariance of the two parameters) as well as of the systematic uncertainties from the errors on the modulation transfer function and the speed of sound.

Possible Mechanisms for the Loss of Coherence

The perfect correlation of particle occupations in opposite momentum modes can be destroyed by single loss events from one of the momentum modes. This can happen as a result of quasi-particle interactions between the mode of interest and the thermal contribution. Even though it redistributes momentum and energy from the original momentum to other ones, it is an effective loss from the original mode. By truncating the Hamiltonian at quadratic order in the derivation of the Bogoliubov dispersion, we neglected these interactions. These interactions are referred to as Landau damping [104]. Additionally, a phonon can decay into two lower energy phonons (Beliaev damping [105]). In two or more dimensions, both processes have on-shell contributions that are momentum and energy conserving. After long times the coherent oscillations will damp out as a result of these processes and the occupations show a thermal distribution [106]. The increased mode occupations on all momenta after six peaks might already show the onset of the redistribution towards a thermal spectrum.

The finite size of our system can also have similar effects because reflection at the boundaries will destroy the correlations (but does not redistribute the absolute momentum k). Similarly, restricting the analyzed region to something smaller than

the cloud size results in effective losses because we essentially trace out a subsystem.

There are also loss mechanisms for the atoms from the trap. In three-body losses two atoms form a molecule while a third ensures the conservation of momentum and energy. Typically, both the molecule and the third atom are lost from the trap, leading to particle loss and an increase in noise from heating [107].

7 Conclusion

7.1 Summary

In this thesis, we further deepened the connection between superfluids with time-dependent interaction strength and quantum field theory on curved spacetimes, by investigating the analogy to the one-dimensional quantum mechanical scattering problem that is described by a Schrödinger equation. We measured an analog to cosmological pair-production in expanding spacetimes in a BEC with a time-dependent interaction strength. In this analog simulator, the scale factor can be increased by a decrease in the speed of sound, which in turn increases the proper lengths in the system. This was done for multiple expansion scenarios. An analysis of the spectra showed an increase in (phononic) quasiparticles and coherent oscillations, which are a result of the quasi-particles being produced in pairs. For a linear expansion scenario, we were able to explain a previously found phenomenon [47], namely the vanishing particle production and the jump in phase for some momenta. We identified this as resonant forward scattering on the potential with zero reflection amplitude, which translates to no particle production. This is equivalent to the Ramsauer-Townsend effect, a known scattering phenomenon which was first found in the context of electrons scattering on noble gases. We were able to confirm the resonance hypothesis, by identifying multiple higher energy resonances in an energy regime beyond the acoustic approximation. Similarly, we found scattering resonances with large quasiparticle production for periodic spacetimes. This was identified as Bragg reflection in the scattering analogy. Because of the shape of the potential, only the lowest band gap opened in the corresponding band structure, and we found a single narrow peak of resonant momenta after multiple oscillations. Finally, we designed a scattering potential that consists of many equally spaced peaks by implementing cusped-shaped peaks in the scale factor. This led not only to the opening of many band gaps and

resonant momenta but also to a fast growth of their occupations. In this scenario, we found that the spectra fall dynamically below the level of vacuum fluctuations, equivalent to the shot noise (in this work at 1/2). This can be interpreted as a witness for entanglement. The data presented in this work showed a significant signal of squeezing below the level of vacuum fluctuations for an intermediate momentum regime close to ξ^{-1}. This has, to our knowledge, not been demonstrated before (for $k\xi \gg 1$ in [45]).

7.2 Outlook

The validity of the analogs as well as some of the findings in this work have implications for similar experiments involving superfluids. Furthermore, some of the phenomena found require future investigations. Other cosmologically motivated phenomena could also be within reach of the current or future capabilities of the simulator. This section is briefly outlines some of them.

7.2.1 Squeezed States and Entanglement

Some scenarios have been shown to produce squeezing below the level of vacuum fluctuations. Since this means that the particles are entangled, it could be used to study entanglement and its dynamics. For example, one could investigate the entanglement between different regions of the condensate, possibly at distances that are related to the hold time in the static region (III). This would be particularly interesting for modes that are deep in the phononic regime, where information is expected to propagate at the speed of sound. Such a study could be combined with the implementation of curvature through specific density profiles, as has previously been shown in our experiment [47].

To experimentally achieve squeezing deep in the phononic regime $k\xi \ll 1$, there are multiple aspects to consider. Going to lower temperatures helps to narrow the initial spectrum and therefore the offset from thermal occupations, especially in the low momentum regime. Extending the acoustic regime can be achieved by higher densities and interactions. However, this might have detrimental effects on the Landau and Beliaev damping rates discussed before and an increase in particle loss combined with an increase in heating through three-body losses. This is a trade-off that needs to be optimized. To alleviate the effects of finite size, it might help to construct something periodic, or mimic periodicity by a highly reflective square box that can then be analyzed with a periodic Fourier transformation.

The experimental schemes shown in this work could also be used to produce squeezed phonon modes at specific momenta. This is, for example, of interest for quantum metrology [108]. There, the reduced variance in one variable can be used to enhance the precision of a measurement.

The scattering framework could help to design the optimal time dependence of the scale factor to either specifically target momenta (periodic potential) or cover a wide range (peaked potential). Typically considered is the sinusoidal driving of the

scattering length to achieve large populations of a momentum mode. Here we have found that the precise form of the excitation spectra depends on the shape of the equivalent scattering potential. Although this is dominated by the driving frequency in the limit of large offset scattering lengths and small driving amplitudes, this is not true in the regime of large drives. To minimize the influence of loss of coherence, the large driving regime might, however, be the regime in which to produce this initial state.

Ultimately, optimizing these parameters requires a quantitative understanding of the different mechanisms contributing to the damping. From there it might be possible to identify an ideal parameter regime. Steps in this direction from a theoretical point of view have been taken in [59].

7.2.2 Cosmologically Motivated Questions

Reheating

The thermalization process that we regarded as unwanted damping for the generation of the squeezed states could be interesting itself. It has been proposed to be an analog for the reheating process in the early universe after the inflationary period [109, 110].

Beyond Density Excitations

Several hyperfine states of the atoms which are miscible in a BEC can behave as an effective spin and can produce a spinor condensate [111]. These support additional excitations, for example spin-waves, with their own speed of sound. This gives more freedom for the construction of metrics, for example, including a sound horizon in the spin from a background flow, without a supersonic flow (in terms of density speed of sound) [112]. Similar considerations are valid to obtain an extended ergoregion of a rotational fluid flow (vortex) [113]. In addition, these systems can benefit from advanced readout techniques of the final state [114].

Alternatively, topological excitations of the single species condensate in the form of vortices are expected to obey the acoustic metric. Because the vortex-vortex interaction depends on the sign of the phase winding, they could behave analogously to massive charged particles [115]. This is also interesting in combination with the implementation of spatial curvature through specific density profiles because curvature would modify the phonon mediated interactions of the vortices.

Backreaction

Throughout this thesis, we assumed a classical metric that depends only on the mean field density. This defined the spacetime for the quantum field filling it. However, one can ask how this changes if the fluctuations of the metric induced by quantum fluctuations of the density are considered. There exist a variety of theoretical results and concrete proposals for experiments testing this in analog cosmology experiments and the context of inflationary preheating [116, 117].

While it is not hard to imagine a quantum superposition of density distributions in our experiment, this is closely related to the question of what the gravitational field of a massive object in a spatial superposition is [118]. Both could be interpreted as a superposition of metrics, which is a possible top-down approach to investigate quantum effects in gravity [119].

A

Appendix: Imaging Response

Here we show details on the asymmetry of the momentum cut-off of the imaging system. Figure A.1 shows the mean density distribution of a BEC at $400\,a_{\mathrm{B}}$. In fact, this is the initial state from the ramp measurements. An extraction of the spectra, equivalent to the thermal clouds in section 5.5.3 shows that the asymmetric cut-off is the result of the overlap of two circular cut-offs. As discussed in the main text, this is the result of a tilt of the imaging beam relative to the axis of the objective. As a result, the objective acts as an off-center cut-off in the Fourier-plane. After the phase information is lost on the imaging sensor, the Fourier transformation of the real-valued images produces a symmetrized version of the cut-off in the spectrum. Below the inner cut-off we find some substructure in the spectrum. This is a result of imaging aberrations. Beyond that cut-off, momenta $\mathbf{k}$ that make it through the objective have their counterpart $-\mathbf{k}$ blocked. The result is a general loss of signal, but also of the interference resulting in this substructure.

A.1 Relation of Two-Dimensional Fourier-Transformation and Zero-Order Hankel-Transformation

We want to show that

$$\int_{\varphi} \mathcal{FT}(f(r,\varphi)) = \mathcal{HT}(f(r)), \tag{A.1}$$

with $f(r) = \int_{\varphi} f(r,\varphi)$ and $\mathcal{HT}$ denoting the 0^{th} order Hankel transformation as defined in the main text and below. First, we expand $f(r,\varphi)$ to multipoles

$$f(r,\varphi) = \sum_{m=-\infty}^{\infty} f_m(r) e^{im\varphi} \tag{A.2}$$

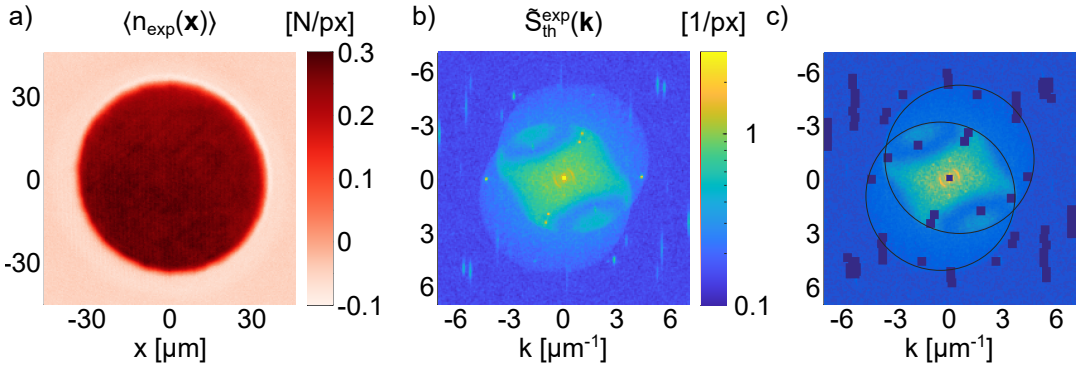

Figure A.1: Mean density distributions a) and two-dimensional density fluctuation power spectra like defined in Equation 5.16. c) Masked spectrum covering the fringes overlayed with two circles of the size of the theoretical momentum cut-off, illustrating the asymmetric cut-off.

and note that $f(r) = 2\pi f_0(r)$. The two-dimensional Fourier-transformation will separate in the same set of symmetries

$$\mathcal{FT}(f(r,\varphi)) = 2\pi \sum_{m=-\infty}^{\infty} i^{-m} e^{im\varphi} F_m(k), \tag{A.3}$$

where

$$F_m(k) = \int f_m(r) J_m(kr) r \mathrm{d}r \tag{A.4}$$

is the m^{th} order Hankel-transform. Again, a radial integral will eliminate all but the 0^{th} order

$$\int_{\varphi} \mathcal{FT}(f(r,\varphi)) = 2\pi F_0(k) = \mathcal{HT}(f(r)). \tag{A.5}$$

This identity is a result of the property of the Fourier-transformation to retain the symmetries of the real space function.

B

Appendix: Slow Oscillations of the Spectra

In 6.5 we found that the mean density after an interaction quench (that is equivalent to an expansion scenario in our analog system) shows some kind of breathing motion and a density wave moving inwards. This is attributed to the sudden change in healing length. Effects from the imperfections of the external potential (and its finite height) are mitigated by ramping the height of the potential (i.e. light power) together with the interaction. Here we show that the background motion results in oscillations of the extracted spectra that can be well characterized by a cosine fit. This is then compensated for in the extracted spectra after all expansions.

Figure B.1 (a) shows the mean density profiles after an expansion over $\Delta t = 1.5\,\mathrm{ms}$ for different hold times. The data shown in the main text is only taken up to $t_h = 15\,\mathrm{ms}$. This is a different dataset that includes much longer hold times up to $t_h = 60\,\mathrm{ms}$. We find a density wave moving inwards and an increase in mean density in the center. In contrast, the peaked scenario in b) does not show these features, at least not to a comparable extend.

Figure B.2 shows density fluctuation power spectra for the highest momenta that were extracted in the analysis. Because their coherent oscillations are orders of magnitude faster than the timescales shown, we can clearly see the slow oscillations induced by the background motions. Red lines show a fit of the form

$$S_k(t) = d + a\cos(\omega t). \tag{B.1}$$

with the free parameters offset d, amplitude a and angular frequency ω.

Figure B.3 shows results from the fit for all extracted momenta. We find that the angular frequency (c) is independent of momentum and a mean value of $\omega = 125(1)\,\mathrm{s}^{-1}$ (for $k > 0.5\,\mathrm{\mu m}^{-1}$). This is consistent with the modulation being the result of a breathing motion. Deviations at low momenta can be attributed to a less well defined separation between their slowly oscillating coherent oscillations

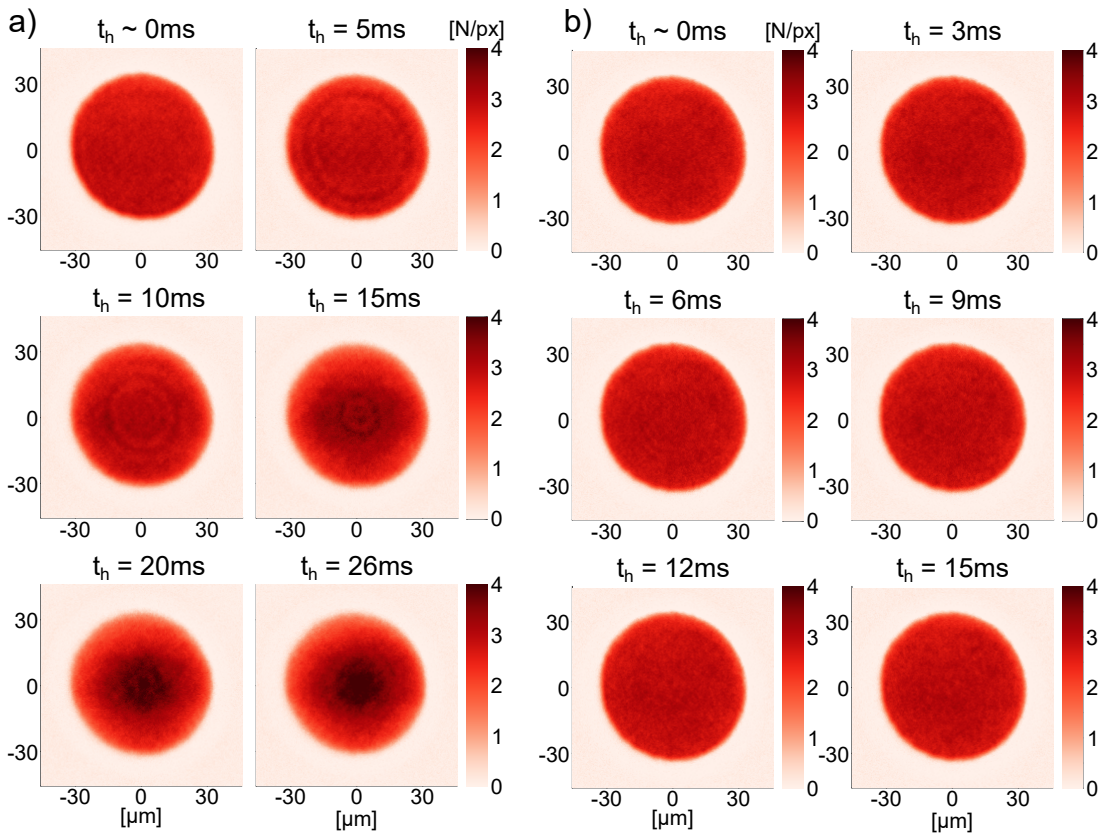

Figure B.1: Mean density distributions for long hold times after a fast expansion over $\Delta t = 1.5\,\mathrm{ms}$ (a) and after a single cusp (b). In a) we find a inward moving density waves and a breathing motion of the density. In b) we do not find this breathing motion. Note that while the hold times differ between the two cases, the sound speed does as well making the shown timescales comparable. Note that data for a) is from a different data set than whats shown in the main text.

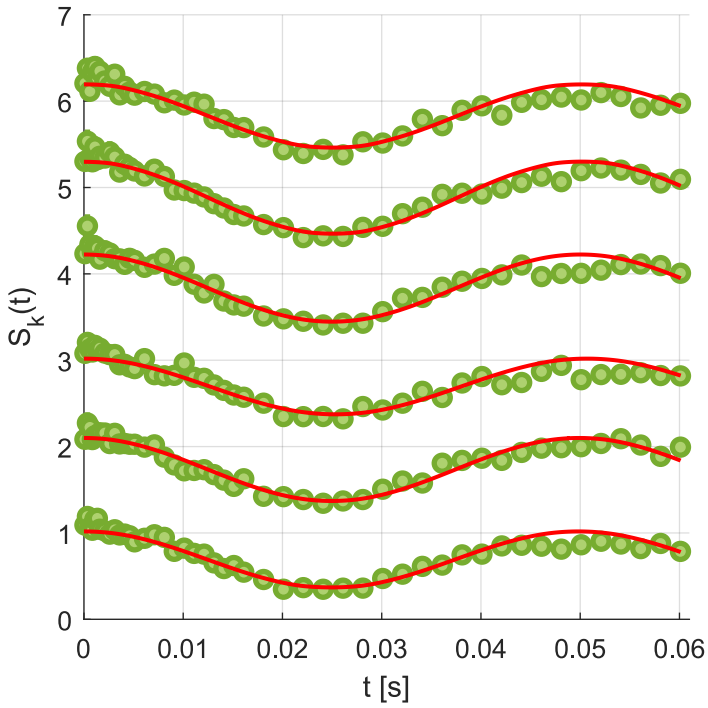

Figure B.2: Slow oscillations found on top the coherent oscillations of the individual modes for $k \in [1.95\,\mu\text{m}^{-1}, 2.2\,\mu\text{m}^{-1}]$ (highest extracted momenta). The extra oscillation is in contrast to the coherent oscillations not momentum dependent. Solid lines are fits of the form $d + a\cos(\omega t)$ with free fit parameters offset d, amplitude a and frequency ω. All fit results can be found Figure B.3.

and the breathing motion. Although the offset and amplitude show a momentum dependence, their ratios are again constant. We find a mean value of $a/d = 0.48(1)$

Overall, we conclude that we can compensate for this slow modulation by applying

$$S_k(t) = \frac{1 + \frac{a}{d}}{1 + \frac{a}{d}\cos(\omega t)} \tilde{S}_k(t) \tag{B.2}$$

to the extracted spectra $\tilde{S}_k(t)$. This is close to one for small times. Because coherent oscillations are only fitted over two periods, this does not influence the fit results at high momenta. This treatment was not applied to results from the periodic scenarios.

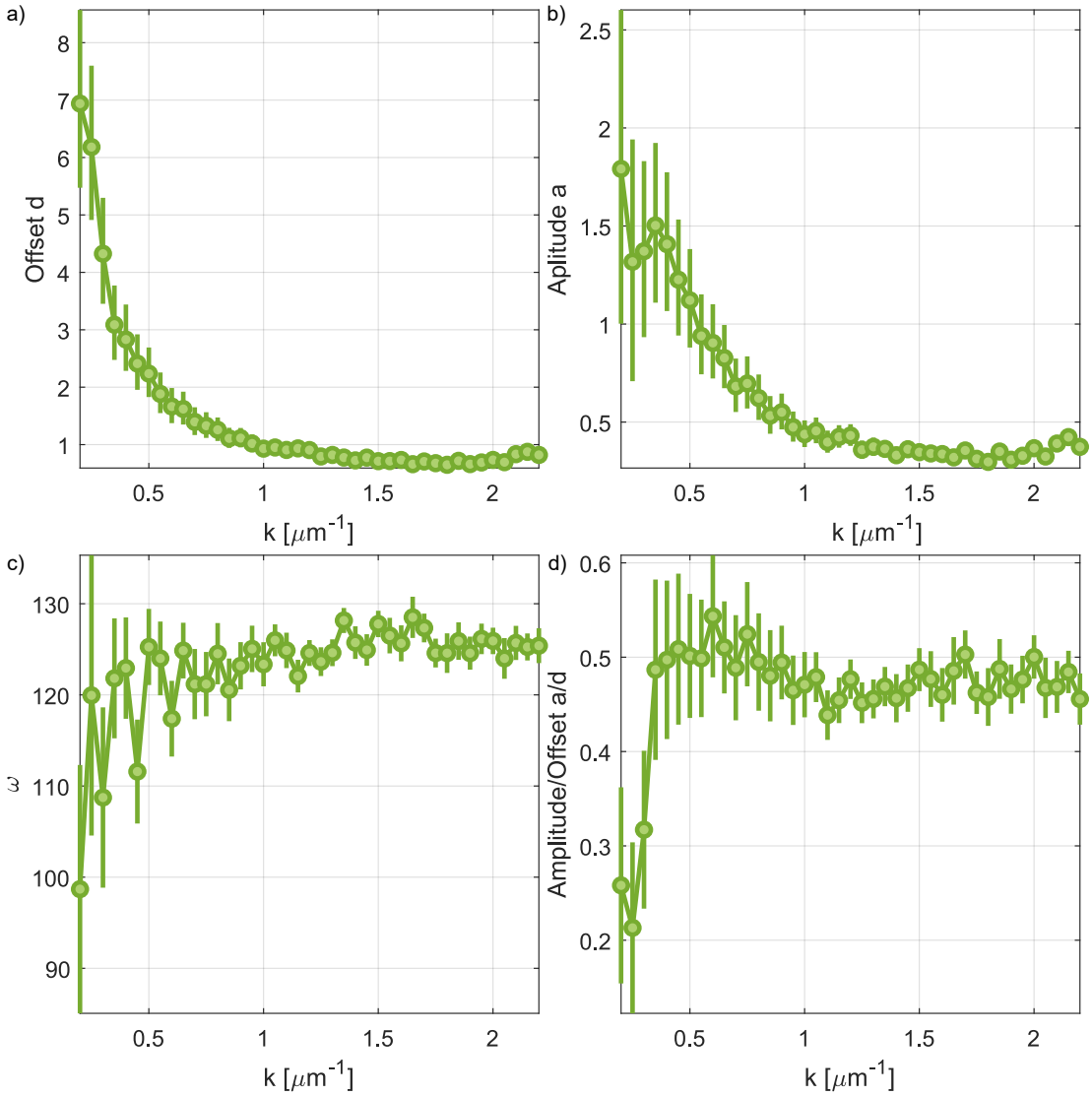

Figure B.3: Fit parameters of the cosine fits to the oscillations of the spectra. The frequency increases slightly with k, has an oscillatory behavior for high k and large errors for small k. The average over all values for $k > 0.5\,\mu\text{m}^{-1}$ is $125(1)/(2\pi)$ Hz and is not far off of most fitted values. Importantly, the ratio of amplitude a and offset d is also a constant. Besides low k it shows again an oscillatory behavior around a mean value of 0.48(1) (for $k > 0.5\,\mu\text{m}^{-1}$).

C

Appendix: Squeezing for Changes in the Analysis

We tested multiple sizes for the analyzed region between 70% of the radius and the full size and found comparable results that drop below the level of vacuum fluctuations in all cases. Figure C.1 shows the analysis of the full cloud as an example.

In addition, we tested the importance of optimizing the reference picture. The result is shown in Figure C.2 (for the original region size of 90%). We find that even without the removal of the additional noise from imaging light we find some data points significantly below the level of vacuum fluctuations. We find a slight tendency towards larger offsets and larger errors, as expected.

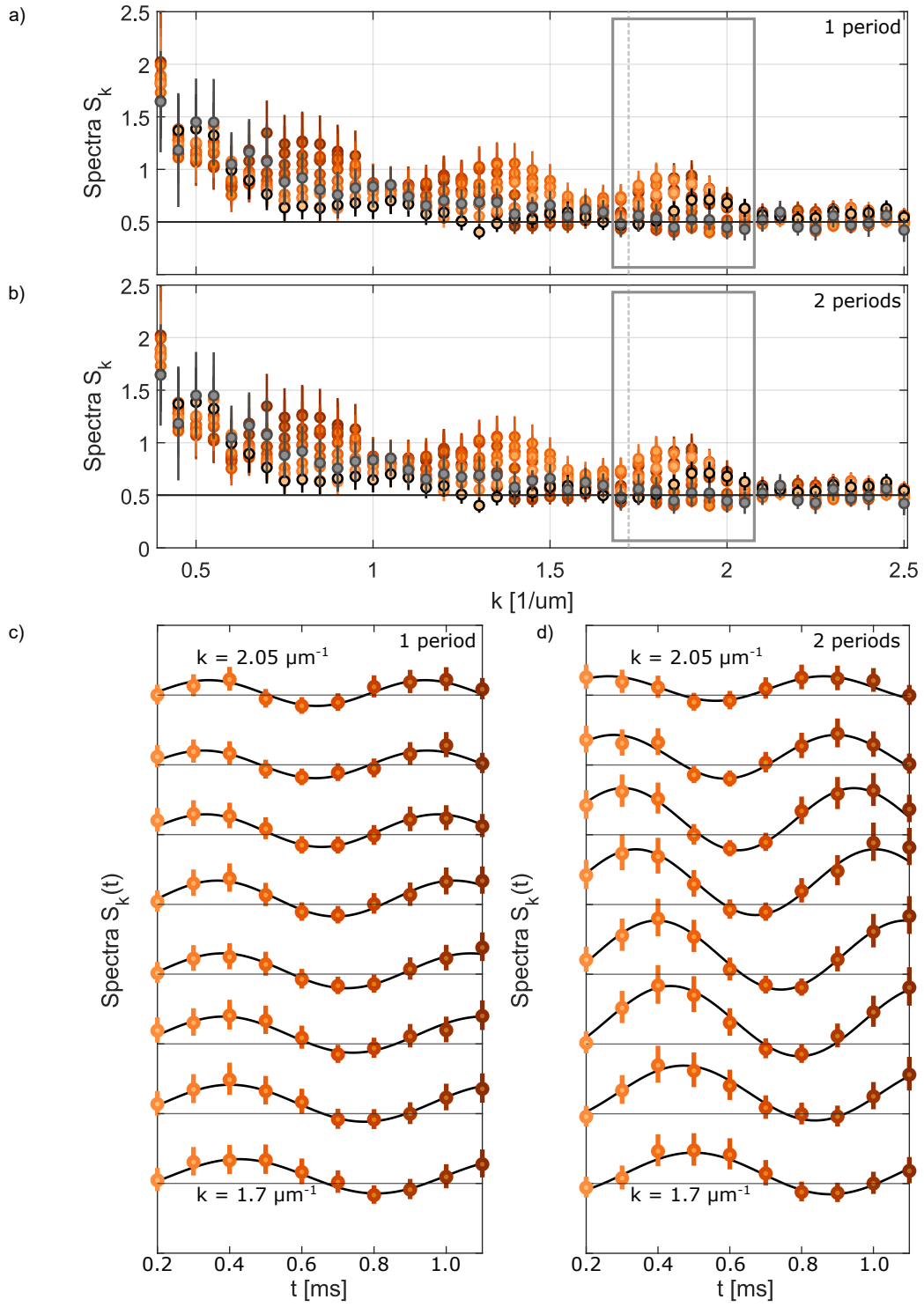

Figure C.1: Spectra (a,b) and coherent oscillations (c,d) for the cusp periodic scenario and G_{nn} correlations performed on the whole cloud. This is comparable to 6.14, where 90% in terms of the radius was used to extract the correlations.

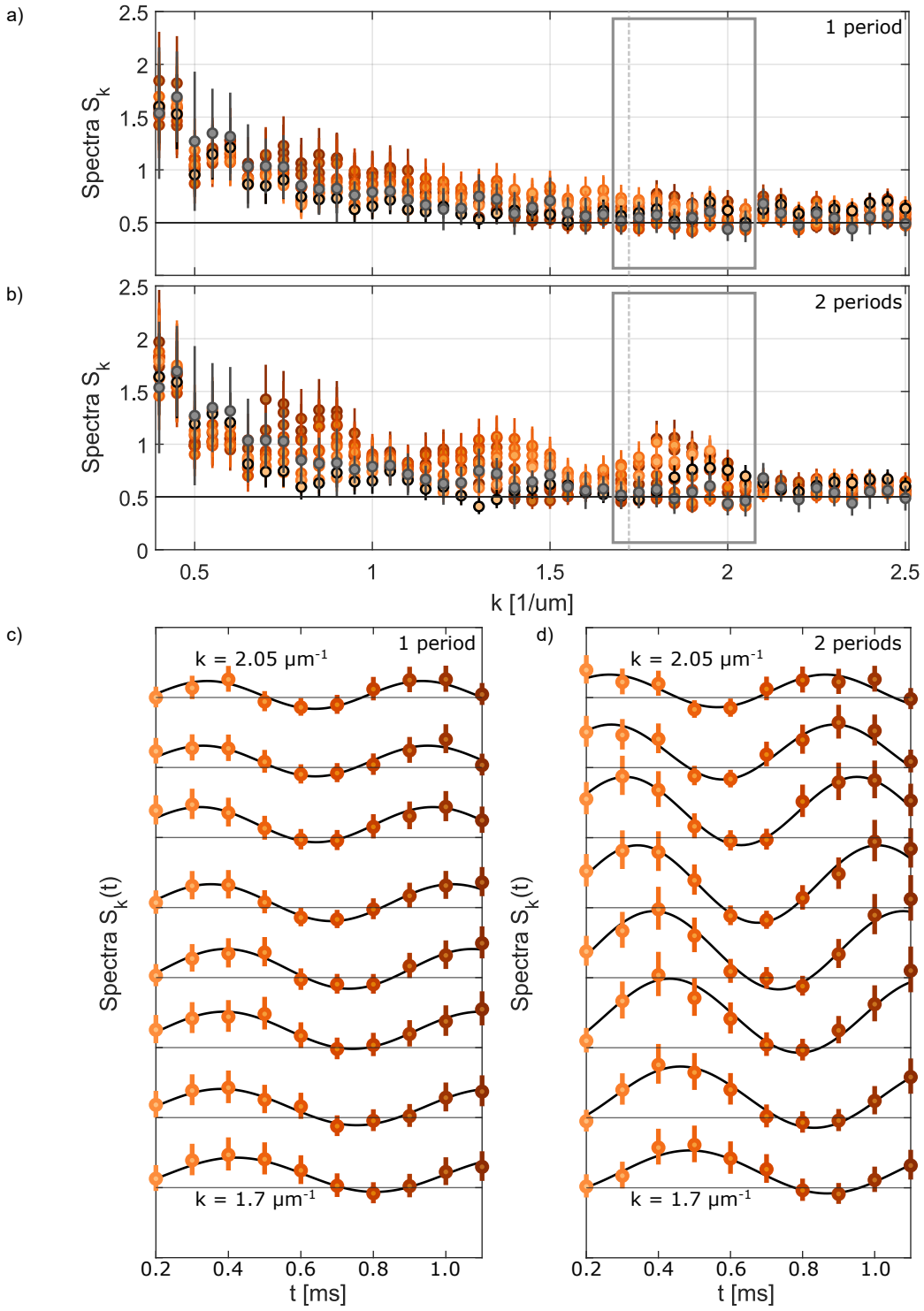

Figure C.2: Spectra (a,b) and coherent oscillations (c,d) for the cusp periodic scenario without performing the optimization algorithm on the reference images. Otherwise, the analysis is the same as in 6.14.

D
Appendix: Background Flows

If we had allowed for background flows $v \neq 0$ Eq. 4.13 would have taken the form

$$\Gamma_2[\phi] = \frac{\hbar^2}{2} \int dt d^2r \left[\frac{1}{c_s^2} \left(\partial_t \phi\right)^2 - \left(\nabla \phi\right)^2 + \frac{2}{c_s^2} \left(\partial_t \phi\right) \boldsymbol{v} \nabla \phi + \frac{1}{c_s^2} \left(\boldsymbol{v} \nabla \phi\right)^2 \right]. \tag{D.1}$$

The extra terms result in off-diagonal entries of the metric

$$\left(g_{\mu\nu}\right) = \frac{1}{c_s^2} \begin{pmatrix} -c_s^2 + v^2 & -v_j \\ -v_i & \delta_{ij} \end{pmatrix} \tag{D.2}$$

together with its inverse:

$$\left(g^{\mu\nu}\right) = \begin{pmatrix} -1 & -v^j \\ -v^i & c_s^2 \delta^{ij} - v^i v^j \end{pmatrix} \tag{D.3}$$

However, the action can still be written in the form of Eq. 2.1:

$$\Gamma_2[\phi] = -\frac{\hbar^2}{2} \int dt d^2r \sqrt{g} g^{\mu\nu} \partial_\mu \phi \partial_\nu \phi \tag{D.4}$$

For the FLRW-metric all off-diagonal terms are zero and, therefore, background flows are ruled out ($v = 0$).

List of Publications

Publications Related to Analog Simulation of Curved Spacetimes

- Marius Sparn, Elinor Kath, Nikolas Liebster, Jelte Duchene, Christian F. Schmidt, Mireia Tolosa-Simeón, Álvaro Parra-López, Stefan Floerchinger, Helmut Strobel, and Markus K. Oberthaler. "Experimental Particle Production in Time-Dependent Spacetimes: A One-Dimensional Scattering Problem". In: *Phys. Rev. Lett.* 133 (26 Dec. 2024), p. 260201. DOI: 10.1103/PhysRevLett.133.260201

- Christian F. Schmidt, Álvaro Parra-López, Mireia Tolosa-Simeón, Marius Sparn, Elinor Kath, Nikolas Liebster, Jelte Duchene, Helmut Strobel, Markus K. Oberthaler, and Stefan Floerchinger. "Cosmological particle production in a quantum field simulator as a quantum mechanical scattering problem". In: *Phys. Rev. D* 110 (12 Dec. 2024), p. 123523. DOI: 10.1103/PhysRevD.110.123523

- Mireia Tolosa-Simeón, Álvaro Parra-López, Natalia Sánchez-Kuntz, Tobias Haas, Celia Viermann, Marius Sparn, Nikolas Liebster, Maurus Hans, Elinor Kath, Helmut Strobel, Markus K. Oberthaler, and Stefan Floerchinger. "Curved and expanding spacetime geometries in Bose-Einstein condensates". In: *Physical Review A* 106 (3 Sept. 2022). ISSN: 24699934. DOI: 10.1103/PhysRevA.106.033313

- C. Viermann, M. Sparn, N. Liebster, M. Hans, E. Kath, Á. Parra-López, M. Tolosa-Simeón, N. Sánchez-Kuntz, T. Haas, H. Strobel, S. Floerchinger, and M. K. Oberthaler. "Quantum field simulator for dynamics in curved spacetime". In: *Nature* 611 (2022), pp. 260–264. DOI: 10.1038/s41586-022-05313-9

Other Publications

- Nikolas Liebster, Marius Sparn, Elinor Kath, Jelte Duchene, Keisuke Fujii, Sarah L. Görlitz, Tilman Enss, Helmut Strobel, and Markus K. Oberthaler. "Observation of Pattern Stabilization in a Driven Superfluid". In: *Phys. Rev. X* 15 (1 Feb. 2025), p. 011026. DOI: 10.1103/PhysRevX.15.011026

- Keisuke Fujii, Sarah L. Görlitz, Nikolas Liebster, Marius Sparn, Elinor Kath, Helmut Strobel, Markus K. Oberthaler, and Tilman Enss. "Stable-fixed-point description of square-pattern formation in driven two-dimensional Bose-Einstein condensates". In: *Phys. Rev. A* 109 (5 May 2024), p. L051301. DOI: 10.1103/PhysRevA.109.L051301

- Maurus Hans, Elinor Kath, Marius Sparn, Nikolas Liebster, Helmut Strobel, Markus K. Oberthaler, Felix Draxler, and Christoph Schnörr. "Bose-Einstein condensate experiment as a nonlinear block of a machine learning pipeline". In: *Phys. Rev. Res.* 6 (1 Jan. 2024), p. 013122. DOI: 10.1103/PhysRevResearch.6.013122

- Maurus Hans, Finn Schmutte, Celia Viermann, Nikolas Liebster, Marius Sparn, Markus K. Oberthaler, and Helmut Strobel. "High signal to noise absorption imaging of alkali atoms at moderate magnetic fields". In: *Review of Scientific Instruments* 92.2 (2021), p. 023203. DOI: 10.1063/5.0040677

Preprint

- Nikolas Liebster, Marius Sparn, Elinor Kath, Jelte Duchene, Helmut Strobel, and Markus K. Oberthaler. *Observation of supersolid-like sound modes in a driven quantum gas.* accepted at Nature Physics. 2025. arXiv: 2503.10519

Statement on AI Usage

AI tools have been used to proofread this thesis (Writefull) and to restructure individual sentences (DeepL and ChatGPT).
The first drafts for the translation of German references and of the abstract (to German) have been done by DeepL.
ChatGPT was used for the generation of MatLab code for figures, but not for data analysis.

Bibliography

[1] Carl Wilhelm Wirtz. "Einiges zur Statistik der Radialbewegungen von Spiralnebeln und Kugelsternhaufen". In: *Astronomische Nachrichten* (1922). DOI: 10.1002/asna.19212151703.

[2] Carl Wilhelm Wirtz. "De Sitters Kosmologie und die Radialbewegungen der Spiralnebel". In: *Astronomische Nachrichten* (1924). DOI: 10.1002/asna.19242220203.

[3] Georges Lemaître. "Un Univers homogène de masse constante et de rayon croissant rendant compte de la vitesse radiale des nébuleuses extra-galactiques". In: *Annales de la Société Scientifique de Bruxelles* (1927).

[4] Edwin Hubble. "A relation between distance and radial velocity among extra-galactic nebulae". In: *Proceedings of the National Academy of Sciences* 15.3 (1929), pp. 168–173. DOI: 10.1073/pnas.15.3.168.

[5] Ian Steer. "Who discovered Universe expansion?" In: *Nature* 490 (2012), p. 176. DOI: 10.1038/490176c.

[6] E. Schrödinger. "The proper vibrations of the expanding universe". In: *Physica* 6 (1939), pp. 899–912. DOI: 10.1016/S0031-8914(39)90091-1.

[7] L Parker. "Particle Creation in Expanding Universes". In: *Physical Review Letters* 21.8 (1968).

[8] C. L. Bennett et al. "Nine-Year Wilkinson Microwave Anisotropy Probe (WMAP) Observations: Final Maps and Results". In: *The Astrophysical Journal Supplement Series* 208 (2013). DOI: 10.1088/0067-0049/208/2/20.

[9] Alan H. Guth. "Inflationary universe: A possible solution to the horizon and flatness problems". In: *Phys. Rev. D* 23 (2 Jan. 1981), pp. 347–356. DOI: 10.1103/PhysRevD.23.347.

[10] Lev Kofman. "Preheating After Inflation". In: *Inflationary Cosmology*. Ed. by Martin Lemoine, Jerome Martin, and Patrick Peter. Berlin, Heidelberg: Springer Berlin Heidelberg, 2007, pp. 55–79. ISBN: 978-3-540-74353-8. DOI: 10.1007/978-3-540-74353-8_2.

[11] Mustafa A. Amin et al. "Nonperturbative dynamics of reheating after inflation: A review". In: *International Journal of Modern Physics D* 24.01 (2015), p. 1530003. DOI: 10.1142/S0218271815300037.

[12] Scott Dodelson and Fabian Schmidt. *Modern Cosmology*. Ed. by Scott Dodelson and Fabian Schmidt. Second Edition. Elsevier, 2021. ISBN: 978-0-12-815948-4. DOI: 10.1016/B978-0-12-815948-4.00015-2.

[13] Daniel J. Eisenstein et al. "Detection of the Baryon Acoustic Peak in the Large-Scale Correlation Function of SDSS Luminous Red Galaxies". In: *The Astrophysical Journal* 633 (2005), p. 560. DOI: 10.1086/466512.

[14] Stephen W. Hawking. "Black hole explosions?" In: *Nature* 248 (1975), pp. 30–31. DOI: 10.1038/248030a0.

[15] Scott A. Hughes. *Trust but verify: The case for astrophysical black holes*. 2005. arXiv: hep-ph/0511217 [hep-ph].

[16] D. J. Fixsen. "The Temperature of the Cosmic Microwave Background". In: *The Astrophysical Journal* 707.2 (Nov. 2009), p. 916. DOI: 10.1088/0004-637X/707/2/916.

[17] William G Unruh. "Experimental Black-Hole Evaporation?" In: *Phys. Rev. Lett.* 46 (21 1981), pp. 1351–1353. DOI: 10.1103/PhysRevLett.46.1351.

[18] Matt Visser. "Acoustic black holes: horizons, ergospheres and Hawking radiation". In: *Classical and Quantum Gravity* 15.6 (June 1998), p. 1767. DOI: 10.1088/0264-9381/15/6/024.

[19] Ralf Schützhold and William G. Unruh. "Gravity wave analogues of black holes". In: *Phys. Rev. D* 66 (4 Aug. 2002), p. 044019. DOI: 10.1103/PhysRevD.66.044019.

[20] Germain Rousseaux et al. "Observation of negative-frequency waves in a water tank: A classical analogue to the Hawking effect?" In: *New Journal of Physics* 10 (May 2008). ISSN: 13672630. DOI: 10.1088/1367-2630/10/5/053015.

[21] Thomas G Philbin et al. "Fiber-Optical Analog of the Event Horizon". In: *Science* 319 (5868 2008), pp. 1367–1370. DOI: 10.1126/science.1153625.

[22] Oren Lahav et al. "Realization of a Sonic Black Hole Analog in a Bose-Einstein Condensate". In: *Phys. Rev. Lett.* 105 (24 2010), p. 240401. DOI: 10.1103/PhysRevLett.105.240401.

[23] N. B. Kopnin and G. E. Volovik. "Critical velocity and event horizon in pair-correlated systems with "relativistic" fermionic quasiparticles". In: *Journal of Experimental and Theoretical Physics Letters* 67 (1998), pp. 140–145. DOI: 10.1134/1.567637.

[24] L. J. Garay et al. "Sonic Analog of Gravitational Black Holes in Bose-Einstein Condensates". In: *Phys. Rev. Lett.* 85 (22 Nov. 2000), pp. 4643–4647. DOI: 10.1103/PhysRevLett.85.4643.

[25] U. Leonhardt and P. Piwnicki. "Optics of nonuniformly moving media". In: *Phys. Rev. A* 60 (6 Dec. 1999), pp. 4301–4312. DOI: 10.1103/PhysRevA.60.4301.

[26] U. Leonhardt and P. Piwnicki. "Relativistic Effects of Light in Moving Media with Extremely Low Group Velocity". In: *Phys. Rev. Lett.* 84 (5 Jan. 2000), pp. 822–825. DOI: 10.1103/PhysRevLett.84.822.

[27] D. Faccio et al. "Analogue gravity and ultrashort laser pulse filamentation". In: *Europhysics Letters* 89.3 (Feb. 2010), p. 34004. DOI: 10.1209/0295-5075/89/34004.

[28] H. S. Nguyen et al. "Acoustic Black Hole in a Stationary Hydrodynamic Flow of Microcavity Polaritons". In: *Phys. Rev. Lett.* 114 (3 Jan. 2015), p. 036402. DOI: 10.1103/PhysRevLett.114.036402.

[29] M. Človečko et al. "Magnonic Analog of Black- and White-Hole Horizons in Superfluid ^{3}He$-B$". In: *Phys. Rev. Lett.* 123 (16 Oct. 2019), p. 161302. DOI: 10.1103/PhysRevLett.123.161302.

[30] Juan Ramón de Nova et al. "Observation of thermal Hawking radiation and its temperature in an analogue black hole". In: *Nature* 569 (7758 2019), pp. 688–691. DOI: 10.1038/s41586-019-1241-0.

[31] Carla R. Almeida and Maxime J. Jacquet. "Analogue gravity and the Hawking effect: historical perspective and literature review". In: *European Physical Journal H* 48 (1 Dec. 2023). ISSN: 21026459. DOI: 10.1140/epjh/s13129-023-00063-2.

[32] C. Barceló, S. Liberati, and M. Visser. "Probing semiclassical analog gravity in Bose-Einstein condensates with widely tunable interactions". In: *Phys. Rev. A* 68 (2003), p. 053613. DOI: 10.1103/PhysRevA.68.053613.

[33] Petr O. Fedichev and Uwe R. Fischer. ""Cosmological" quasiparticle production in harmonically trapped superfluid gases". In: *Physical Review A - Atomic, Molecular, and Optical Physics* 69 (3 2004). ISSN: 10502947. DOI: 10.1103/PhysRevA.69.033602.

[34] Uwe R Fischer and Ralf Schützhold. "Quantum simulation of cosmic inflation in two-component Bose-Einstein condensates". In: *Phys. Rev. A* 70 (6 2004), p. 63615. DOI: 10.1103/PhysRevA.70.063615.

[35] P. Jain et al. "Analog model of a Friedmann-Robertson-Walker universe in Bose-Einstein condensates: Application of the classical field method". In: *Phys. Rev. A* 76 (2007), p. 033616. DOI: 10.1103/PhysRevA.76.033616.

[36] Silke Weinfurtner, Angela White, and Matt Visser. "Trans-Planckian physics and signature change events in Bose gas hydrodynamics". In: *Physical Review D - Particles, Fields, Gravitation and Cosmology* 76 (12 Dec. 2007). ISSN: 15507998. DOI: 10.1103/PhysRevD.76.124008.

[37] S. Weinfurtner et al. "Cosmological particle production in emergent rainbow spacetimes". In: *Class. Quantum Grav.* 26 (2009), p. 065012. DOI: 10.1088/0264-9381/26/6/065012.

[38] I. Carusotto et al. "Density correlations and analog dynamical Casimir emission of Bogoliubov phonons in modulated atomic Bose-Einstein condensates". In: *Eur. Phys. J. D.* 56 (2010), pp. 391–404. URL: https://link.springer.com/article/10.1140/epjd/e2009-00314-3.

[39] Angus Prain, Serena Fagnocchi, and Stefano Liberati. "Analogue cosmological particle creation: Quantum correlations in expanding Bose-Einstein condensates". In: *Physical Review D - Particles, Fields, Gravitation and Cosmology* 82 (10 Nov. 2010). ISSN: 15507998. DOI: 10.1103/PhysRevD.82.105018.

[40] Matthias Wittemer et al. "Phonon Pair Creation by Inflating Quantum Fluctuations in an Ion Trap". In: *Phys. Rev. Lett.* 123 (18 2019), p. 180502. DOI: 10.1103/PhysRevLett.123.180502.

[41] Jeff Steinhauer et al. "Analogue cosmological particle creation in an ultracold quantum fluid of light". In: *Nat. Commun.* 13 (1 2022), p. 2890. DOI: 10.1038/s41467-022-30603-1.

[42] J.-C. Jaskula et al. "Acoustic Analog to the Dynamical Casimir Effect in a Bose-Einstein Condensate". In: *Phys. Rev. Lett.* 109 (22 Nov. 2012), p. 220401. DOI: 10.1103/PhysRevLett.109.220401.

[43] Chen Lung Hung, Victor Gurarie, and Cheng Chin. "From cosmology to cold atoms: Observation of Sakharov oscillations in a quenched atomic superfluid". In: *Science* 341 (6151 2013), pp. 1213–1215. ISSN: 10959203. DOI: 10.1126/science.1237557.

[44] S. Eckel et al. "A Rapidly Expanding Bose-Einstein Condensate: An Expanding Universe in the Lab". In: *Phys. Rev. X* 8 (2 2018), p. 21021. DOI: 10.1103/PhysRevX.8.021021.

[45] C.-A. Chen, S. Khlebnikov, and C.-L. Hung. "Observation of Quasiparticle Pair Production and Quantum Entanglement in Atomic Quantum Gases Quenched to an Attractive Interaction". In: *Phys. Rev. Lett.* 127 (6 2021), p. 060404. DOI: 10.1103/PhysRevLett.127.060404.

[46] S. Banik et al. "Accurate Determination of Hubble Attenuation and Amplification in Expanding and Contracting Cold-Atom Universes". In: *Physical Review Letters* 128 (9 Mar. 2022). ISSN: 10797114. DOI: 10.1103/PhysRevLett.128.090401.

[47] C. Viermann et al. "Quantum field simulator for dynamics in curved spacetime". In: *Nature* 611 (2022), pp. 260–264. DOI: 10.1038/s41586-022-05313-9.

[48] Carlos Barceló, Stefano Liberati, and Matt Visser. "Analogue Gravity". In: *Living Reviews in Relativity* 8.1 (2005). ISSN: 1433-8351. DOI: 10.12942/lrr-2005-12.

[49] Mireia Tolosa-Simeón et al. "Curved and expanding spacetime geometries in Bose-Einstein condensates". In: *Physical Review A* 106 (3 Sept. 2022). ISSN: 24699934. DOI: 10.1103/PhysRevA.106.033313.

[50] Christian F. Schmidt et al. "Cosmological particle production in a quantum field simulator as a quantum mechanical scattering problem". In: *Phys. Rev. D* 110 (12 Dec. 2024), p. 123523. DOI: 10.1103/PhysRevD.110.123523.

[51] Ruth Durrer. *The Cosmic Microwave Background*. Cambridge University Press, 2008. DOI: 10.1017/9781316471524.

[52] L. Parker. "Quantized Fields and Particle Creation in Expanding Universes. I". In: *Phys. Rev.* 183 (1969), pp. 1057–1068. DOI: 10.1103/PhysRev.183.1057.

[53] V. Mukhanov and S. Winitzki. *Introduction to Quantum Effects in Gravity*. Cambridge, England: Cambridge University Press, 2007. DOI: 10.1017/CBO9780511809149.

[54] S.E. Rugh and H. Zinkernagel. "The quantum vacuum and the cosmological constant problem". In: *Studies in History and Philosophy of Science Part B: Studies in History and Philosophy of Modern Physics* 33.4 (2002), pp. 663–705. ISSN: 1355-2198. DOI: https://doi.org/10.1016/S1355-2198(02)00033-3.

[55] Rainer Dick. *Advanced Quantum Mechanics*. Springer Cham, 2020. DOI: 10.1007/978-3-030-57870-1.

[56] Scott Robertson, Florent Michel, and Renaud Parentani. "Assessing degrees of entanglement of phonon states in atomic Bose gases through the measurement of commuting observables". In: *Physical Review D* 96 (4 Aug. 2017). ISSN: 24700029. DOI: 10.1103/PhysRevD.96.045012.

[57] Scott Robertson, Florent Michel, and Renaud Parentani. "Controlling and observing nonseparability of phonons created in time-dependent 1D atomic Bose condensates". In: *Physical Review D* 95 (6 Mar. 2017). ISSN: 24700029. DOI: 10.1103/PhysRevD.95.065020.

[58] Jérôme Martin, Amaury Micheli, and Vincent Vennin. "Discord and decoherence". In: *Journal of Cosmology and Astroparticle Physics* 2022 (4 Apr. 2022). ISSN: 14757516. DOI: 10.1088/1475-7516/2022/04/051.

[59] Ivan Agullo, Adrià Delhom, and Álvaro Parra-López. "Toward the observation of entangled pairs in BEC analog expanding universes". In: *Phys. Rev. D* 110 (12 Dec. 2024), p. 125023. DOI: 10.1103/PhysRevD.110.125023.

[60] E. A. Cornell and C. E. Wieman. "Nobel Lecture: Bose-Einstein condensation in a dilute gas, the first 70 years and some recent experiments". In: *Rev. Mod. Phys.* 74 (3 Aug. 2002), pp. 875–893. DOI: 10.1103/RevModPhys.74.875.

[61] Lev Pitaevskii and Sandro Stringari. "Bose–Einstein Condensation and Superfluidity". In: Oxford University Press, 2016. ISBN: 978–0–19–875888–4.

[62] Franco Dalfovo et al. "Theory of Bose-Einstein condensation in trapped gases". In: *Rev. Mod. Phys.* 71 (3 Apr. 1999), pp. 463–512. DOI: 10.1103/RevModPhys.71.463.

[63] Christopher Pethick. *Bose-Einstein condensation in dilute gases*. eng. Cambridge University Press, 2002. ISBN: 978-0-521-66194-2.

[64] Christian F.Schmidt and Stefan Floerchinger. "Dispersive Effects in Quantum Simulators for Cosmology: Influence and Prospects". Unpublished - Authors and title are preliminary.

[65] Celia Viermann. "Cosmological particle production and curved spaces in an ultracold quantum gas". PhD thesis. Universität Heidelberg, 2022.

[66] Marcel Kern. "Enhanced Local Control of Two-Dimensional Ultracold Atomic Clouds". MA thesis. Universität Heidelberg, 2024.

[67] Tobias Gerard Tiecke. "Feshbach resonances in ultracold mixtures of the fermionic quantum gases 6Li and 40K". PhD thesis. University of Amsterdam, 2009.

[68] Wolfgang Müssel. *Characterization of a Two-dimensional MOT for* ^{39}K. Diploma thesis. Universität Heidelberg, 2011.

[69] Maurus Hans. "Physical Computing on a Versatile Setup for Ultra-cold Potassium". PhD thesis. Universität Heidelberg, 2022.

[70] Alexander Fabian Impertro. *Laser system for magneto-optical cooling and trapping of potassium*. BA thesis. Universität Heidelberg, 2017.

[71] Nikolas Felix Laurenz Leonhardt. *Frequency offset stabilization of a fiber laser system for laser cooling of potassium*. BA thesis. Universität Heidelberg, 2022.

[72] Paul D. Lett et al. "Observation of Atoms Laser Cooled below the Doppler Limit". In: *Phys. Rev. Lett.* 61 (2 July 1988), pp. 169–172. DOI: 10.1103/PhysRevLett.61.169.

[73] Claude N. Cohen-Tannoudji. "Nobel Lecture: Manipulating atoms with photons". In: *Rev. Mod. Phys.* 70 (3 July 1998), pp. 707–719. DOI: 10.1103/RevModPhys.70.707.

[74] Alexandra Alice Beikert. *Controlled Frequency Generation for Grey Molasses Cooling*. BA thesis. Universität Heidelberg, 2021.

[75] Maurus Hans. "An experimental setup for a potassium Bose-Einstein condensate with tunable interactions". MA thesis. Universität Heidelberg, 2017.

[76] Marius Sparn. *Magnetic Fields for Cooling and Trapping of Potassium Atoms*. BA thesis. Universität Heidelberg, 2017.

[77] J. L. Roberts et al. "Controlled collapse of a Bose-Einstein condensate". In: *Physical Review Letters* 86 (19 May 2001), pp. 4211–4214. ISSN: 00319007. DOI: 10.1103/PhysRevLett.86.4211.

[78] Rudolf Grimm, Matthias Weidemüller, and Yurii B. Ovchinnikov. "Optical Dipole Traps for Neutral Atoms". In: *Advances In Atomic, Molecular, and Optical Physics*. Ed. by Benjamin Bederson and Herbert Walther. Vol. 42. Academic Press, 2000, pp. 95–170. DOI: https://doi.org/10.1016/S1049-250X(08)60186-X.

[79] Guillaume Gauthier et al. "Chapter One - Dynamic high-resolution optical trapping of ultracold atoms". In: *Advances In Atomic, Molecular, and Optical Physics*. Ed. by Louis F. Dimauro, Hélène Perrin, and Susanne F. Yelin. Vol. 70. Academic Press, 2021, pp. 1–101. DOI: https://doi.org/10.1016/bs.aamop.2021.04.001.

[80] Gauthier Guillaume. "Configuring BECs with Digital Micromirror Devices". In: *Transport and Turbulence in Quasi-Uniform and Versatile Bose-Einstein Condensates*. Cham: Springer International Publishing, 2020, pp. 79–119. ISBN: 978-3-030-54967-1. DOI: 10.1007/978-3-030-54967-1_4.

[81] Nikolas Liebster et al. "Observation of Pattern Stabilization in a Driven Superfluid". In: *Phys. Rev. X* 15 (1 Feb. 2025), p. 011026. DOI: 10.1103/PhysRevX.15.011026.

[82] Maurus Hans et al. "Bose-Einstein condensate experiment as a nonlinear block of a machine learning pipeline". In: *Phys. Rev. Res.* 6 (1 Jan. 2024), p. 013122. DOI: 10.1103/PhysRevResearch.6.013122.

[83] Nikolas Liebster et al. *Observation of supersolid-like sound modes in a driven quantum gas*. accepted at Nature Physics. 2025. arXiv: 2503.10519.

[84] Marius Sparn. "A Setup for Creating Arbitrary Potentials in a Two-dimensional ^{39}K BEC with a Digital Micromirror Device". MA thesis. Universität Heidelberg, 2020.

[85] Jelte Jan Luca Duchêne. "Designed Boundaries for Phonon-Based Quantum Simulations". MA thesis. Universität Heidelberg, 2024.

[86] J. Etrych et al. "Pinpointing Feshbach resonances and testing Efimov universalities in ^{39}K". In: *Phys. Rev. Res.* 5 (1 2023), p. 013174. DOI: 10.1103/PhysRevResearch.5.013174.

[87] Maurus Hans et al. "High signal to noise absorption imaging of alkali atoms at moderate magnetic fields". In: *Review of Scientific Instruments* 92.2 (2021), p. 023203. DOI: 10.1063/5.0040677.

[88] C. F. Ockeloen et al. "Detection of small atom numbers through image processing". In: *Phys. Rev. A* 82 (6 Dec. 2010), p. 061606. DOI: 10.1103/PhysRevA.82.061606.

[89] Jan Dreher. *An Offset Locking Scheme for Absorption Imaging of ^{39}K at High Magnetic Fields*. BA thesis. Universität Heidelberg, 2019.

[90] Elinor Kath. "Feasibility of Single-Atom-Resolved Fluorescence Imaging of Freely Propagating ^{39}K Atoms". MA thesis. Universität Heidelberg, 2022.

[91] C.-A. Chen, S. Khlebnikov, and C.-L. Hung. *Supplementary Information to "Observation of Quasiparticle Pair Production and Quantum Entanglement in Atomic Quantum Gases Quenched to an Attractive Interaction"*. 2021. DOI: 10.1103/PhysRevLett.127.060404.

[92] Marius Sparn et al. “Experimental Particle Production in Time-Dependent Spacetimes: A One-Dimensional Scattering Problem”. In: *Phys. Rev. Lett.* 133 (26 Dec. 2024), p. 260201. DOI: 10.1103/PhysRevLett.133.260201.

[93] Marcel Leutenegger. *Hankel transform*. Matlab package. 2006.

[94] Carl Ramsauer. “Über den Wirkungsquerschnitt der Gasmoleküle gegenüber langsamen Elektronen”. In: *Annalen der Physik* 369 (6 1921), pp. 513–540. ISSN: 15213889. DOI: 10.1002/andp.19213690603.

[95] J.S. Townsend and V.A. Bailey. “XCVII. The motion of electrons in gases”. In: *The London, Edinburgh, and Dublin Philosophical Magazine and Journal of Science* 42 (252 Dec. 1921), pp. 873–891. ISSN: 1941-5982. DOI: 10.1080/14786442108633831.

[96] Albert Einstein, Hedwig Born, and Max Born. *Briefwechsel. 1916 - 1955*. ger. Ungekürzte Ausg. Ullstein-Bücher ; 34345 : Ullstein-Sachbuch. Enth. Sammlungen von Einstein u. H. u. M. Born. Frankfurt/M [u.a.]: Ullstein, 1986, 329 S. ISBN: 3-548-34345-7.

[97] Andreas Albrecht et al. “Inflation and squeezed quantum states”. In: *Phys. Rev. D* 50 (8 Oct. 1994), pp. 4807–4820. DOI: 10.1103/PhysRevD.50.4807.

[98] Andrei D Sakharov. “The initial stage of an expanding universe and the appearance of a nonuniform distribution of matter”. In: *Sov. Phys. JETP* 22 (1966), p. 241.

[99] Marius Sparn et al. *Supplementary Information to "Experimental Particle Production in Time-Dependent Spacetimes: A One-Dimensional Scattering Problem"*. Dec. 2024. DOI: 10.1103/PhysRevLett.133.260201.

[100] Steven Weinberg. *Cosmology*. Oxford University Press, 2008. DOI: 10.1093/oso/9780198526827.001.0001.

[101] Juliana Almeida, Tatiana Rodrigues, and Alexys Bruno-Alfonso. “Solving the Schrödinger Equation by the Transfer-Matrix Method”. In: *Matemática Contemporânea* 59 (8 2024). DOI: 10.21711/231766362024/rmc598.

[102] William Henry Bragg and William Lawrence Bragg. “The reflection of X-rays by crystals”. In: *Proceedings of the Royal Society of London. Series A, Containing Papers of a Mathematical and Physical Character* 88 (605 1913), pp. 428–438. DOI: 10.1098/rspa.1913.0040.

[103] Peter Markos and Costas M. Soukoulis. *Wave Propagation: From Electrons to Photonic Crystals and Left-Handed Materials*. Princeton University Press, Dec. 2008. ISBN: 9781400835676. DOI: 10.1515/9781400835676.

[104] L.P. Pitaevskii and S. Stringari. “Landau damping in dilute Bose gases”. In: *Physics Letters A* 235.4 (1997), pp. 398–402. ISSN: 0375-9601. DOI: 10.1016/S0375-9601(97)00666-X.

[105] ST Beliaev. “Energy spectrum of a non-ideal Bose gas”. In: *Sov. Phys. JETP* 34.2 (1958), p. 299.

[106] Clément Duval and Nicolas Cherroret. "Quantum kinetics of quenched two-dimensional Bose superfluids". In: *Phys. Rev. A* 107 (4 Apr. 2023), p. 043305. DOI: 10.1103/PhysRevA.107.043305.

[107] Dennis Rätzel and Ralf Schützhold. "Decay of quantum sensitivity due to three-body loss in Bose-Einstein condensates". In: *Physical Review A* 103 (6 June 2021). ISSN: 24699934. DOI: 10.1103/PhysRevA.103.063321.

[108] Carlos Sabín et al. "Phonon creation by gravitational waves". In: *New Journal of Physics* 16 (2014). ISSN: 13672630. DOI: 10.1088/1367-2630/16/8/085003.

[109] Aleksandr Chatrchyan et al. "Analog cosmological reheating in an ultracold Bose gas". In: *Phys. Rev. A* 104 (2 Aug. 2021), p. 023302. DOI: 10.1103/PhysRevA.104.023302.

[110] Ke Wang, Han Fu, and K. Levin. "Simulating cosmological evolution by quantum quench of an atomic Bose-Einstein condensate". In: *Physical Review A* 109 (1 Jan. 2024). ISSN: 24699934. DOI: 10.1103/PhysRevA.109.013316.

[111] Dan M. Stamper-Kurn and Masahito Ueda. "Spinor Bose gases: Symmetries, magnetism, and quantum dynamics". In: *Rev. Mod. Phys.* 85 (3 July 2013), pp. 1191–1244. DOI: 10.1103/RevModPhys.85.1191.

[112] P. É Larré and N. Pavloff. "Hawking radiation in a two-component Bose-Einstein condensate". In: *EPL* 103 (6 Sept. 2013). ISSN: 02955075. DOI: 10.1209/0295-5075/103/60001.

[113] Anna Berti, Luca Giacomelli, and Iacopo Carusotto. "Superradiant phononic emission from the analog spin ergoregion in a two-component Bose–Einstein condensate". en. In: *Comptes Rendus. Physique* 24.S3 (2023), pp. 113–132. DOI: 10.5802/crphys.145.

[114] Philipp Kunkel et al. "Simultaneous Readout of Noncommuting Collective Spin Observables beyond the Standard Quantum Limit". In: *Phys. Rev. Lett.* 123 (6 Aug. 2019), p. 063603. DOI: 10.1103/PhysRevLett.123.063603.

[115] Tapio Simula. "Gravitational vortex mass in a superfluid". In: *Phys. Rev. A* 101 (6 June 2020), p. 063616. DOI: 10.1103/PhysRevA.101.063616.

[116] Salvatore Butera and Iacopo Carusotto. "Numerical Studies of Back Reaction Effects in an Analog Model of Cosmological Preheating". In: *Physical Review Letters* 130 (24 June 2023). ISSN: 10797114. DOI: 10.1103/PhysRevLett.130.241501.

[117] Scott Robertson, Florent Michel, and Renaud Parentani. "Nonlinearities induced by parametric resonance in effectively 1D atomic Bose condensates". In: *Physical Review D* 98 (5 Sept. 2018). ISSN: 24700029. DOI: 10.1103/PhysRevD.98.056003.

[118] M. Carlesso et al. "Testing the gravitational field generated by a quantum superposition". In: *New Journal of Physics* 21 (9 Sept. 2019). ISSN: 13672630. DOI: 10.1088/1367-2630/ab41c1.

[119] Marios Christodoulou and Carlo Rovelli. "On the possibility of laboratory evidence for quantum superposition of geometries". In: *Physics Letters B* 792 (2019), pp. 64–68. ISSN: 0370-2693. DOI: https://doi.org/10.1016/j.physletb.2019.03.015.

Acknowledgements

I want to use these last pages to thank the people who enabled me to pursue this scientific journey in recent years. Many people contributed to the success of the project described in this document, the many other scientific endeavors on which we departed over the years, and the overall great time we shared.

First, I want to thank Markus Oberthaler, who continuously put his trust in me and my abilities to progress the BECK experiment and employ it to achieve scientific success. Thank you for sharing your knowledge, your continued excitement for our work, and the plethora of analogies and expertise you bring from other research areas into our discussions.

I also thank Lauriane Chomaz, who agreed to examine this thesis. I look forward to discussing the contents of this work with you.

The same is true for the other members of my defense committee, Werner Aeschbach and Thomas Gasenzer. Thank you for your time.

My thanks also go to Helmut Strobel. His role in making the BECK the stable, functioning experiment that it is cannot be overestimated. I also thank you for your scientific guidance, not only for this project but also for the completion of my earlier theses.

Of course, I would also like to thank all the other current and former BECK members who make this experiment a success story and an enjoyable working environment. Many thanks to my current team members Nikolas Liebster, Elinor Kath, Jelte Duchêne, Philipp Weingardt and Louis Evans. Thank you, Elinor, for all the work you have put into this project and for introducing me to Mike's sports program. Thanks Nikolas, for the constant optimization of the experiment and leading the search for periodic structures in the spatial dimensions. Thanks to Jelte for proof-reading this thesis and to all of you for discussing not only scientific ideas but also politics and nonsense over lunch.

I would also like to thank the former PhD students at BECK, Celia Viermann and Maurus Hans, who set up the BECK experiment and laid the foundation for our current research, as well as former Master's student Marcel Kern and many Bachelor's students who have all made important contributions over the years to what the experiment is today. Many thanks to each and every one of you, you all form or formed great teams.

I thank the entire Matterwave group for the great times we had. Thank you for being such inviting people and keep doing all the great things that keep this a lively group. Special thanks to all those that made our group retreats possible. This was always a great time to not only progress academically, but also grow as a group.

Thank you to Stefan Floerchinger and the theory group around him for originally sparking the idea and embarking on this journey with us. This especially includes Christian Schmidt, who is responsible for many of the recent theoretic advancements and supported this thesis by discussions and proofreading. I also want to thank the former members of the group Mireia Tolosa-Simeón and Álvaro Parra-López for their work on the project as well as all the other former members that helped to build the formalism.

I also want to thank the people who are involved in the KIP infrastructure. Thank you to the current and former members of the workshop, for building so many vital parts of the experiment and coming up with solutions for our engineering problems. Among many others, this includes David Jansen and Julia Bing, who built many of those parts often from incomplete sketches and on short notice. Thank you to the people in the administration for keeping the institute running and enabling us to pursue the science, for example through orders and tender invites.

Thank you to the current and former team-assistants Christiane Jäger, Petra Hübler and Dagmar Hufnagel for organizing everything group related.

I also want to thank a few people from my personal life. I want to thank my family for sparking my scientific interest and supporting me to be able to follow up on this interest throughout my life. Thank you for continued support also during this writing stage, especially to my father, who spent the time to proofread the entire thesis.

I thank my friends for making my time in Heidelberg so pleasant. Thank you for the fun times and also for your emotional support in the more stressful times.

Finally, I want to thank my partner Lisa for our great relationship and supporting me throughout the years and especially during the writing stage of this thesis. You not only played the most vital role in supporting me emotionally, you also almost single-handedly made sure I did not have to live on takeout for the last months. Thank you so much.

Thanks again to all the people I mentioned and the others I may have forgotten that make this a very enjoyable patch of spacetime!